Spring 2020

Thermal Contact Resistance Measurement and Related Uncertainties

Amanda Elizabeth Stark
Old Dominion University, amandaestark@gmail.com

THERMAL CONTACT RESISTANCE MEASUREMENT AND RELATED UNCERTAINTIES

by

Amanda Elizabeth Stark
B.F.A December 2003, Grand Valley State University
M.F.A. May 2006, Bowling Green State University
B.S. August 2016, Grand Valley State University

A Thesis Submitted to the Faculty of
Old Dominion University in Partial Fulfillment of the
Requirements for the Degree of

MASTER OF SCIENCE

OLD DOMINION UNIVERSITY
May 2020

Approved by:

Dr. Robert Ash (Director)

Dr. Kamran Daryabeigi (Member)

Dr. Arthur Taylor (Member)

ABSTRACT

THERMAL CONTACT RESISTANCE MEASUREMENT AND RELATED UNCERTAINTIES

Amanda Elizabeth Stark
Old Dominion University, 2020
Director: Dr. Robert Ash

Thermal contact resistance is an important parameter in detailed thermal analysis and design of aerospace systems. The ability to determine thermal contact resistance reliably can have a significant impact on the fidelity of thermal models—particularly for space applications. The 2004 NASA Langley Research Center thermal contact resistance test apparatus has been employed to evaluate two methods for inferring estimated interface surface temperatures so that thermal contact resistance can be calculated more accurately. The traditional method of extrapolation is a steady-state approach, while the new method utilizes inverse heat transfer techniques to account for inherent unsteadiness in these quasi-steady-state measurements. The understanding of the uncertainty for the empirical data has helped quantify the reliability of thermal contact resistance. As a result, this study includes a thorough uncertainty analysis so that the two methods could be compared.

ACKNOWLEDGMENTS

All research was completed at NASA Langley Research Center in Hampton, Virginia with the help of the Structural & Thermal Systems Branch and Systems Integration & Test Branch.

With thanks to Dr. Robert Ash, Dr. Kamran Daryabeigi, Dr. Arthur Taylor, Dr. Walter Bruce, Warren Davis, Dwight Duncan, Josh Beverly, and the many other engineers and technicians at NASA Langley who helped to make this possible. Also, to my husband Ryan Biraben and my other family members for always being there when I needed encouragement.

NOMENCLATURE

A	Cross-sectional area (m^2)
B	Slope of a least-squares linear fit line
C	Number of collection points used in least-squares linear fit line
c_p	Specific Heat (J/kg-°C)
D	Constant defining a least-squares linear fit line
Da	Measured depth of TC hole in (mm)
hx	Measured location of TC drill hole along Meter Bar (mm)
I	Number of nodes for discretization along length
k_i	Thermal conductivity at point *i* (W/m-°C)
k_m	Thermal conductivity of a material (W/m-°C)
N	Number of total time steps
P_e	Uncertainty of a value for a determined confidence interval
q	Heat flux (W/m^2)
Q	Heat flow rate (W)
R′	Thermal Contact Resistance (°C-m^2/W)
S_e	Standard Deviation of the test article set
T	Temperature (°C)
T_y	Temperature measured at y-location (°C)
t	t-distribution associated to the appropriate degrees of freedom
Δt	Time interval/step (sec)
ΔT	Temperature difference (°C)
ΔT_m	Temperature difference in Meter Bars (°C)
U	Uncertainty in the indicated measured value
x	Measured location (mm)
x′	Measured location adjustment based on hole angle (mm)
X	Measured location of hole accounting for angle of drill (mm)
Δx_i	Distance between discretized points (m)

Δx_{TC} Distance between measured locations (m)

y Temperature, used for least-squares linear fit line

ϱ Density (kg/m^3)

θ Angle of drilled hole (degree)

σ_y Error of extrapolated value y

δ Uncertainty in variable that it proceeds

Subscript and Superscript

i Discretized point used in IHT code for bottom test article and code validation

j Discretized point used in IHT code for the top test article

n Time step location

Acronyms

DAQ Data Acquisition

IHT Inverse Heat Transfer

LaRC Langley Research Center

PID Proportional-Integral-Derivative

SS304 Stainless Steel 304

TC Thermocouples

TCR Thermal Contact Resistance

TABLE OF CONTENTS

Page

LIST OF FIGURES

Figure Page

Figure Page

LIST OF TABLES

Table Page

1 INTRODUCTION

Thermal contact resistance (TCR) occurs when two solid surfaces at different temperatures are brought into contact with each other. Mathematically, the interface is assumed to have no thickness, but the two surface temperatures do not actually achieve the same value. A temperature difference exists between the two surfaces at the interface indicating a resistance in the heat flow through the interface. The heat flow at the interface is affected by the imperfections present due to surface finish and the result is thermal contact resistance.

By using surface roughness measurements, the physical characteristics of the interface surfaces can be quantified. No matter the surface finish, an actual interface will experience all three heat transfer modes: conduction between the solid material points of contact, conduction/convection within the interstitial gas that is trapped in the gaps between the two solids, and radiation across spaces where the solids are not in contact. When two contacting parts are placed in a vacuum, heat can transfer through conduction at the small physical contact points at the interface. Radiant exchange can still be present in a vacuum environment, and if the level of vacuum decreases to the point where enough molecules are present, there will also be gas conduction. These restrictions in heat transfer paths result in TCR.

The resistance to heat flow has been a topic of interest to the aerospace community since the 1950s due to heat transfer in the vacuum of space being limited to radiation and solid conduction. In order to increase the possibility of mission success from a thermal perspective, the knowledge of TCR at the interface of various components is highly important and is needed to correctly model and understand the space-bound systems. By assembling an experimental test setup so that test interfaces can be used to directly determine TCR for specific interfaces, thermal engineers can incorporate the found values in thermal models.

The thesis research described herein has been conducted jointly with a NASA LaRC effort to design and fabricate a test apparatus that can be used to determine the contact resistance between two material test articles. The goal for this apparatus is to enable near real-time contact resistance measurements permitting thermal design engineers to acquire resistance values that support high confidence hardware performance estimates. A common practice when TCR is

unknown is to rely on sensitivity studies to help engineers assess the accuracy of the TCR values to appropriately analyze space-bound hardware systems. The final steps in these analyses correlate the thermal model results with actual thermal vacuum testing.

Experimental thermal contact resistance data collections date back to the late 1960s [1]. Literature discussed in this study has focused primarily on recent efforts conducted since the early 1990s. A limited amount of older literature has been included to document progression of the state of the art. One past researcher who is of interest to this project is Thomas McWaid from the University of California Santa Barbara [2], whose work includes detailed descriptions of his experimental setup. McWaid studied contact resistance between two well-characterized surface test articles. He was not the only researcher interested in generating such an algorithm; others include Yovanovich [3], Merrill and Garimella [4], Tomimura et al [5], Bahrami, Culham and Yovanovich [6], and Fuller and Marotta [7]. However, most TCR documents published by these research groups lacked the test apparatus design and test procedure details necessary to reproduce their results and to ensure accuracy and repeatability. The advantage of McWaid's work is that it has the potential to be used as a reference to compare results by matching his experiments. He used a longitudinal heat flow apparatus to determine TCR values between Aluminum 6061 test articles and Stainless Steel 304 (SS304) test articles; the interface surface of each set was prepared following the same procedure and was measured for surface roughness values. The experiment design and testing procedure for his research was conducted so that the main focus was to generate an algorithm to calculate TCR, which was then verified through experimentation.

Even though published research by numerous investigators has spanned several decades and has produced interesting outcomes, most of that data cannot be used in contemporary thermal analyses because the studies focused on specific applications that may not be applicable to space hardware. Many of these studies include information that is directly related to the specific application but may not report all information that is required to fully compare the study to the space hardware that is being analyzed. Consequently, NASA has been interested in developing not only the experimental contact resistance test setup, but also a database that can contain all results produced by the test apparatus at NASA LaRC.

The test apparatus design was required to generate repeatable, near-real-time contact resistance values suitable for direct application to the development of space hardware thermal designs. However, one does not build a test apparatus to measure TCR directly. Instead, the test apparatus should be designed to measure the internal temperature, at known locations, within two test articles of the same or different material. In most cases the thermocouples (TCs) are placed down the center line at locations equidistant from both ends and each other. The measured internal temperatures should accurately illustrate the thermal gradient that is present in the test articles. The collected temperature data can then be used to estimate the temperature of each interface surface. The other required value for calculating TCR is internal heat flux. The same temperature data that was used for estimating the interface surface temperatures can also be used to calculate the internal heat flux within the test articles.

The uncertainty associated with the interface temperatures can help identify the degree of accuracy that exists in the estimated values and can propagate through the TCR calculation along with the uncertainty of other required values. Actual uncertainty in the interface-based surface temperatures is not the only potential error. Other error sources include the following: measured dimensional accuracies, knowledge of material thermal properties, uncertainty in the heat flux, heat losses to the surroundings due to radiation, and gaseous conduction due to inadequate evacuation of the vacuum chamber testing environment; this last issue could also result in gaseous conduction between the test articles [8].

This research effort has focused on estimating surface temperatures at the two contacting interfaces. Previous methods for estimating the interface surface temperatures have been examined and compared with a new approach proposed herein. Contemporary methods have utilized linear extrapolation to determine both interface surface temperatures [2,9–13]; while this new approach utilizes the Inverse Heat Transfer (IHT) method to calculate interface temperatures based on two internal test article temperature measurements [14,15]. Test results based on both methods have been compared after identifying quantifiable uncertainties related to the estimated surface temperatures. Since the interface surface temperatures are some of the quantities employed in calculating TCR, a clear understanding of the confidence levels associated with the

two interface temperatures must be properly characterized in the overall TCR uncertainty analysis.

Part of this research involved restoring a TCR test fixture originally used at LaRC between 2003 and 2005 [16]; the current test apparatus will be described in Section 2.2. The work presented here is only a small step toward creating a test fixture design that can be used for direct evaluation of TCR between material surfaces commonly utilized in aerospace hardware design. The desired data products will be TCR tabulations over a relevant range of temperatures when properly characterized surface finishes are subjected to carefully applied compressive forces, along with the associated uncertainty in the TCR values.

In summary, this thesis provides an overview of thermal contact resistance fundamentals including current methods for estimating contact surface temperatures and the development of a newly-proposed approach for estimating the surface temperatures. Experimental uncertainty has been addressed.

This study first verified an IHT MATLAB code. Subsequently, the prototype test setup utilizing two sets of SS304 surface test articles were employed to record the temperatures needed to calculate TCR. The test article surfaces were characterized as bead blasted interface surfaces. Parasitic losses due to radiation were discussed but not addressed in-depth in this work. Finally, the results were compared with similar TCR values found in published literature for SS304 with comparable interface surface finishes.

2 BACKGROUND

2.1 THERMAL CONTACT RESISTANCE

When surfaces come into contact in the atmosphere, there are three modes of heat transfer present between the two surfaces: (1) conduction through the physical contact areas between the two solid surfaces, (2) conduction through the fluid medium filling any voids between the two surfaces [2], and (3) radiation when the void volumes are optically transparent. Natural convection does not occur for properly prepared contact surfaces since characteristic Grashof numbers based on void volume dimensions will be substantially below onset levels on the order of 2000 [17], and nominally equal to zero for orbiting systems. In this research, all testing was conducted within a vacuum chamber operated in the absolute pressure range of 10^{-2} to 10^{-3} Torr (mid-vacuum range) and at temperatures below 300°C. Previous research has shown that radiation heat transfer effects are negligible in that temperature range [18]. This was investigated with a short analysis calculating radiation heat loss after TCR data had been collected. Another advantage of the vacuum chamber test environment is that gaseous conduction with the surroundings are eliminated. The result is that thermal energy can only be transferred via contact conduction at the interface. Hence, part of this research has attempted to isolate and characterize thermal contact resistance produced primarily by heat conduction through the physical contact areas, as influenced by controlled application of compressive load forces.

Since no surface is completely flat, the physical points of contact are limited to the outermost asperities, thus limiting the heat flow, as illustrated in Fig. 1. The actual area of contact is dependent on the surface roughness, the mechanical properties of the materials, and any applied normal forces.

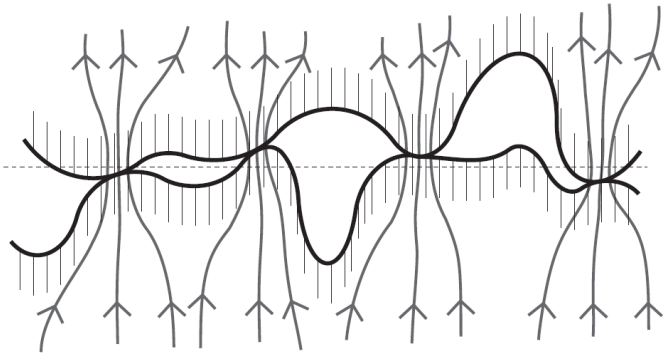

Fig. 1 Cross sectional view of heat flow paths through a contact interface.

Thermal contact resistance and thermal contact conductance have both been employed to characterize the thermal exchange between two contacting surfaces. Specification of "resistance" or "conductance" depends on the specific application. Both quantities can easily be found since one is the inverse of the other. The basic mathematical definition of TCR utilizes heat flux, $q"$, i.e.,

$$R" = \frac{T_A - T_B}{q"} \quad \left[\frac{m^2 - °C}{W}\right] \tag{1}$$

where T_A and T_B are the interface surface temperatures (°C), q'' is the heat flux (W/m²), and R'' is the TCR (m²-°C/W). The basic steady-state heat flux equation can be used to determine the heat flux in the sample column:

$$q" = k\frac{T_1 - T_2}{\Delta x} \quad \left[\frac{W}{m^2}\right] \tag{2}$$

where T_1 and T_2 are measured temperatures (°C) within the test articles, k is the thermal conductivity of the material (W/m-K), Δx is the measured axial distance between the two temperature measurement locations. Figure 2 is a schematic representation of the temperature gradient through two test articles with similar thermal conductivities and the temperature drop at the interface between them, along with the associated heat flux direction. Some researchers substitute overall heat flow rate ($Q = q'' \times A$) for local heat flux rate; that approach is limited

because the precise cross sectional area must be known in order to compare the TCR results to other application [2,18]. A longitudinal heat flow test apparatus can be used to collect the required data for estimating the TCR values between two surface test articles [19].

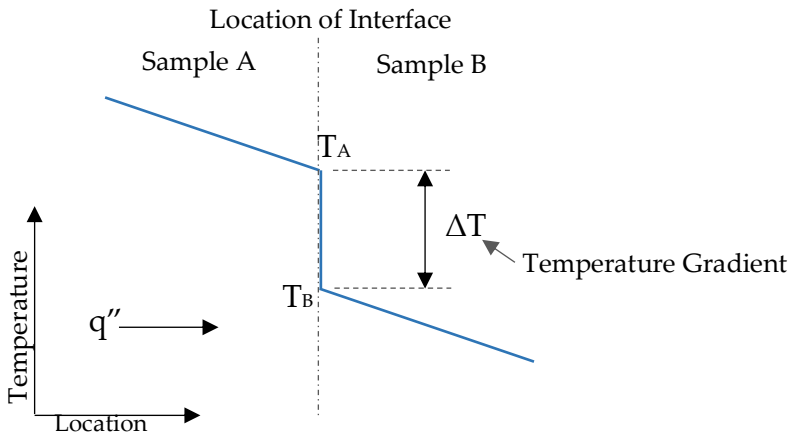

Fig. 2 Temperature gradient through test article A and test article B with temperature drop at interface.

2.2 DESCRIPTION OF CURRENT TEST SETUP

The LaRC test fixture is a longitudinal heat flow apparatus and was built following specifications defined by the ASTM standard E1225-13. Starting in 2017, the LaRC test fixture setup has undergone a recommissioning process, and will be used in this study to compare the results found through extrapolation and IHT for estimating the interface surface temperatures [19].

Since the point of interest is the interface between two materials, the fixture must be able to minimize heat loss to the surrounding from the two test articles while allowing thermal energy flow from a heater through one test article and then to the other, allowing for temperatures to be measured along the test articles. By placing the test fixture in a vacuum chamber, convective heat transfer and gaseous conduction can be eliminated. This will allow conduction to be the primary

interface heat transfer mechanism between interfacing surfaces, facilitating the determination of TCR. This test fixture was designed to fit in a Stainless Steel Bell Jar located in building 1250 at NASA LaRC; details of the system can be found in the Appendix, Section A.

The present design employs two cylindrical test articles placed between the upper and lower Meter Bars, as shown schematically in Figure 3. A controlled heater and associated heat sink are located at either end of the test setup. Meter Bars are not one meter in length, they were actually 45 mm long for this test setup and had the same diameter as the test articles (24 mm in diameter). The term "Meter Bar," found within the ASTM E1225-13 standard [19], implies an instrumented bar that can be used for quantitative measurements. By constructing the Meter Bar from material with very low thermal conductivity, the temperature gradient will be well defined. For this setup cylindrical Invar (65FeNi) Meter Bars were employed. Four blind holes with a 0.9 mm diameter were drilled at evenly spaced intervals, approximately 9 mm apart, with a depth approximately equivalent to the radius of the cylinder; this allowed the temperature to be measured along the centerline of the Meter Bar. T-type (36-gauge, 0.13 mm diameter) TCs were then installed in the holes. *Apiezon N* vacuum grease was used to fill the voids around the TCs in the blind holes, while aluminum tape was placed over each hole to hold the TCs in place. The TCs should have a distance between them of at least 10 times the diameter of the chosen TC, this also needed to be followed between the top/bottom TC and each surface (TCR interface or not) [8]. Adhering to this spacing to diameter ratio ensured that the local thermal distortion at each TC location would not affect adjacent TCs.

The Touloukian [20] temperature-dependent thermal conductivity data for Invar (found in the Appendix, Section D) was utilized, along with the TC data, to determine the heat flux through the Meter Bars. By embedding TCs along the center line of the Meter Bar, the temperature gradient can then be calculated. In Fig. 3 there are two Meter Bars that are equipped with TCs numbered TC2 through TC5 and TC12 through TC15.

Each test article was also prepared with embedded TCs in a similar method to that of the Meter Bar. Blind holes were drilled into the test articles perpendicular to the centerline so that the TC junctions could be placed along the centerline of the test articles. Vacuum grease was also used along with Aluminum tape to secure the TCs in place. Since the blind holes required manual

machining, the location of the bottom of the hole along the height of the cylinders were found using the drill angle and hole depth; the distances between the bottom of the blind holes along the central axis is provided in the Appendix, Section D along with the description of the procedure that was followed; the same procedure was used to find the location of the TC holes for the Meter Bar. The length of the test articles was flexible while keeping in mind the requirement for the distance between each TC (at least 10 times the TC diameter) that will reduce thermal distortion. Figure 4 shows the actual sample column incorporating two test articles mounted in the test fixture.

The collected test article TC data were used to calculate temperature gradient within each test article. The heat flux was also calculated by using the collected test article TC data; the same TC data was used to estimate the interface surface temperatures. Each test article had three embedded TCs, shown as TC6 through TC11 in Fig. 3.

The assembly of Meter Bar(s), test articles, heater, and heat sink is called the *sample column*. The heater was positioned at the top of the column and the heat sink beneath the sample column, prior to the evacuation of the vacuum chamber. The sample column is isolated thermally from the test frame by minimizing external contacts by using Stainless Steel ball pivots, as shown in Fig. 3. The pivots also provided a secondary functionality of reducing bending moments through the sample column when the compressive force is applied [21]. This allows for the compressive load to be evenly applied at the interface. By adding the capability of adjusting the compressive force at the interface to a desired load, TCR can be found not only for specific materials and surface finishes, but also under a variety of compressive forces. The compressive force is controlled by utilizing a pneumatic cylinder and a moveable horizontal plate. A load cell located below the bottom moveable horizontal plate was used to measure the compressive force applied to the column. The test frame was constructed from Aluminum and Stainless Steel so that it would withstand the force applied to the sample column. Figure 3 is a schematic diagram of the sample column with the horizontal moveable plates.

All horizontal interface surfaces within the sample column, except for the actual TCR interface surfaces, were coated with a thin layer of Apiezon N thermal grease for improved thermal contact. The flat ends of the Meter Bars and the opposite side of the interface surface on

the test articles were highly polished to improve thermal contact at the interfaces between the Meter Bars and the test articles along with the heater/heat sink interfaces. The interface surfaces for each test article were prepared to desired surface finish specifications.

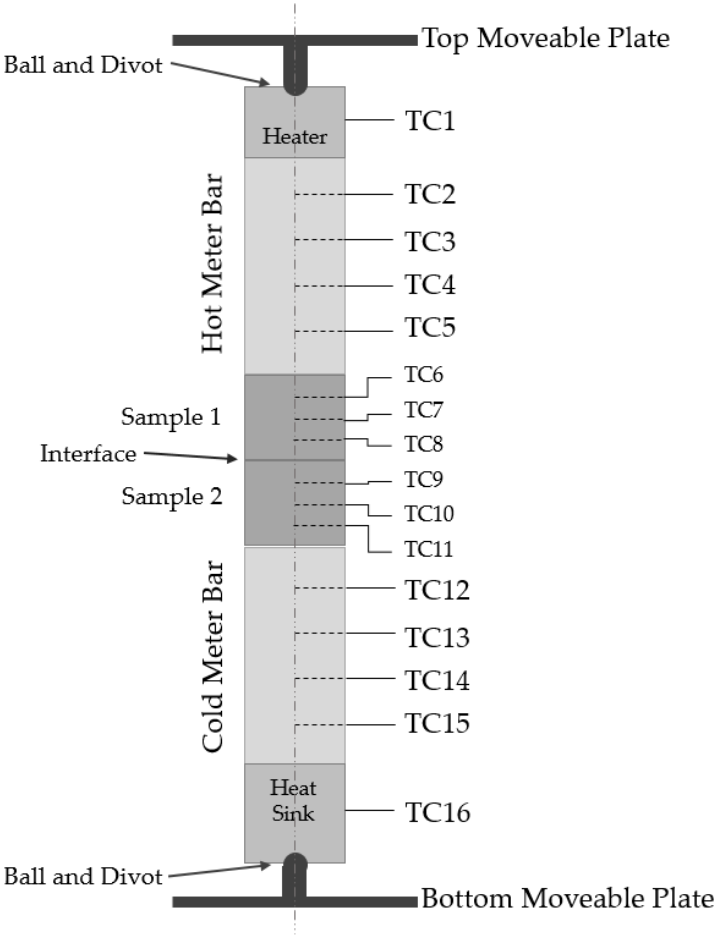

Fig. 3 Orientation of components in sample column with top and bottom moveable plates from 2003 and 2017 test setup.

Electric power for the heater, coolant lines for the heat sink, the communication cable for the load cell, pressurized air lines to/from the pneumatic cylinder, and wiring for each TC were introduced through ports in the vacuum chamber wall. An external power supply provided the desired electrical power to the heater so that desired test temperatures could be achieved. A water chiller provided coolant to the heat sink. The vacuum chamber was controlled via a computer

utilizing *LabView™* software that not only collected all TC and load cell data but also controlled the applied compressive force utilizing a Proportional-Integral-Derivative (PID) controller. A hand regulator was placed at the facility airline so that the supply air pressure would be consistent throughout testing. The Enfield TR-010-g10-S air regulator was chosen to control the air pressure supplied to the pneumatic cylinder so that the desired compressive force could be achieved. Since the compressive force system is controlled using a PID controller it had the ability of compensating for thermal expansion effects during testing by adjusting the air pressure to the pneumatic cylinder so that the compressive force was constant. A schematic of the full system can be found in Fig. 5.

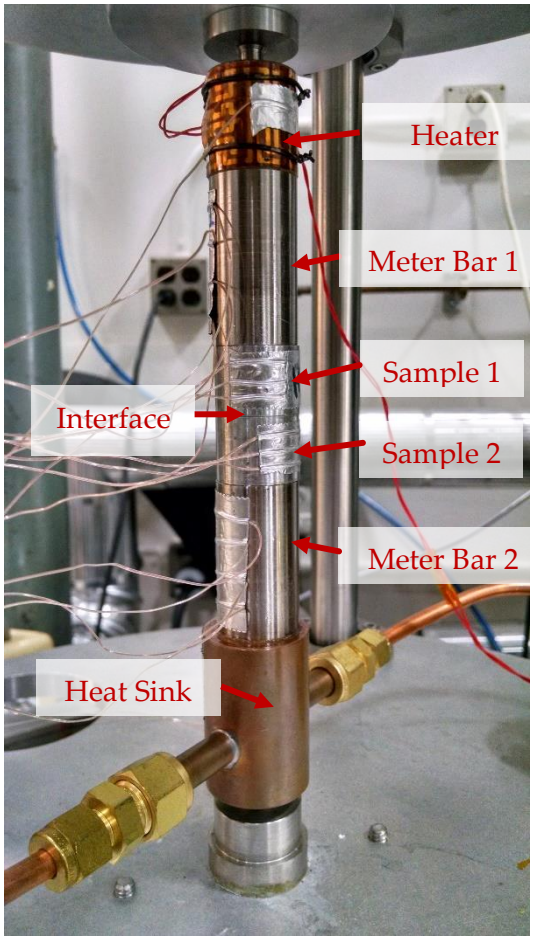

Fig. 4 Close-up photo showing details of the 2004 sample column.

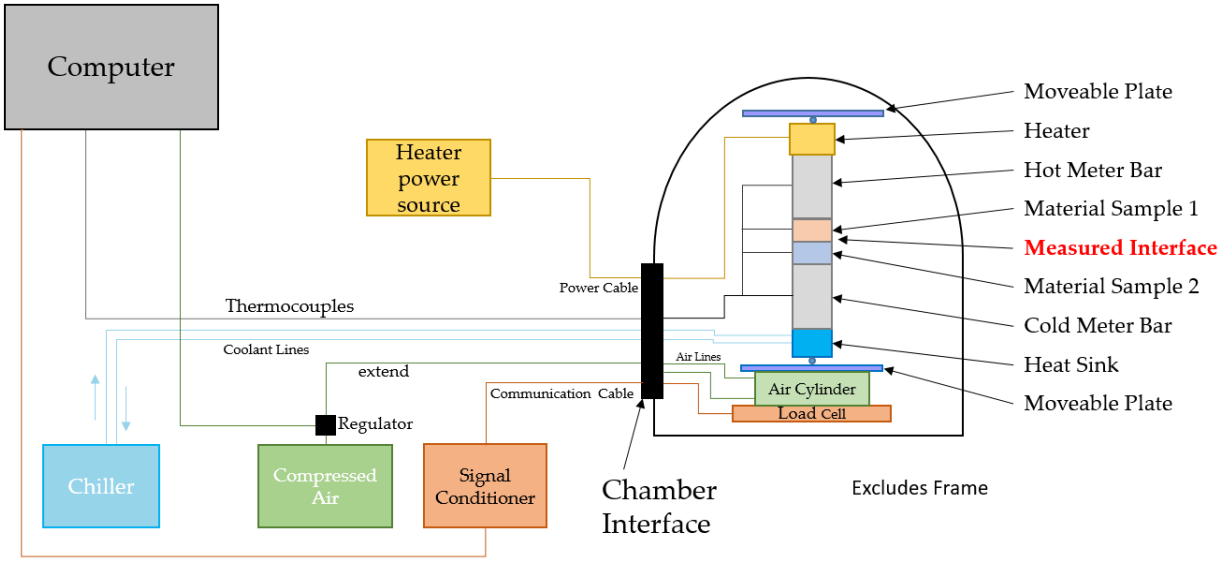

Fig. 5 Overall simplified schematic of the full system.

2.3 TWO METHODS FOR ESTIMATING CONTACT SURFACE TEMPERATURES

Since TCR cannot be measured directly, test fixtures have been designed and fabricated so that the temperature within the test articles can be utilized to infer the surface temperatures at the interface and the heat flux through the test articles. Contact resistance causes the temperatures of the interface surfaces to differ. This temperature difference can be employed in both TCR determination procedures (Eqs. (1) and (2), Section 2.1). The current method for finding the surface temperature at the interface has involved embedding at least three temperature sensors within the test articles at precise locations [8,19]. These three data points have been used to

extrapolate the temperature at each interface surface. One major issue with this method is that it does not take temperature dependent material properties into account, and therefore requires a degree of understanding of the uncertainty associated with the extrapolated values; this topic will be discussed in more detail subsequently.

By using an IHT technique the temperature can be estimated at a location where it cannot be directly measured [14,15]. This characteristic has made the method useful when trying to determine the surface temperature of thermal protective material for reentry vehicles [22]. When determining TCR, the interface surface temperatures cannot be measured since any alteration to the surfaces at the interface, such as embedding a TC, will produce an altered temperature value. The result is that IHT technique can be adjusted for use in TCR calculations. The inverse method utilizes temperature data that has been collected at two known locations within the test article of interest. During this study each test article was prepared so that three TCs were embedded in known locations for extrapolating the surface temperature; but only two of the three TCs were needed for IHT calculations.

3 CALCULATING INTERFACE SURFACE TEMPERATURES

3.1 EXTRAPOLATION METHOD

Since a TC cannot be placed on the surface of an interface to measure its temperature, the interface temperature can be estimate from temperature measured at other axial locations in the test article. By using a minimum of three locations where temperature is measured within a test article the surface temperature can be estimated by linear extrapolation. The linear extrapolation method utilizes a linear "best fit" based on the TC data and associated locations. Utilizing the precise interface distances from the TCs, the steady-state interface temperature can be estimated. The linear least-squares method for finding the "best fit" temperature variation to extrapolate the interface surface temperatures was employed. The basic equation for a line is as follows:

$$y = D + Bx \tag{3}$$

where the constants [23] D and B are

$$D = \frac{(\sum x^2 \sum y - \sum x \sum xy)}{N\sum x^2 - (\sum x)^2} \tag{4}$$

$$B = \frac{C\sum xy - \sum x \sum y}{C\sum x^2 - (\sum x)^2} \tag{5}$$

In this case, x is the distance along the test article measured from the opposite surface of the test article, y is the measured temperature, and C is the number of collection measurements, with three TCs, i.e C will be equal to three. A simple MATLAB code was written to calculate D and B values, along with the estimated surface temperature.

When the least-squares fits are compiled for both test articles, a graphical representation can be generated. Figure 6 is an idealized representation of two hypothetical temperature distributions through the test articles. Using linear extrapolation and the temperatures measured by TCs T_1 through T_3, the surface temperature T_A can be estimated. Similarly, temperatures T_4 through T_6 can be used to estimate surface temperature T_B. The temperature difference between

T_A and T_B is one of the important quantities needed, besides heat flux, to calculate the interface resistance.

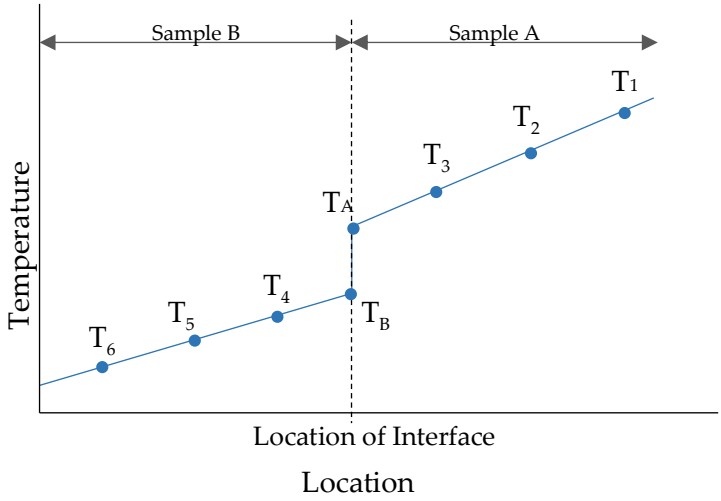

Fig. 6 Idealized representation of measured temperatures with the contact resistance effect.

3.2 INVERSE HEAT TRANSFER METHOD FOR CALCULATING SURFACE TEMPERATURE

By assuming that the TCR stack setup can be modeled accurately as a transient one-dimensional heat conduction problem, the interface surface temperatures can be estimated using a finite difference numerical method, specifically utilizing an IHT approach. IHT (also known as inverse heat conduction) uses space-marching finite difference and internally measured temperatures to estimate heat flux and surface temperature from internal temperature measurements [15,24]. This process involves marching from a point where the internal temperature is being measured to the contact surface by discretizing the distance between the TC location and the surface. There are two major steps involved in this procedure: (1) performing a direct solution of the 1D heat conduction equation between two internal locations where

temperatures can be measured and (2) using an inverse solution method (IHT) to estimate the surface temperature (Fig. 7).

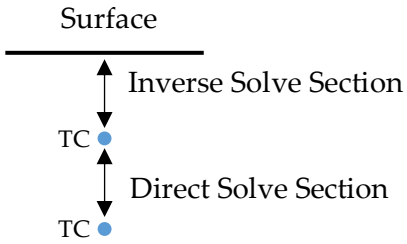

Fig. 7 Material sections related to applicable code sections.

3.2.1 DIRECT SOLVE CODE

By using basic heat transfer fundamentals and a control volume, an energy balance equation can be developed to calculate the instantaneous temperatures and heat fluxes. These equations can be applied to internal locations by discretizing the space between two locations where the temperature is being measured. This is one of two possible initial setup approaches for this type of problem; the other method utilizes the differential form of heat transfer equation. When using the energy balance equation, it is necessary to start with a one-dimensional control volume as shown in Fig. 8. The energy balance for the control volume is

$$\rho c_p V \frac{\partial T}{\partial t} = -q_{in} A + q_{out} A \qquad (6)$$

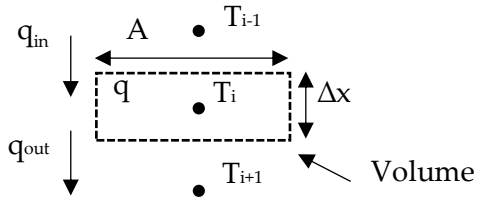

Fig. 8 Diagram used to identify basic heat transfer equations.

Using Fourier's law of heat conduction this can be written as Eq. (7):

$$\rho c_p V \frac{\partial T}{\partial t} = \left(kA\frac{\partial T}{\partial x}\right)_{in} + \left(-kA\frac{\partial T}{\partial x}\right)_{out} \quad (7)$$

(see Kreith and Black [25]). The required equations can be developed by starting with Taylor Series expansions to represent temporal and spatial derivatives, and by assuming uniform nodal spacing. In this study, the process ends by using the Crank-Nicholson implicit time marching method. The Crank-Nicholson implicit method is unconditionally stable and allows for flexibility in specifying the time step. The result is that the time step may be set to be equal to the TC sampling rate once the results are checked for accuracy. The implicit energy balance equation averages the current and future time step heat flux values entering and leaving each node, i.e.,

$$\rho c_p \Delta x \frac{T_i^{n+1} - T_i^n}{\Delta t} = \frac{1}{2}\left[k_{i-1}^n \frac{T_{i-1}^n - T_i^n}{\Delta x} + k_i^n \frac{T_{i+1}^n - T_i^n}{\Delta x}\right] + \frac{1}{2}\left[k_{i-1}^{n+1} \frac{T_{i-1}^{n+1} - T_i^{n+1}}{\Delta x} + k_i^{n+1} \frac{T_{i+1}^{n+1} - T_i^{n+1}}{\Delta x}\right] \quad (8)$$

where i represents nodal location, i = [1, 2, 3,…,I–1, I] and n represents the time step interval, n = [1, 2, 3,…,N–1, N]. The spacing between nodes (Δx) was the user-specified discretization, and the time interval (Δt) was matched with the data acquisition (DAQ) sampling rate.

The basic energy balance equation requires the temperature dependent thermal conductivity values for both current and future time steps. Since the change in temperature and thermal conductivity between consecutive time steps is small in the present testing procedure, only the thermal conductivity for the current time step was employed:

$$\rho c_p \Delta x \frac{T_i^{n+1} - T_i^n}{\Delta t} = \frac{1}{2}\frac{k_i^n}{\Delta x}\left[T_{i+1}^n - T_i^n + T_{i+1}^{n+1} - T_i^{n+1}\right] + \frac{1}{2}\frac{k_{i-1}^n}{\Delta x}\left[T_{i-1}^n - T_i^n + T_{i-1}^{n+1} - T_i^{n+1}\right] \quad (9)$$

Rearranging,

$$\frac{-k_{i-1}}{2\Delta x}T_{i-1}^{n+1} + \left(\frac{\Delta x \rho c_i}{\Delta t} + \frac{k_{i-1}}{2\Delta x} + \frac{k_i}{2\Delta x}\right)T_i^{n+1} - \frac{k_i}{2\Delta x}T_{i+1}^{n+1}$$
$$= \frac{\Delta x \rho c_i}{\Delta t}T_i^n + \frac{k_{i-1}}{2\Delta x}(T_{i-1}^n - T_i^n) + \frac{k_i}{2\Delta x}(T_{i+1}^n - T_i^n) \quad (10)$$

In this application the two TC locations, generating instantaneous temperatures, were at locations M1 and M2, shown in Fig. 9, and were treated as known boundary conditions. The space between M1 and M2 was discretized resulting in uniformly spaced interior nodes. The number of required nodes for an accurate solution is discussed in Section 4.4. Equations at M1+1 and M2–1 were treated differently from the remaining interior nodes since their neighboring node temperatures at M1 and M2 were known. Subsequently, the temperatures at each user-specified node location can be determined simultaneously via matrix inversion built into the MATLAB code.

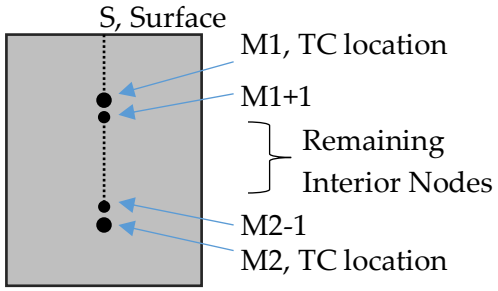

Fig. 9 Location of internal nodes in relation to temperature sensors.

There are four relevant equations that define the matrix. These equations were named so that they correspond with their locations within the matrix representation. For convenience, the

matrix representation of the four matrix elements governed by Eq. (10) have been represented using submatrix elements,

$$LD_i = -\frac{k_{i-1}}{2\Delta x} T_{i-1}^{n+1} \quad (11)$$

$$UD_i = -\frac{k_i}{2\Delta x} T_{i+1}^{n+1} \quad (12)$$

$$MD_i = \left(\frac{\rho c_i \Delta x}{\Delta t} + \frac{k_{i-1}}{2\Delta x} + \frac{k_i}{2\Delta x}\right) T_i^{n+1} \quad (13)$$

$$RHS_i = \frac{\Delta x \rho c_i}{\Delta t} T_i^n + \frac{k_{i-1}}{2\Delta x}(T_{i-1}^n - T_i^n) + \frac{k_i}{2\Delta x}(T_{i+1}^n - T_i^n) \quad (14)$$

so that

$$LD_i + MD_i + UD_i = RHS_i \quad (15)$$

Matrix inversion calculations start at node location M1+1, since node M1 (refer to Fig. 9) is the location with known temperature measured by TC and computations are terminated at node M2–1 since node M2 is the location with known measured temperatures at the other TC. The generalized tridiagonal matrix representation is as follows:

$$\begin{bmatrix} MD_{M1+1} & UP_{M1+1} & 0 & 0 \\ LD_{M1+2} & MD_{M1+2} & UP_{M1+2} & 0 \\ \vdots & \vdots & \vdots & \vdots \\ 0 & 0 & LD_{M2-1} & MD_{M2-1} \end{bmatrix} \begin{bmatrix} T_{M1+1}^{n+1} \\ T_{M1+2}^{n+1} \\ \vdots \\ T_{M2-1}^{n+1} \end{bmatrix} = \begin{bmatrix} RHS_{M1+1} + \frac{k_{M1+1}}{2\Delta x} T_{M1}^{n+1} \\ RHS_{M1+2} \\ \vdots \\ RHS_{M2-1} + \frac{k_{M2-1}}{2\Delta x} T_{M2}^{n+1} \end{bmatrix} \quad (16)$$

By utilizing MATLAB and starting at time $n = 1$, the matrix can be solved for the next time step so that the instantaneous temperatures at each node can be calculated concurrently before moving on to the next time step. Subsequently, the next time test-article TC temperatures at nodes M1 and M2 are introduced and, as seen in Eq. (16), are used to calculate the temperature between M1+1 and M2–1. Once the computed instantaneous nodal temperatures are determined, the transient heat fluxes are calculated using Fourier's Law between consecutive nodes. Once the matrix is solved for each time step, the temperature measured with the TC closest to the surface

(node M1) and the associated heat flux at that node are utilized to initiate the march to the surface (inverse solve section).

3.2.2 INVERSE SECTION OF THE CODE

Unlike the direct section, the inverse section of the code marches with the node location. For each node location the temperature and local heat flux is calculated while moving through each time step before moving to the next node. This results in a spatial marching scheme instead of a time marching scheme, i.e., the code is marching instantaneously to the surface. This section of the code employs the S6 Central Method of Carasso [15] as suggested by Pizzo et al. [14] because of its simplicity.

This code starts by using the temperature collected from the TC that is closest to the interface (M1 in Fig. 9), and the heat flux at node M1 that is found during the direct solve portion of the code. That is, at time, t_n, starting from M1 in Fig. 9 and moving to the surface, the adjacent node temperature is given by [15]

$$T_{i+1}^{n} = T_i^n + \Delta x \left[\frac{q_i^n}{k_i^n T_i^n}\right] \quad (17)$$

Then, allowing for transient nodal energy storage, the estimated instantaneous heat flux is given by [15]

$$q_{i+1}^{n} = q_i^n + \Delta x \rho c_p^n \left(\frac{T_i^{n+1} - T_i^{n-1}}{2\Delta t}\right) \quad (18)$$

When using IHT, the objective is to march in space and time to reach steady state while calculating heat flux and associated interface temperature. The interface temperature and heat flux are found for each time step.

The code generates two arrays containing the temperature and heat flux for each node (M1-1 to *S*) and each time step (n = 0 to N). For this application the surface temperature average during the last 5 minutes of testing was employed to calculate the TCR values.

3.2.3 CODE MODIFICATIONS FOR THERMAL CONTACT RESISTANCE CALCULATIONS

The basic IHT code for estimating surface temperature has been used primarily for surfaces subjected to extreme heating, e.g., heat shields and thermal protective surfaces [14]. For the common application of IHT, the matching is done in one direction. When IHT is used for TCR calculating the matching is in two different directions: marching up for the lower test article and down for the upper test article so that the calculations end at the interface (Fig. 10).

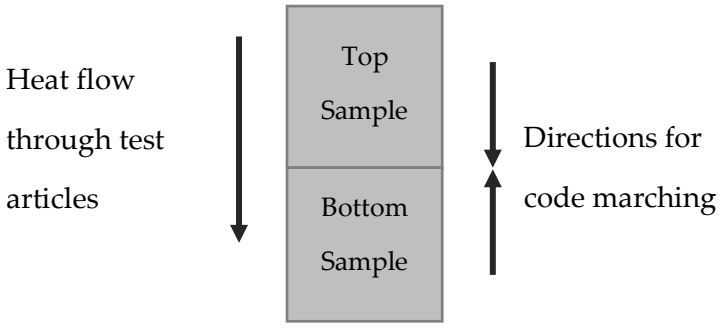

Fig. 10 Heat flow direction, showing directional marching conflict.

Data acquisition system was employed to collect the test article TC temperature measurements (at a user-specified sampling rate of one measurement per second). Representative upper and lower test article temperature data sets are shown in Fig. 11. While the one-second sampling rate is not discernable over the 10,000 data point plots, the data is noisy and there are numerous measurement spikes. The observed noise was problematic and considered to be atypical for this test apparatus. During tests performed outside of this study, data collected from the same system did not exhibit the temperature spikes shown in Fig. 11. Some degree of noise is expected for temperature measurements [26] and future work will need to identify other noise sources. Consequently, the collected temperature data for each test that was conducted was smoothed using the built-in MATLAB *Smooth Data Function*, the smoothed results for one of the TCR data collection test runs can be found in Fig. 12. The Smooth Data Function calculated a

running median over a window length of 20 data points (20 seconds) with the center being about the current and previous data points [27]. The smoothed data were employed in estimating the interface surface temperatures for comparisons between both TCR methods, and also for calculating heat fluxes.

The code ran for the full duration of the test data. The interface temperatures and heat flux were calculated for each time step, then the averages were found for the last five minutes (300 test points) of data. The average values were employed to determine the interface surface temperatures and associated heat fluxes. The resulting surface temperature difference and heat flux estimates permitted direct calculation of TCR. The MATLAB TCR code (Appendix, Section I) accepted LabView data files as input, then calculated the interface surface temperatures employing both IHT and extrapolated methods, as discussed in Section 3.1.

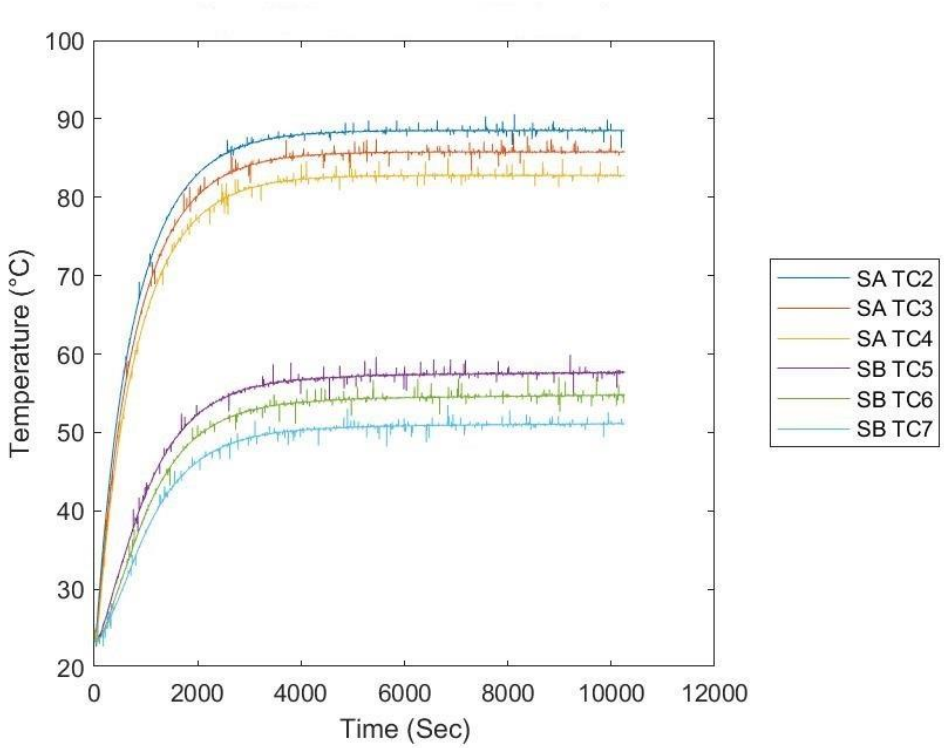

Fig. 11 Raw data plot of temperature data collection test run.

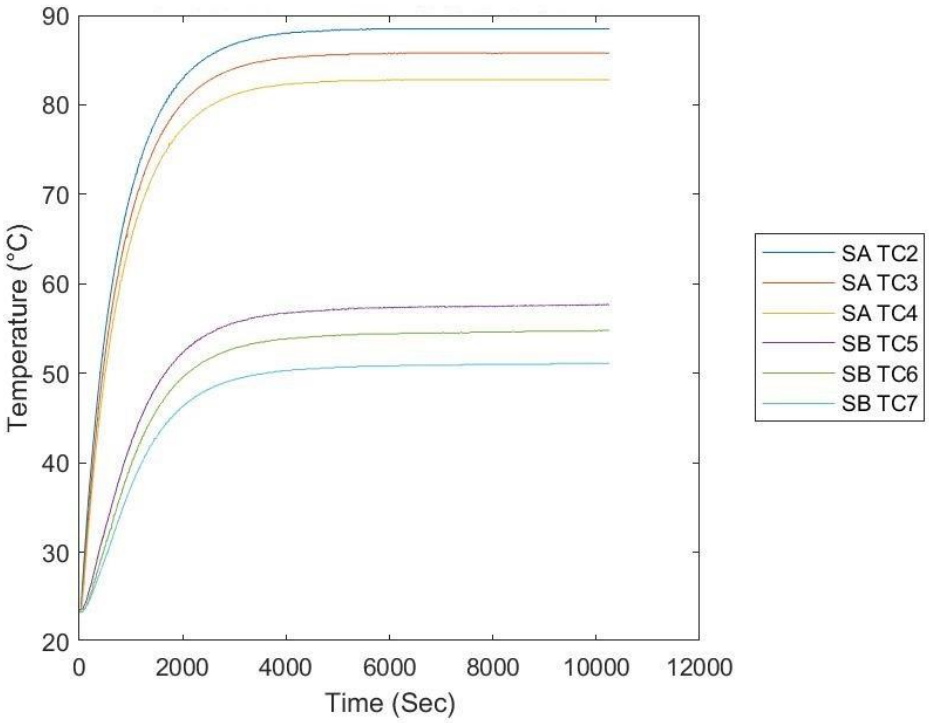

Fig. 12 MATLAB smoothed data for same test run presented in Fig. 11.

4 INVERSE HEAT TRANSFER CODE VERIFICATION TESTS

4.1 INTRODUCTION

To establish confidence in the IHT methodology, a simple test was developed to verify the results obtained with the IHT code. The test article was a cylindrical SS304 sample with the same dimensions as the test articles for TCR data collection, with strategically embedded TCs in the test article, and a disk resistance heater. This test did not use the TCR sample column or test fixture. Instead it involved embedding the TCs in the test article, adhering a TC to the surface, and then adhering the disk heater over the surface TC. The prepared test article was then placed on a piece of Teflon in the Stainless Steel Bell Jar. The intent was to compare the measured surface temperature to the surface temperature calculated using either the IHT code or the extrapolated technique. This test was used to evaluate the accuracy and related uncertainties of the IHT and extrapolated technique to estimate surface temperatures from axially located temperature measurements.

Test preparation setup involved using conductive adhesive to ensure proper thermal contact between a T-type TC and the flat top surface of a cylindrical SS304 test article. LaRC technicians were able to ensure appropriate proximity of the TC to the test article surface so that the surface temperature could be measured with minimal distortion. A Minco 70.1-ohm resistance disk heater without pressure-sensitive adhesive was then bonded, using the same conductive adhesive that was used for the TC, to the same surface that the surface TC (TC-T in Fig. 13) was bonded to. Two TCs were also embedded along the axis of the test article to provide temperatures at various axial locations in the test article.

The SS304 cylinder had a diameter of 24.1 mm and a length of 25.3 mm and was prepared for the test by drilling two 0.9 mm diameter blind holes perpendicular to the center axis, to a depth of 12.1 mm, equivalent to the test article radius. The two blind holes were located so that they were equidistant from each other and between the top and bottom surfaces, i.e., approximately 6.5 mm, see Fig. 13 for details. Two T-type TCs were inserted in the holes and held in place with Apiezon N thermal grease, filling any voids; aluminum tape wrapped around the circumference of the test article as a secondary method of securing the TCs. A third TC was taped

to the bottom surface with Kapton tape, and care was taken to make sure that the sensing junction was maintained on the bottom surface of the test article.

The test cylinder was placed on a 3 mm thick Teflon pad and located within the Stainless Steel Bell Jar (Fig. 14). Teflon is a common material that is used by the vacuum facility for thermal and electrical isolation within the vacuum chambers. Teflon has a relatively low thermal conductivity, greatly reducing thermal exchange with the vacuum chamber base. Since a radiation covering was not included, future studies will need to evaluate for radiation losses from the vertical surface of the test article. Since the resistance heater had a maximum temperature limit of 150˚C [28], the maximum temperature measured by TC-T was required to be below 150˚C to protect the heater.

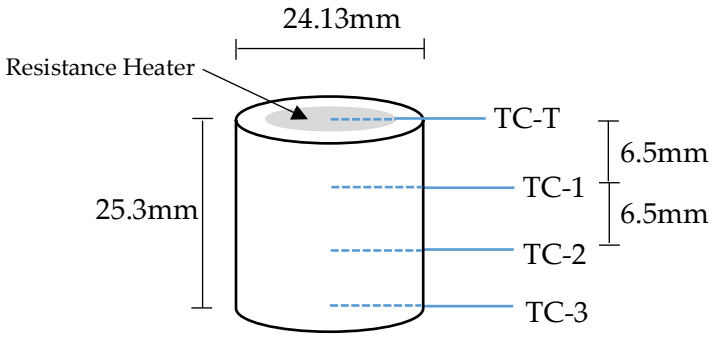

Fig. 13 Configuration for SS304 code verification test cylinder.

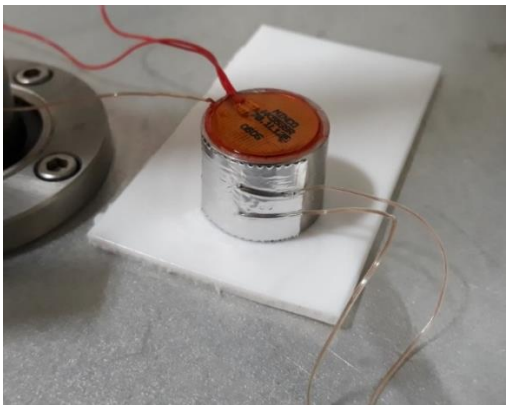

Fig. 14 Actual verification test setup within the Stainless Steel Bell Jar.

The vacuum chamber was operated at a nominal pressure of 10^{-2} Torr for these verification tests. After pumping the chamber to the desired vacuum range, the resistance heater was activated, and data collection began. Subsequently, the system was operated until thermally steady state conditions were achieved. The DAQ system sampled all four TCs once a second for the test duration. The data were collected for a minimum of 6 hours and then checked for thermal stability by looking at the rate of temperature change over a period of time prior to test termination. Three different verification tests were conducted so that thermal data sets could be collected for three different heater power supply settings. The test article was allowed to cool back to ambient temperature between each successive test. Each test generated a temperature data set starting from ambient conditions and proceeding to steady state by the end of the data set.

The collected data from TC1 and TC2 were used to estimate the temperature of the surface on which the heater was bonded. The calculated values were compared to the measured surface temperature recorded by TC-T. This process involved using a MATLAB Smooth Data function prior to the use of the IHT code. The default appeared to eliminate the anomalous, non-physical temperature spikes and was used for each set of test results. Once the surface temperature was estimated for all time steps, an overall average surface temperature was found by taking the average of data over the last 5 minutes of recorded data. This resulted in estimated average steady state surface temperatures for the three heater power settings used in these tests. The code not

only calculated the average steady state surface temperature with IHT but also estimated the surface temperature using the extrapolation method. IHT utilized the two embedded TCs while the extrapolation method used both embedded TCs along with TC-3, located at the bottom of the test article. This allowed for both values to be compared with the measured surface temperature (TC-T in Fig. 13).

4.2 PROCEDURE

The three different heater power settings provided three different data sets that could be used to calculate the surface temperature. The settings that would be used for the heater power supply were determined through preliminary tests and each test was conducted with the power supply set to constant voltage. The TC leads and the heater lines were connected externally utilizing several chamber wall penetration plates. A roughing pump was employed to achieve vacuum pressures at or below 10^{-2} Torr (mid-vacuum range).

When the vacuum threshold was achieved a new data file was generated using the LabView interface maintained on the Bell Jar computer so that the temperature data would be recording when the heater power supply was activated. At the time of heater activation, the sudden change in temperature indicated by TC-T was used to verify heater operation. Each test ran for a minimum of 6 hours with a steady-state check being conducted prior to shutting off the heater. This process was followed until all three tests were completed.

After completing the tests, the temperature data for each test was used, along with the IHT MATLAB code, to estimate the surface temperature and perform a nodal convergence study. The estimated surface temperatures from the IHT code and extrapolation technique were compared to the measured temperatures.

4.3 NODAL CONVERGENCE STUDY

One attribute of numerical solution techniques is that the sections between the TCs are discretized and the temperature and heat flux could thus be calculated at each node. The question

was, "How many nodes are required for the results to be as accurate as possible?" This was determined by conducting a nodal convergence study and comparing the results based on the number of nodes. An optimum number of nodes was determined for the verification code; the number of nodes was carried over into the TCR IHT code and then verified a second time.

Results produced from the code written for the verification test were used to identify the appropriate node count starting with 20 nodes in the direct section. The node count was doubled for each run ending with 640 nodes. The 8V test data was used for this study and the temperature of the center node was observed and compared each time the node count was increased. The temperature of the center node only changed by 0.01°C each time the number of nodes was doubled; this was consistent with each increase in node count. Since the calculated temperatures resulted in little change the heat flux between the two TCs and the calculated IHT heat flux through the surface were compared as each node count increased and the convergence was observed; resulting in the heat flux being used to determine the node count. As the node count increased, the IHT calculated heat flux at the surface approached the heat flux that was calculated between the two control TCs. Since the heat flux at the surface should finally approximate the steady-state heat flux between the two TCs, that convergence toward the calculated heat flux indicated nodal convergence.

The variation of IHT calculated surface heat flux with the number of nodes used in the numerical model is displayed in Fig. 15. The 80- and 160-node results are not shown because the largest changes occurred between the lowest and highest node counts. As the numerical resolution was refined, the IHT heat flux converged toward the steady-state heat flux based on the embedded control TCs. That convergence effect is most obvious between 20-node and 40-node cases in plots (a) and (b) in Fig. 15, the change becomes less significant as the number of nodes was increased by factors of 16 or more.

Comparing heat flux histories, the 320- and 640-node results exhibited only minimal influences. Once the node count exceeded 160 nodes, the difference between heat flux histories was less than 2 W/m^2 (0.2%) based on imposed test article heat flux levels between 1150 and 1200 W/m^2. The instantaneous heat flux difference over the full data collection duration can be seen in Fig. 16, where the difference between the two heat fluxes is plotted. When the node quantities

were 80, 160, 320, and 640, the percent difference between the two heat fluxes over the last 5 minutes of data collection falls below 1% (Table 1).With 160 nodes the average percent difference was well below 0.5% and so 160 nodes was used in the TCR code where both interface surface temperatures are estimated.

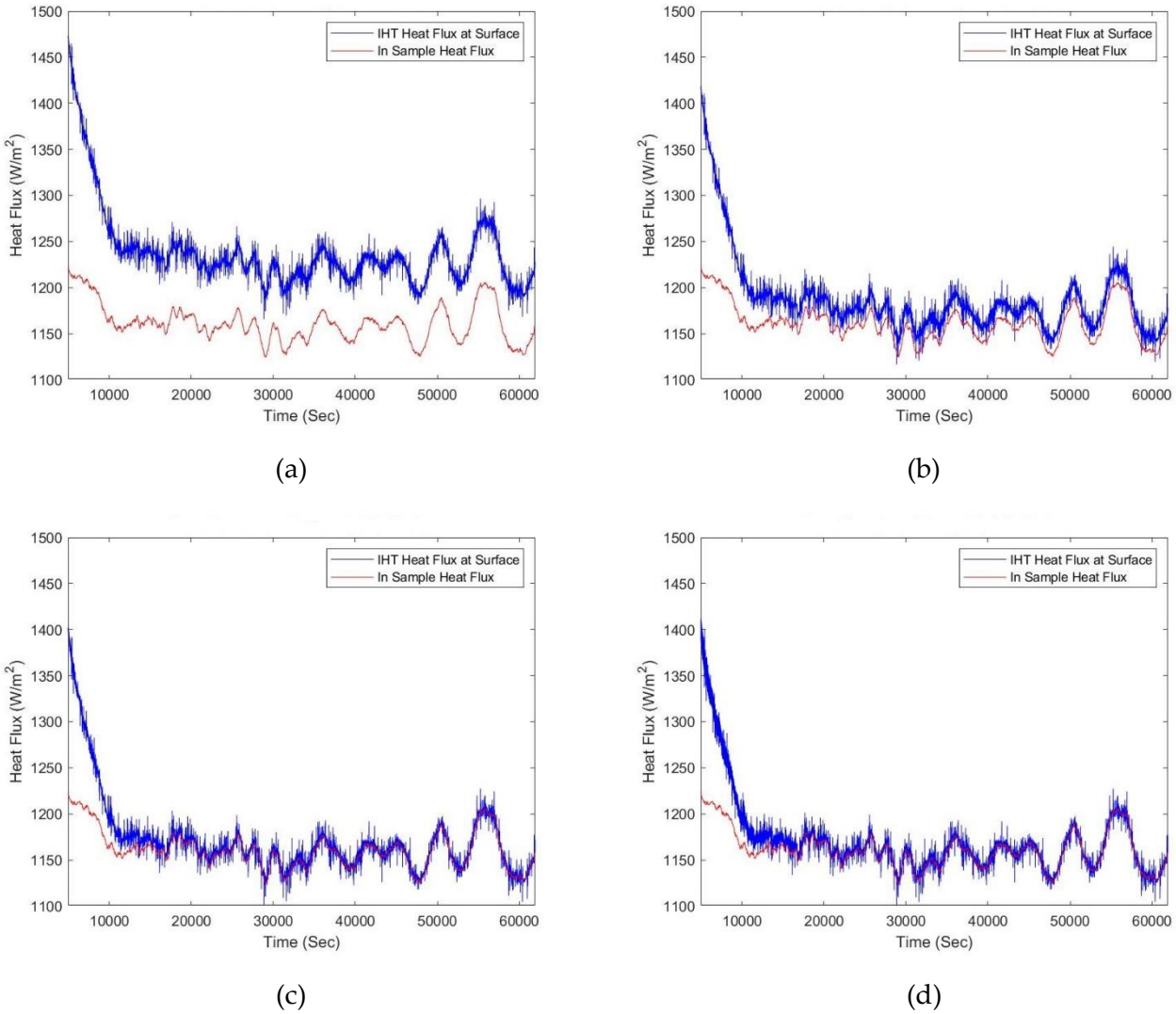

Fig. 15 Heat Flux vs. number of nodes for 8V verification test; (a) 20 nodes, (b) 40 nodes, (c) 320 nodes, (d) 640 nodes.

Table 1Average percent difference between IHT heat flux and heat flux calculated using embedded TCs for each quantity of nodes over last 5 minutes of data collection.

Node Count	Average Percent Difference
20	5.61
40	1.44
80	0.40
160	0.14
320	0.08
640	0.06

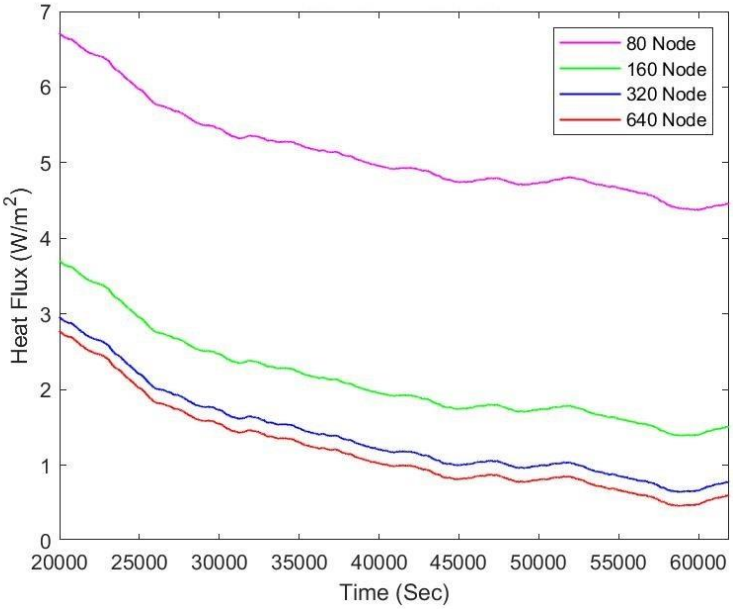

Fig. 16 Difference between heat flux calculated by IHT code and heat flux calculated using embedded TCs for each node count.

4.4 RESULTS AND DISCUSSION

The estimated average steady-state surface temperature found using both methods and the average of the measured surface temperature collected from TC-T for the last 5 minutes of data are presented in Table 2, as well as the standard deviation for both values. It was found that the estimated surface temperature calculated with IHT resulted in values that were closer to the

measured temperature than when the surface temperature was extrapolated. The percent difference between the measured surface temperature and both estimates is presented in Table 3. Not only does the extrapolated estimate have a greater difference, but the difference increased with increasing temperature.

A graph of the measured and estimated surface temperature along with the embedded TC temperatures for the full test duration when the heater voltage was set to 4V can be found in Fig. 17. The measured surface temperature and the IHT estimate are graphically indistinguishable. Fig. 18 plots the difference over time between the measured and IHT estimated surface temperature since they were otherwise too close together in Fig. 17. Plotted results for the 6V and 8V tests are found in the Appendix, Section C.

As the temperatures stabilize within the test article, the difference between the estimated and measured surface temperatures for the 4V results became more consistent and averaged around 0.02°C in Fig. 18. Since the IHT surface temperature results were so close to the measured results, this indicates that the implementation of IHT for this data was correct and will produce results that can be employed to calculate TCR values.

The IHT calculated surface heat flux and the heat flux found by using the embedded TC data and Fourier's Law are both graphed in Fig. 19. Over time, the IHT heat flux approaches the heat flux found using Fourier's Law (Eq. 2). Towards the end of the test the difference is hardly perceivable in Fig. 19 indicating that thermal stability had been achieved. The heat flux for each voltage setting is found in Table 4. Presented in the same table is the difference between the two heat fluxes. The results were calculated after the nodal convergence test, presented in Section 4.3, was completed.

Table 2Estimated surface temperatures.

Heater Power Supply Settings			Measured Surface Temperature (°C)	Surface Temperature			
				Estimated with IHT Code		Estimated with Extrapolation	
Voltage (V)	Amps (A)	Resulting Power (W)		Average Temperature (°C)	Standard Deviation	Average Temperature (°C)	Standard Deviation
4	0.056	0.224	47.1	47.1	0.0013	48.5	0.0014
6	0.084	0.504	72.1	71.9	0.0005	74.9	0.0004
8	0.112	0.896	100.7	100.3	0.0024	105.1	0.0009

Table 3 Percent difference between estimated surface temperatures and measured.

Heater Voltage (V)	Percent Difference	
	With IHT Code	With Extrapolation
4	0.04%	2.93%
6	0.25%	3.78%
8	0.35%	4.32%

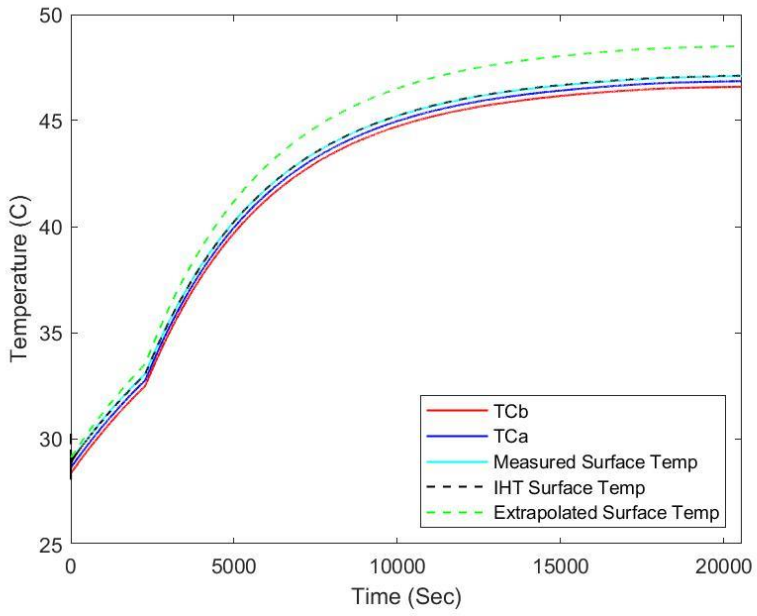

Fig. 17 Temperature over time for 4V validation test (TCa represents TC-1 and TCb represents TC-2 in Fig. 13).

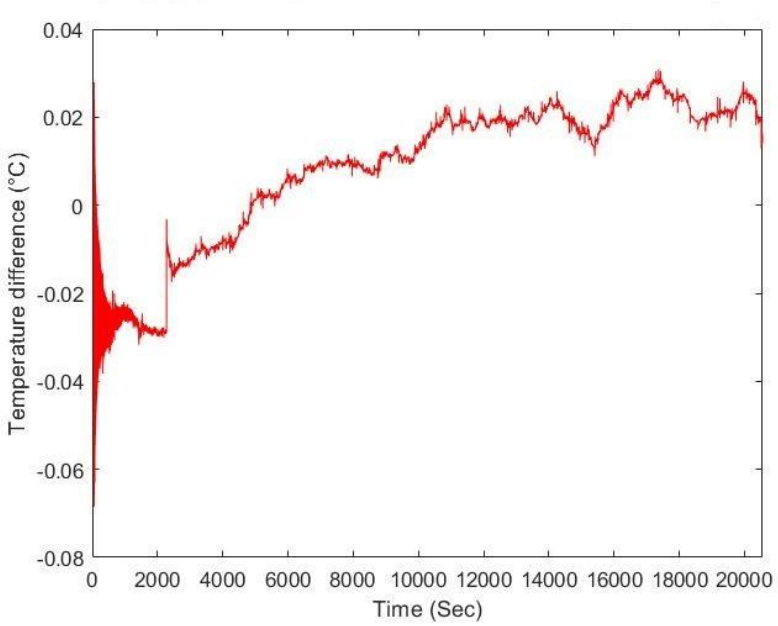

Fig. 18 Difference between estimated surface temperature and measured surface temperature for 4V test.

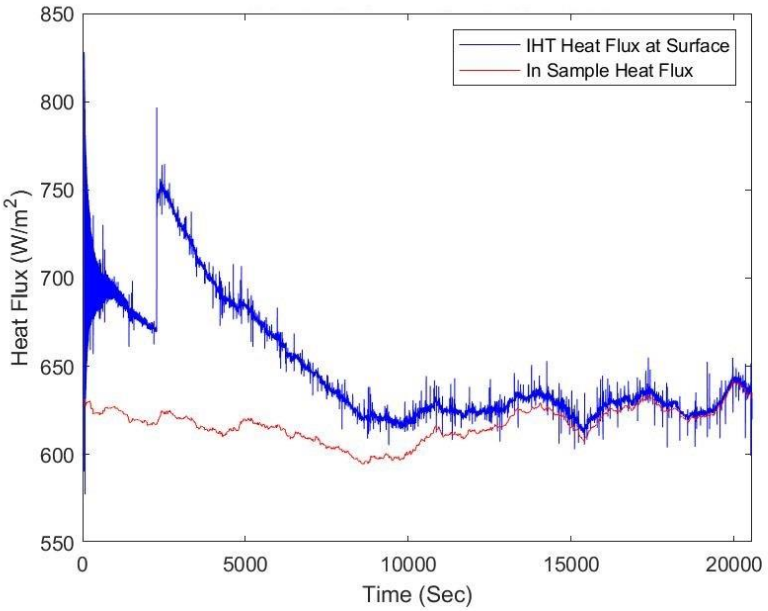

Fig. 19 Heat flux over time for both IHT surface heat flux and heat flux found using embedded TC data (In Sample) for 4V test (160 nodes).

Table 4 Heat flux for each heater power supply setting for the verification test found using IHT code and Fourier's Law.

Heater Voltage (V)	Heat Flux (W/m^2)		
	IHT Average	In-test article [a]	% Difference
4	683.5	635.3	7.6
6	1062.9	747.0	42.3
8	1564.0	1152.4	35.7

a. Found using embedded TCa and TCb

5 DATA COLLECTION FOR CALCULATING CONTACT RESISTANCE

The original test setup from 2004 utilized two Invar Meter Bars in the test article stack. What was discovered through the initial literature review was that the number of Meter Bars can vary. Two Meter Bars must be used for anisotropic material test articles [7], while other research only used one Meter Bar when testing isotropic materials [10,29]. Because SS304 is an isotropic material, it was chosen as the test article material for this study; therefore, only one Invar Meter Bar was necessary for experimental testing (Fig. 20). The choice to include one Meter Bar was also part of an attempt to match the test setup presented by McWaid [2]. The relatively low SS304 thermal conductivity produced a robust temperature gradient along the test article length.

McWaid's [2] dissertation contains detailed information regarding which material he selected for specific components (including the test articles) and how the interface surface finish was produced and characterized. Measured temperatures down his sample column, along with TC locations, were included in his dissertation. Many other published works lacked key details that McWaid included; many of the excluded details are either related to surface preparation or temperature gradients that were experienced during testing.

McWaid's sample column did have some differences from the one employed in this study: Meter Bar material (Austenitic Stainless Steel), TC count in individual components, and lengths of the test articles and Meter Bar. McWaid also added insulating material to the top of the heater prior to placing it in the test fixture to minimize heat loss. His dissertation lacked the actual set temperature of the water coolant bath. Unfortunately, all of these differences precluded matching McWaid's temperatures in the test articles and Meter Bar during testing. Care was taken in this study to identify the heater power supply settings and coolant bath temperature that were required to produce thermal gradients that approximated McWaid's. The heater power supply was set to constant voltage control at 20V, while the coolant bath was held at 18°C. With these settings the temperatures approximated the McWaid data, but did not match exactly.

For this study, two cylindrical test article sets, resulting in a total of four SS304 test articles, were used to collect TC data in a vacuum environment. Two sets of test articles were used so that the results are not completely dependent on only one test article set. Upon test completion, the

collected TC data was then processed using the MATLAB code, which included estimating the interface surface temperature both with IHT and extrapolation. Then the two results for interface surface temperatures at each test point was compared prior to their use in calculating TCR.

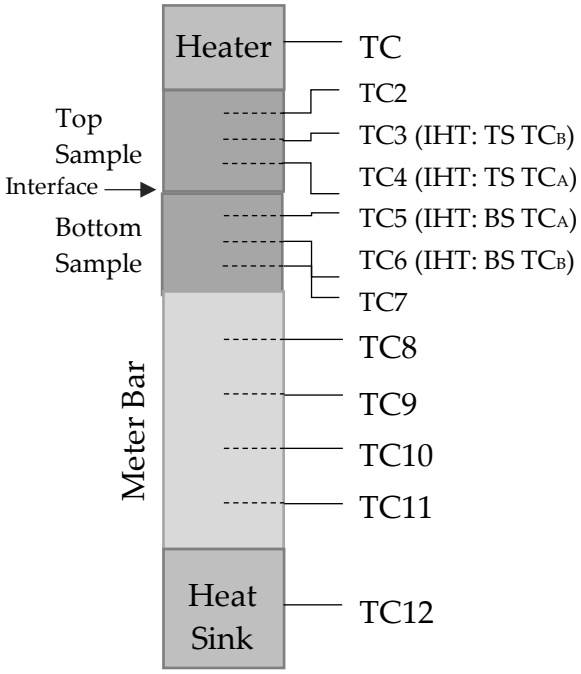

Fig. 20 Sample column with TC numbers used for experimental tests and TC labels for IHT calculations.

Since the IHT code allows for temperature dependent material properties, both the thermal conductivity and specific heat for SS304 are needed. Using material property data collected by Yeram Touloukian [20,30], a relationship with the temperature of the material was identified by curve-fitting data using third-order polynomials (this can be found in the Appendix, Section B). The third-order polynomial equations were used in IHT calculations and when Fourier's Law was used to calculate heat flux.

Even though three TCs were embedded in each test article, only two are needed for IHT analysis. During the application of the IHT section of the MATLAB code, the temperature

histories of the two embedded TCs located closest to the interface surface of each test article was employed. The temperature histories for the same two TCs were also used to calculate the heat flux in the test articles at each time step with the average being taken over the last 5 minutes of the total data set. The average was then used to calculate TCR. All three TCs that were embedded in each test article were also used to extrapolate the interface surface temperature of each test article.

For this study only six of the 10 compressive forces used by McWaid were used as test points since not all forces could be achieved by the test setup; the limiting factor being that the facility air pressure was too low to match McWaid's higher forces. The compressive forces that were used for each step are found in Table 5. This table also contains interface pressures found by dividing the compressive force by the cross-sectional area of the test articles; interface pressures are usually reported with TCR results. The compressive force system was designed with a PID controller so that it could accommodate thermal expansion of the sample column while holding the set value.

A total of 16 tests were conducted; the initial plan was that each test would have six different compressive forces. Once the testing was concluded, seven tests had the full six test points. Three tests were lacking either the initial or the final test points. The main cause for the unplanned loss of test points was primarily because the air cylinder malfunctioned resulting in the system not being able to compensate for thermal expansion. The malfunction was corrected by lubricating the air cylinder and providing 5 psi of facility air to generate an air spring in the retract chamber. Five tests labeled as "extra" tests, were planned to only have three of the six test points.

More tests were planned, but unfortunately the vacuum chamber is a shared chamber and the available time only allowed for the 16 tests. There were two test series: the first series consisted of 12 tests and the second with the remaining four. The second set was conducted after the data from the first set had been analyzed.

Table 5 Test step number with associated compressive force and interface pressure.

Step Number	Compressive Force (N)	Interface Pressure (MPa)
1	72	0.159
2	221	0.489
3	643	1.421
4	1015	2.244
5	1457	3.221
6	1816	4.014

5.1 TEST SET ONE, INTRODUCTION

As reported, the first test set consisted of 12 tests. Six of the 12 tests were planned to include all six of the planned compressive force applications and were executed at a mid-vacuum range of 10^{-2} Torr. The remaining tests were either conducted at high vacuum or involved changing the location of the test articles in the stack and running at the mid-vacuum range.

5.1.1 PROCEDURE

The four test articles of SS304 were drilled with blind holes for the placement of three 36-gauge T-type TCs along the centerline of the cylinders. This was followed by polishing both flat surfaces of all test articles; once completed, both surfaces were protected with Kapton tape. One flat surface remained protected with Kapton tape while the other had the tape removed so that it was bead blasted with glass bead having a diameter rage of 0.0089–0.015 cm (0.0035–0.0059 in); the bead blasted surface became the interface surface for all test runs. The interface surface was protected so that it was not altered prior to testing. The TCs were then embedded in each of the test article materials and the Invar Meter Bar (labeled #2 from the legacy test setup) using Apiezon N vacuum grease and aluminum tape, following the same process that was discussed in Section 4. A TC was also attached to the side of the heat sink and heater using Kapton or Aluminum tape. These TCs were used to monitor the heater and heat sink during testing to verify that they were operating. This resulted in a total of 12 TCs collecting data for the sample column.

Along with the TC data the compressive force reported from the load cell and pressure of the chamber was also recorded for the total duration of each test. During testing the start time for each step, the target compressive force, the amperage for the heater power supply, chamber pressure, and any extra notes about the test run were recorded by hand in a log book. The LabView software was setup so that TC data would be collected every second.

The sequence for the testing started with bringing the Bell Jar to the desired vacuum level. Once the chamber reached the target vacuum range, the compressive force was set to the required load, a data file was generated, and data collection started. The heater power supply was set so that the voltage was 20V. A detailed procedure can be found in the Appendix, Section H. The system was considered to be at steady state when all temperatures had a deviation of 0.5° C/hr [31]; this was verified by manually entering TC data into an Excel sheet setup to check equilibrium with data being collected about every 10 minutes. Several tests were allowed to run over night and these tests were checked for equilibrium the following morning.

Each test started with the lowest compressive force. Once equilibrium was reached, the force was increased to the next compressive force test point (or step) and the time that the change was made was recorded. The minimum test point duration was determined to be one hour and 15 minutes. If equilibrium was reached prior to the minimum duration the test did not proceed to the next test point until the minimum duration was reached. When steady state was reached after the minimum test length, then the test was allowed to run 10—15 minutes longer. This was repeated until data was collected for all test points.

Only one test article set could be tested at a time; this allowed for one set to be bead blasted while the other was being used for testing, providing fresh interface surfaces for each test. In order to assure that the full surface was refinished the interface surface was marked with a marker and then bead blasted until the marker was completely removed.

Table 6 is the test matrix that was used for the tests that were run at a mid-vacuum level. Table 7 is the test matrix for the extra tests that were added to the Test Set One matrix after the mid-vacuum tests were concluded. The six mid-vacuum tests were conducted alternating between test article sets as listed in Table 6. For these tests the lower number test article was always the top test article in the stack. Once all six test runs were completed, three additional tests

were conducted with the test article locations swapped and the number of compression force steps decreased to three, see Table 7. The testing campaign was concluded with two tests with the chamber at high vacuum and the test article positioned in the same orientation as the six mid-vacuum tests. A third high-vacuum test was conducted but unexplained anomalies in the data resulted in it being unusable.

After completing each test, the data file was sectioned into individual files for each test point (step) by matching the start times for each time the compressive force was changed. The individual test point files were then analyzed with the MATLAB code.

Table 6 Mid-vacuum test matrix for test set one.

Test number	Top Sample	Bottom Sample	Chamber Pressure Range	Number of compressive force steps
Test1 S1S2	1	2	10^{-2} Torr	6
Test1 S3S4	3	4	10^{-2} Torr	6
Test2 S1S2	1	2	10^{-2} Torr	6
Test2 S3S4	3	4	10^{-2} Torr	6
Test3 S1S2	1	2	10^{-2} Torr	6
Test3 S3S4	3	4	10^{-2} Torr	5

Table 7 Test matrix for extra tests for test set one.

Test number	Top Sample	Bottom Sample	Chamber Pressure Range	Number of compressive force steps
Test4 S2S1	2	1	10^{-2} Torr	3
Test4 S4S3	4	3	10^{-2} Torr	3
Test4 S2S1 Redo	2	1	10^{-2} Torr	3
HighVac S1S2	1	2	10^{-5} Torr	3
HighVac S3S4	3	4	10^{-5} Torr	3
HighVac S3S4 Redo	3	4	10^{-5} Torr	3

The DAQ system had set numbers for each TC port. Throughout testing, the same port was used for each TC location along the sample column. Location of TCs and DAQ associated numbers can be found in Table 8.

Table 8 Thermocouple location with DAQ number.

Location	DAQ System Number
Heater	1 or 18
Top Sample Top	2
Top Sample Middle	3
Top Sample Bottom	4
Bottom Sample Top	5
Bottom Sample Middle	6
Bottom Sample Bottom	7
Meter Bar Top	8
Meter Bar Middle Top	9
Meter Bar Middle Bottom	10
Meter Bar Bottom	11
Heat Sink	12

5.2 TEST SET TWO, INTRODUCTION

After evaluating the results from the first test set four more tests were planned. This added two more tests for each test article set. These tests were added to increase the statistical relevance for the final results. To stay consistent, all four tests were executed at the mid-vacuum range. This group of four test articles had more quantitative surface finish data collected prior to testing, such as measuring the root-mean-square (RMS) deviation, the peak-to-valley height (PV), and the roughness average (RA) values for each test article. This was not done during the first test set because it was assumed that the surface preparation was all that was needed in order to compare the results to published data. This could have been done after the first test set but there was concern that the surface characteristics would be changed by the compressive force used during

the tests. By including the RMS measurement, the literature results could be expanded to include a variety of studies with comparable surface roughness.

5.2.1 PROCEDURE

The procedure for the second set of test runs followed the same as the first but included measuring the surface roughness. This was done after each test article was bead blasted (before running the test), after the test was run, and then after being refinished. The surface roughness measurements can be found in the Appendix, Section E. The test matrix can be found in Table 9.

Table 9 Test matrix for second set of tests.

Test number	Top Sample	Bottom Sample	Chamber Pressure Range	Number of compressive force steps
Test5 S1S2	1	2	10^{-2} Torr	4
Test5 S3S4	3	4	10^{-2} Torr	6
Test6 S1S2	1	2	10^{-2} Torr	6
Test6 S3S4	3	4	10^{-2} Torr	5

5.3 RESULTS AND DISCUSSION

The collected data for all tests was used to estimate the interface surface temperature for each test article and heat flux for each step of each test. All of the surface temperature results for the mid-vacuum range test for the test article 1 and 2 test set are found in Table 10, and the results for the test article 3 and 4 test set are found in Table 11. Table 12 contains the results for the high-vacuum tests, and the tests where the test article location was swapped in the test column. The code also included calculating the random uncertainty in the estimated interface surface temperatures for both methods. The total uncertainties in the estimated surface temperatures are also presented in each table, though details about the uncertainty analysis are presented in a later section of this document.

Table 10 Estimated surface temperatures and total uncertainty for each mid-vacuum test for test article 1 and test article 2.

		IHT Estimated Surface Temperature (°C)				Extrapolated Estimated Surface Temperature (°C)			
Test Run	Pressure (MPa)	Top Sample	Top Sample Uncert-ainty	Bottom Sample	Bottom Sample Uncert-ainty	Top Sample	Top Sample Uncert-ainty	Bottom Sample	Bottom Sample Uncert-ainty
Test 1	0.159	79.81	±0.2	63.54	±0.3	80.21	±3.3	63.41	±2.4
	0.489	72.97	±0.2	63.66	±0.2	73.38	±3.1	63.51	±2.4
	1.421	68.03	±0.2	63.80	±0.2	68.42	±2.9	63.68	±2.4
	2.244	67.00	±0.2	64.28	±0.3	67.39	±2.8	64.19	±2.4
	3.221	66.26	±0.3	64.17	±0.3	66.63	±2.8	64.11	±2.4
	4.014	65.84	±0.2	64.17	±0.2	66.21	±2.7	64.09	±2.4
Test 2	0.159	79.92	±0.2	59.01	±0.2	80.14	±3.0	58.83	±2.2
	0.489	74.72	±0.2	60.76	±0.2	74.93	±2.8	60.59	±2.3
	1.421	69.55	±0.3	62.12	±0.2	69.74	±2.6	61.97	±2.3
	2.244	68.15	±0.2	62.80	±0.2	68.35	±2.6	62.64	±2.4
	3.221	67.06	±0.2	62.96	±0.2	67.25	±2.5	62.81	±2.4
	4.014	66.50	±0.2	63.02	±0.2	66.67	±2.5	62.87	±2.4
Test 3	0.159	79.43	±0.2	61.40	±0.2	79.63	±3.0	61.35	±2.3
	0.489	74.80	±0.2	62.59	±0.2	75.02	±2.8	62.52	±2.3
	1.421	69.87	±0.1	63.96	±0.2	70.07	±2.6	63.89	±2.4
	2.244	68.50	±0.2	64.65	±0.2	68.71	±2.6	64.57	±2.4
	3.221	67.47	±0.2	64.75	±0.2	67.67	±2.6	64.68	±2.4
	4.014	66.91	±0.1	64.77	±0.2	67.11	±2.5	64.68	±2.4
Test 5	1.421	72.68	±0.2	62.67	±0.1	72.57	±2.7	62.44	±2.4
	2.244	70.95	±0.2	63.31	±0.1	70.83	±2.7	63.10	±2.4
	3.221	69.69	±0.1	64.03	±0.2	69.55	±2.7	63.83	±2.4
	4.014	68.94	±0.2	64.21	±0.2	68.79	±2.6	64.01	±2.5
Test 6	0.159	81.43	±0.2	60.85	±0.1	81.70	±3.1	60.69	±2.3
	0.489	76.68	±0.2	61.35	±0.2	76.97	±3.0	61.26	±2.3
	1.421	71.85	±0.2	62.25	±0.1	72.14	±2.8	62.18	±2.3
	2.244	70.22	±0.2	62.45	±0.2	70.51	±2.8	62.41	±2.3
	3.221	69.10	±0.2	62.74	±0.1	69.38	±2.7	62.72	±2.3
	4.014	68.51	±0.2	62.84	±0.1	68.79	±2.7	62.84	±2.3

Table 11 Estimated surface temperatures and total uncertainty for each mid-vacuum test for test article 3 and test article 4.

		IHT Estimated Surface Temperature (°C)				Extrapolated Estimated Surface Temperature (°C)			
Test Run	Pressure (MPa)	Top Sample	Top Sample Uncert-ainty	Bottom Sample	Bottom Sample Uncert-ainty	Top Sample	Top Sample Uncert-ainty	Bottom Sample	Bottom Sample Uncert-ainty
Test 1	0.159	84.9	±0.2	60.3	±0.2	85.2	±3.3	60.3	±2.2
	0.489	78.1	±0.2	61.8	±0.2	78.3	±3.0	61.8	±2.3
	1.421	71.9	±0.2	63.1	±0.2	68.3	±2.7	63.0	±2.3
	2.244	70.1	±0.2	63.4	±0.2	70.3	±2.7	63.4	±2.3
	3.221	68.8	±0.1	63.6	±0.2	69.0	±2.6	63.5	±2.3
	4.014	68.1	±0.1	63.6	±0.2	68.3	±2.6	63.5	±2.3
Test 2	0.159	85.3	±0.2	59.9	±0.2	85.8	±3.5	59.7	±2.4
	0.489	79.0	±0.2	61.7	±0.2	79.4	±3.3	61.6	±2.4
	1.421	72.2	±0.3	63.3	±0.3	72.5	±3.0	63.2	±2.4
	2.244	70.0	±0.2	63.6	±0.2	70.3	±2.8	63.5	±2.4
	3.221	68.6	±0.2	63.7	±0.2	68.9	±2.7	63.6	±2.4
	4.014	67.8	±0.2	63.8	±0.2	68.1	±2.7	63.6	±2.4
Test 3	0.489	77.2	±0.2	60.0	±0.2	77.4	±3.0	59.9	±2.2
	1.421	72.5	±0.2	61.6	±0.2	72.7	±2.8	61.6	±2.3
	2.244	71.0	±0.2	62.4	±0.2	71.2	±2.8	62.3	±2.3
	3.221	69.8	±0.1	62.6	±0.1	70.0	±2.7	62.6	±2.3
	4.014	69.1	±0.2	62.8	±0.2	69.4	±2.7	62.8	±2.3
Test 5	0.221	90.8	±0.2	58.8	±0.2	91.1	±3.6	58.6	±2.3
	0.489	82.7	±0.2	61.3	±0.2	83.1	±3.3	61.1	±2.4
	1.421	74.3	±0.2	62.8	±0.2	74.6	±3.0	62.7	±2.4
	2.244	71.7	±0.2	63.3	±0.2	72.1	±2.9	63.1	±2.4
	3.221	70.0	±0.2	63.4	±0.1	70.3	±2.8	63.3	±2.4
	4.014	69.2	±0.1	63.5	±0.2	69.5	±2.6	63.4	±2.4
Test 6	0.159	89.4	±0.2	57.1	±0.1	89.6	±3.3	56.9	±2.3
	0.489	81.4	±0.2	59.3	±0.2	81.5	±3.0	59.1	±2.3
	1.421	73.9	±0.2	61.9	±0.1	74.0	±2.7	61.7	±2.5
	2.244	71.6	±0.2	62.5	±0.2	71.7	±2.6	62.3	±2.5
	3.221	69.5	±0.1	62.8	±0.2	69.5	±2.6	62.7	±2.5

Table 12 Estimated surface temperatures for the high-vacuum tests and test article swap tests.

		IHT Estimated Surface Temperature (°C)				Extrapolated Estimated Surface Temperature (°C)			
Test Run	Pressure (MPa)	Top Sample	Top Sample Uncert-ainty	Bottom Sample	Bottom Sample Uncert-ainty	Top Sample	Top Sample Uncert-ainty	Bottom Sample	Bottom Sample Uncert-ainty
High Vac S3S4 Retest	0.489	79.1	±0.2	62.5	±0.1	79.5	±3.4	62.5	±2.3
	1.421	71.3	±0.2	64.5	±0.2	71.8	±3.1	64.5	±2.4
	3.221	69.2	±0.2	64.9	±0.1	69.7	±3.0	64.8	±2.4
S2S1	0.489	77.6	±0.2	59.7	±0.1	77.8	±2.9	59.8	±2.2
	1.421	69.8	±0.1	62.1	±0.1	70.1	±2.6	62.2	±2.3
	3.221	68.6	±0.2	63.0	±0.2	68.8	±2.5	63.1	±2.3
S4S3	0.489	78.6	±0.2	61.9	±0.1	78.9	±3.0	61.4	±2.5
	1.421	71.1	±0.2	64.0	±0.1	71.4	±2.7	63.5	±2.5
	3.221	69.2	±0.2	64.3	±0.1	69.4	±2.6	63.9	±2.5
High Vac S3S4 Retest	0.489	84.7	±0.2	63.1	±0.2	84.7	±3.1	63.0	±2.3
	1.421	74.7	±0.2	65.5	±0.1	74.7	±2.7	63.0	±2.4
	3.221	72.0	±0.2	65.8	±0.1	72.0	±2.7	63.0	±2.4
S2S1 Retest	0.489	80.0	±0.2	61.5	±0.1	80.1	±2.9	61.3	±2.3
	1.421	71.3	±0.2	63.7	±0.1	71.5	±2.6	63.6	±2.4
	3.221	69.0	±0.2	64.0	±0.1	69.1	±2.5	63.8	±2.4

Since the actual surface contact areas affect the thermal resistance, it is apparent that the contact asperities are being altered and the contact areas increased as the compressive force increased. This leads to a decrease in the temperature difference between the interface surfaces. When the average was taken for the top test article at an interface pressure of 2.244 MPa, the surface temperature was 69.9°C when estimated using the IHT code and 70.1°C when the surface temperature was extrapolated; this results in only a 0.3% difference (Table 13) between the two methods. A major difference is found when the uncertainty is considered. For all of the interface temperatures determined via the IHT code, the uncertainty was <1°C, whereas the extrapolated surface temperatures had an uncertainty >2°C. Even though the results for both methods have estimated interface temperatures that can be considered acceptable, the uncertainty values were very different.

Tests when the test article location was changed were included to verify that none of the four test articles had significantly different thermophysical properties. Since the results for the estimated surface temperatures of the extra tests are within range of the larger mid-vacuum test group, it is assumed that there is no major deviation between the test articles. This can be seen when the average estimated surface temperatures for test article 1 and 2 when the applied pressure was 2.244 MPa are compared in Table 14, the percent difference is only 0.3%.

Table 13 Interface surface temperature averages and average uncertainty for interface pressure of 2.244 MPa at mid-vacuum.

	IHT Estimated (°C)	Extrapolated (°C)	Percent Difference
Top Sample Average	69.9	70.1	0.3%
Average Uncertainty	0.2	2.7	-
Bottom Sample Average	63.3	63.2	0.2%
Average Uncertainty	0.2	2.4	-

Table 14 IHT estimated surface temperature averages, average uncertainty, and average heat flux for tests where the test article location was changed from S1S2 to S2S1 at mid-vacuum for 2.244 MPa.

	IHT Estimated Mid-Vacuum (S1S2)	IHT Estimated Sample Location Change (S2S1)
Top Sample Average (°C)	69.0	70.6
Average Uncertainty	0.2	0.2
Bottom Sample Average (°C)	63.5	62.9
Average Uncertainty	0.2	0.2
Average Heat Flux (W/m^2)	10787.6	10087.0

When considering the high-vacuum estimated surface temperatures found with IHT, it is revealed that the percent difference between the high-vacuum and mid-vacuum results for both the top and bottom test articles is greater than 1% (Table 15). The results presented in Table 15

include the average results for all of test article 3 and 4 mid-vacuum tests when the compression pressure is 2.244 MPa. Two high vacuum tests were run with test articles 3 and 4; the interface surface temperatures and in-sample heat flux were averaged and are also found in Table 15. The high vacuum tests resulted in higher interface surface temperatures due to the increase in heat flux in the system. The percent difference between the heat flux in-sample average for each vacuum level is 5.6%. Since two tests were conducted at high vacuum and the larger results could be due to the small sample set used to calculate the averages. By conducting more tests at high vacuum, the statistical strength of the results would provide more reliable results that could be compared to the mid-vacuum test group.

Table 15 IHT estimated surface temperature averages, average uncertainty, and average heat flux for tests using test article configuration using S3S4, conducted at high and mid-vacuum for 2.244 MPa.

	IHT Estimated Mid-Vacuum (S3S4)	High Vacuum Tests (S3S4)	Percent Difference
Top Sample Average (˚C)	70.9	73.0	2.9
Average Uncertainty	0.2	0.2	-
Bottom Sample Average (˚C)	63.0	65.0	3.1
Average Uncertainty	0.2	0.2	-
Average Heat Flux (W/m^2)	10302.4	10890.7	5.6

To verify that the estimated surface temperatures for each test step resulted in values that fell in between the embedded TCs, the interface surface temperature and collected TC data was graphed together; Fig. 21 is the temperature data for Test 6 S1S2 Step 3. These values can be associated to the embedded TC found in Fig. 22. A visual verification can be made by identifying the location of the results recorded by the associated TC embedded in each sample and that the found surface temperatures are located in between the four sets of TC data. This was done for

each test step to verify if the code was written so that the interface surface temperature would be calculated correctly.

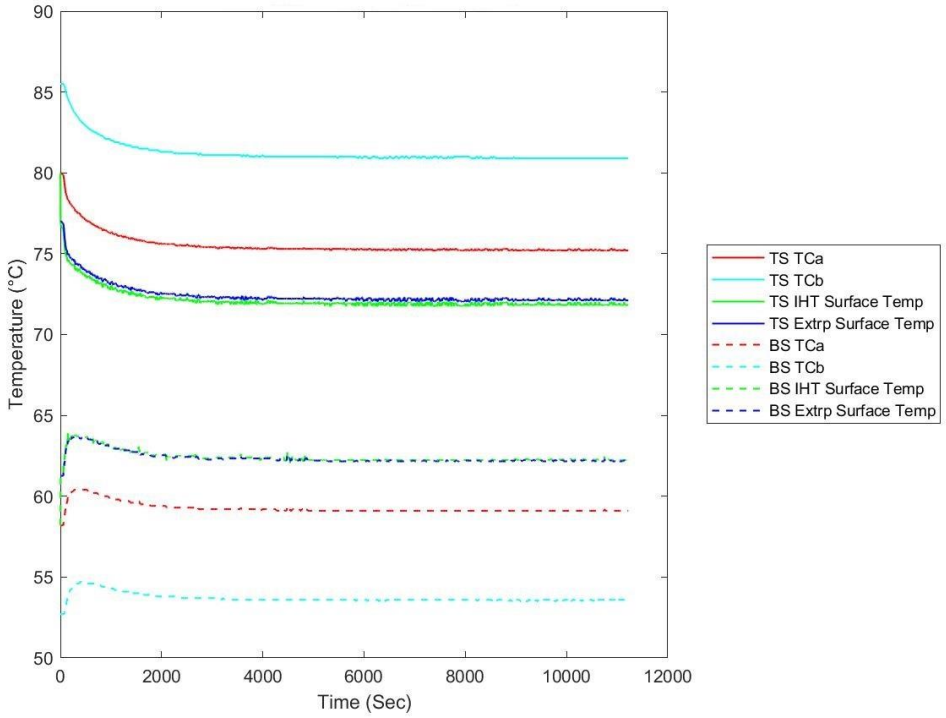

Fig. 21 Estimated interface surface temperatures for both samples (TS is Top Sample, BS is Bottom Sample) for Step 3 in Test 6 for test articles 1 and 2.

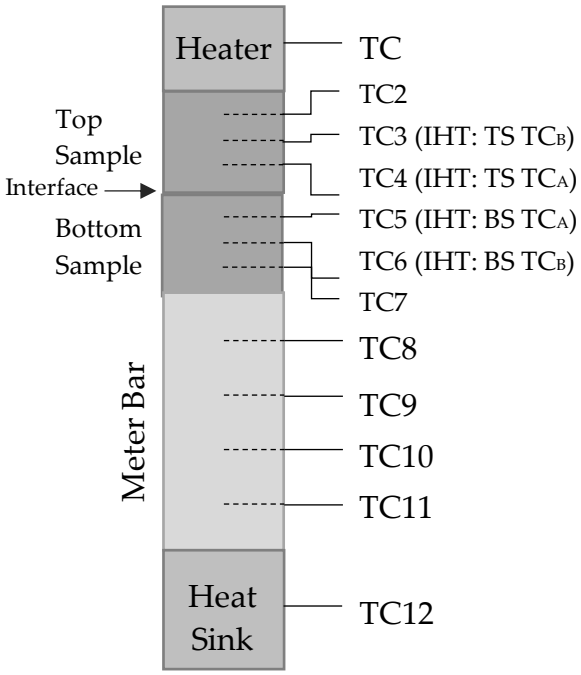

Fig. 22 Sample column with TC numbers used for experimental tests and TC labels for IHT calculations.

Heat flux in the sample column is calculated three different ways. The first is from the indirect section of the IHT code estimating the heat flux at the interface surface. The other two use Fourier's Law and data collected from the embedded TC: one uses the Meter Bar, and the second uses the temperature data collected from the TC embedded in the test articles. The results from these three methods should be similar.

The IHT heat flux was compared to the calculated in-test article and Meter Bar heat flux to see if there was any indication of thermal energy loss due to radiation in the sample column. Table 16 contains a comparison of the heat flux calculated by the three methods. The heat flux values indicate some thermal energy loss to the surroundings; another point of interest could be the interface between the bottom test article and the Meter Bar since this is another interface and will impede heat flow. As stated earlier, this interface is coated with vacuum grease to increase the conduction, but there still could be a change at this interface since there is a material change. The chosen vacuum grease may not be the best choice to assist in reducing the resistance at this

point, but is better than nothing and will need consideration in future testing. Just like the test article material, a mathematical expression was identified for the thermal conductivity of the Meter Bar material, Invar, based on Touloukian data [30]. Since the Meter Bar thermal conductivity was not initially measured by a certified material properties lab, there is the possibility that the exact material properties may differ, resulting in a different calculated heat flux.

Table 16 Heat flux in sample column calculated three different ways for test articles 1 and 2.

Test Number	Interface Pressure (MPa)	In-Sample Heat Flux (W/m^2)			IHT Interface Surface Heat Flux (W/m^2)			Meter Bar Heat Flux (W/m^2)
		Top Sample	Bottom Sample	Average	Top Sample	Bottom Sample	Average	
6	0.159	9716.8	9482.2	9599.5	9779.2	9554.5	9666.8	8480.7
	0.489	10017.7	9470.7	9744.2	10091.9	9542.8	9817.3	8694.9
	1.421	10227.6	9480.8	9854.2	10300.5	9552.8	9926.6	9023.5
	2.244	10243.6	9481.3	9862.4	10316.8	9554.7	9935.7	9108.1
	3.221	10260.6	9474.1	9867.3	10335.0	9545.9	9940.5	9209.0
	4.014	10251.8	9475.2	9863.5	10325.5	9547.0	9936.3	9258.2

To verify the assumption that the radiation loss was negligible, the radiation loss was calculated for the external surface area of the test articles. Since Test 5 for Samples 3 and 4 had the highest average recorded temperatures (Appendix, Section F) from the two embedded TCs that were used for the IHT calculations, this test was used to calculate the radiation heat loss at each compressive force. Table 17 contains the radiation loss as a percentage of the in-test article heat rate. There are only five compressive loads steps since Test 6 was forced to end early. These results show that the loss due to radiation is less than 3% of the total internal heat rate. This is not a substantial amount of loss, but it could be enough to account for the inconsistences within the data.

Table 17 Radiation loss from test articles to chamber as a percentage of the in-test article heat rate.

	Percent of Total				
	Step 1	Step 2	Step 3	Step 4	Step 5
Sample 3 loss to chamber	2.8	2.3	1.9	1.8	1.7
Sample 4 loss to chamber	1.0	1.0	1.0	1.0	1.1

6 UNCERTAINTY ANALYSIS

All experiments that require the collection of values to be used in calculations have two types of uncertainty: systematic (bias) and random (precision) [23,32]. Since the two methods for estimating surface temperature are being compared, the uncertainty associated with both are crucial for this work. The uncertainty in the TCR values can be used to gauge which method will have the least uncertainty and provide a more reliable TCR value. Total uncertainty is defined by Eq. (19) and includes both systematic and random uncertainty:

$$U_{total} = \sqrt{(U_B)^2 + (U_R)^2} \quad (19)$$

where U_B is the systematic uncertainty and U_R is the random uncertainty. These uncertainties are found by identifying the uncertainty for each measured value and then propagating them through the heat flux and TCR equations by using the standard equation for uncertainty propagation for multivariable functions (Eq. (20)):

$$Uf = \sqrt{\left(\frac{\partial f}{\partial x}Ux\right)^2 + \cdots + \left(\frac{\partial f}{\partial z}Uz\right)^2} \quad (20)$$

When Eq. (20) is applied to Eqs. (1) and (2), the uncertainty for TCR, Eq. (21), and heat flux, Eq. (22), can be identified:

$$U_{R''} = \sqrt{\left(\frac{\partial R''}{\partial q''}U_{q''}\right)^2 + \left(\frac{\partial R''}{\partial T_A}U_{T_A}\right)^2 + \left(\frac{\partial R''}{\partial T_B}U_{T_B}\right)^2} \quad (21)$$

$$U_{q''} = \sqrt{\left(\frac{\partial q''}{\partial \Delta x}U_{\Delta x}\right)^2 + \left(\frac{\partial q''}{\partial k}U_k\right)^2 + \left(\frac{\partial q''}{\partial T_1}U_{T_1}\right)^2 + \left(\frac{\partial q''}{\partial T_2}U_{T_2}\right)^2} \quad (22)$$

where $U_{q''}$, U_{TA}, U_{TB}, $U_{\Delta x}$, U_k, U_{T1}, and U_{T2} are the uncertainty estimates for the heat flux, interface surface temperatures, distance between TC locations, thermal conductivity in the test article material, and the data collected by the two TCs that were used to calculate the heat flux. These

equations can be used independently to find first the random uncertainty and then the systematic uncertainty.

The propagation of uncertainty for Eqs. (1) and (2) is easy to find as long as the uncertainty of the TCs, the heat flux, and the distance between the TC locations are known. Many of the values were averaged from repeated measurements resulting in the ability to identify a confidence interval that can be used for uncertainty. For all averaged values a confidence interval of 95% was used for the random uncertainty; by identifying the confidence interval a range can be established where the true value will be present [32]. This process involved calculating the standard deviation of the data set and using the associated t-distribution value for the appropriate degrees of freedom. The random uncertainty component is then found by

$$P_e = t\, S_e \qquad (23)$$

where P_e is the random uncertainty, t is the t-distribution value associated with the correct degrees of freedom and desired confidence interval, and S_e is the standard deviation of the data set. By using the associated number of degrees of freedom for the values of interest, the t-value can be found within any statistical table [32]. Since the test article set for the temperature data was the last five minutes of test data, the test article size was 300 data points corresponding to a t-value of 1.960. The t-value that was used for the locations of the TC holes was found to be 2.228.

The uncertainty associated with the extrapolated surface temperature was found by using the equation for the uncertainty of a value calculated with the generated least-square line. Taylor presents an analysis of the least-squares fitting line for experimental data which includes calculating error for the components of the fitted line along with error in an extrapolated data point [23]. The equations used to estimate the surface temperatures with the least-square fit line can be found in Section 3.1, Eq. (4). For an uncertainty value to be determined for y, in this case the extrapolated surface temperature, it is assumed that the results for y are normally distributed about the true value defined by the least-square line equation, $y = D + Bx$. The result is that the sum of squares can be used for the error with a modification to the number of collected data

points due to the fact that D and B are the best estimate values based on Eqs. (5) and (6). The result is the standard deviation which can be used to find the random uncertainty [32]:

$$\sigma_y = \sqrt{\frac{1}{N-2}\sum_{i=1}^{N}(y_i - D - Bx_i)^2} \quad (24)$$

The systematic uncertainty for the TCs is reported by Omega, the manufacturer. According to Omega, the TCs contain a systematic error of 0.75% of the reading or ±1°C (whichever is larger) [33]. For this case, the ±1°C was found to be larger and therefore was used. The systematic error for the TC location measurement was taken from calibration documentation for the caliper used for these measurements.; this value was found to be $\pm 5.08\times10^{-5}$ m. The systematic uncertainty for the material properties was presented at 10% in the Touloukian documentation [30]. Unfortunately, the random uncertainty for the material properties is unknown and would require multiple measurements at different temperatures for it to be calculated.

The systematic uncertainty calculated in Section 4 were used for the estimated surface (see Section 4 for more details). The percent difference between the measured surface temperatures and the temperature found through both methods were obtained from the verification test where the heater power supply was set to 6V. The results from this test were chosen because the verification surface temperature is comparable to the estimated interface surface temperatures found using IHT and extrapolation. The percent differences were then used for the associated bias error for interface surface temperatures estimated with both methods.

The uncertainty values for each test were calculated for the individual test parameters before being propagated through the heat flux or TCR equations. This allowed for the evaluation of each test and allowed for comparison between individual test results. The individual uncertainties for some of the measurements can be found in Table 18. Individual uncertainty values for the interface temperatures, along with the calculated temperatures, are presented in the results for the data collection section of this document, Section 5.3.

TCR utilizes simple equations but the change in temperature between the interface surfaces is crucial. The work presented here for the uncertainty was completed so that the two methods of estimating the interface surface temperatures could be used to evaluate the individual methods and produce TCR values that have a reliable associated uncertainty.

Table 18 Bias and Random Uncertainty for measured values.

Variable	Bias	Random
SS 304 Thermal Conductivity	10%	-
Measured distances	0.0000508m	0.00039m [a]
TC Data	1°C	0.15°C [a]
IHT Surface temperature	0.21%	0.25°C [a]
Extrapolated Surface Temperature	3.68%	1.5°C [b]

a. Found from standard deviation with 95% confidence interval, maximum uncertainty value for all tests

b. Found by using Least-Square Line Standard Deviation with 95% confidence interval, maximum uncertainty value for all tests

7 CALCULATING THERMAL CONTACT RESISTANCE VALUES WITH BOTH METHODS

The process for calculating TCR values with associated uncertainties for each compressive force are as follows: (1) collect data; (2) for the full duration of each test point, determine interface surface temperature estimates using both methods and calculate heat flux in the sample column; (3) average each interface surface temperature and heat flux over the last five minutes of data for each test so that TCR can be calculated; and (4) average the calculated TCR value found for each test at each compressive force so that a final resistance can be presented for each compressive force. Throughout this process the associated systematic and random uncertainty were determined and then allowed to propagate through any calculations that were made.

All mid-vacuum tests will be presented together as a group, the tests where the test article location was switched and where the chamber was brought to high vacuum will be considered in two separate groups so that comparison can be made between all three. The TCR values for each test can be found in a tabulated form in the Appendix, Section G. The results for all mid-vacuum tests were used to find a TCR average for both methods of estimating the interface surface temperatures. Fig. 23 contains the average TCR values for both methods, and both sample sets, at each compressive force step along with the associated error bars; Table 19 contains the numerical values. Since the resulting values are so close, the percent difference between the IHT TCR results and the extrapolated TCR results have been presented in Table 20. The uncertainty of the TCR results using the extrapolated surface temperatures increased as the compressive force increased, whereas the results found using the IHT interface surface temperatures stayed relativity the same, about ±25% of the result. The results for the steps with the lower compressive force resulted in high absolute uncertainty values for the IHT TCR values.

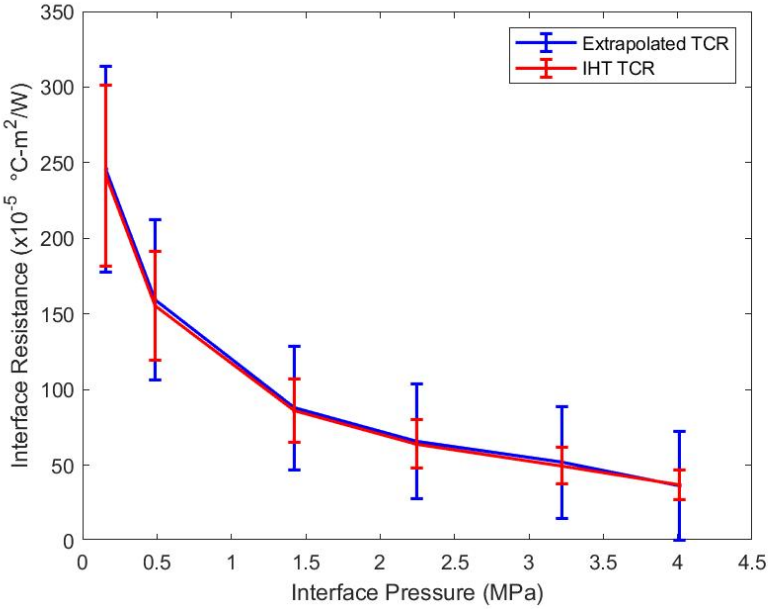

Fig. 23 Averages for TCR values for the mid-vacuum tests with surface temperatures estimated with both methods.

Table 19 Overall TCR average values with uncertainty for all mid-vacuum tests.

Step Number	Interface Pressure (MPa)	Found with IHT Estimated Surface Temperatures (x10^{-5} °C-m^2/W)			Found with Extrapolated Surface Temperatures (x10^{-5} °C-m^2/W)		
		TCR Average	Uncertainty Average	Percent Uncertainty	TCR Average	Uncertainty Average	Percent Uncertainty
1	0.159	241.5	±60	25%	245.8	±68	28%
2	0.489	155.1	±36	23%	159.1	±53	33%
3	1.421	85.8	±21	24%	87.7	±41	47%
4	2.244	64.0	±16	24%	65.6	±38	58%
5	3.221	49.6	±12	24%	51.8	±37	72%
6	4.014	41.9	±10	24%	42.5	±36	84%

Table 20 Percent difference between IHT TCR values and Extrapolated TCR values.

Step Number	Interface Pressure (MPa)	Percent Difference
1	0.159	-1.8%
2	0.489	-2.5%
3	1.421	-2.2%
4	2.244	-2.5%
5	3.221	-4.4%
6	4.014	1.4%

The uncertainty of the individual components for TCR showed that the systematic uncertainty for the average heat flux in the test articles has the greatest difference between its values based on compressive force; when the compressive force is the lowest, the uncertainty for the heat flux is the highest. This propagates through and causes the uncertainty for TCR to be larger at the lower compressive forces.

A focused study of the uncertainty for each variable found that the uncertainty for the heat flux was the largest contributor to the TCR uncertainty value (Table 21). This study looked at the uncertainty contribution for each variable found in the TCR equation (Eq. 1); this short study used the results for Test 2 S1S2 Step 4. Considering the heat flux uncertainty, the systematic uncertainty is the larger of the two uncertainty components, with the systematic uncertainty for the embedded TC temperature measurements, ±1˚C, contributing the most to the propagated heat flux uncertainty. This was followed closely by the 10% uncertainty found in the Touloukian thermal conductivity of SS 304. The total uncertainty, along with both the random and systematic uncertainties for each test, are in the Appendix, Section G.

All of the TCR final values were calculated using an average of the in-sample heat flux for both test articles. The nodal convergence compared the difference between the in-test article heat flux and the heat flux at the interface surface. The in-sample calculation utilizing Fourier's Law, which allows for the uncertainty to propagate through the equation.

Table 21Values used to calculate TCR results for Test2 S1S2 Step 4 (2.244 MPa).

Variable	Empirical Value	Random Uncertainty	Systematic Uncertainty	Total Uncertainty	Percent of Total
Top Sample TC1 (°C)	78.5	±0.1	±1	±1.0	1.3%
Top Sample TC2 (°C)	72.0	±0.1	±1	±1.0	1.4%
Bottom Sample TC1 (°C)	59.5	±0.0	±1	±1.0	1.7%
Bottom Sample TC2 (°C)	53.6	±0.1	±1	±1.0	1.9%
Top Sample IHT Surface Temperature Estimate (°C)	68.2	±0.1	±0.1	±0.2	0.3%
Bottom IHT Surface Temperature Estimate (°C)	62.8	±0.2	±0.1	±0.2	0.3%
Top Sample Extrapolated Surface Temperature Estimate (°C)	68.3	±0.6	±2.5	±2.6	3.8%
Bottom Sample Extrapolated Surface Temperature Estimate (°C)	62.6	±0.6	±2.3	±2.4	3.8%
Average Sample Heat Flux (W/m^2)	10868.4	±472.1	±2673.2	±2715	25.0%
TCR Value IHT ($x10^{-5}$ °C-m^2/W)	**68.9**	**±5.0**	**±17.2**	**±17.9**	**25.9%**
TCR Value Extrapolated ($x10^{-5}$ °C-m^2/W)	**52.5**	**±7.9**	**±33.9**	**±34.8**	**66.4%**

Since the high-vacuum tests and test article switch tests were added to evaluate the results from a different vacuum level and assure consistent material properties of the test articles, they were compared to the mid-vacuum tests. Figure 24 contains results from one of the high-vacuum tests, one of the tests where the test article location was switched, and one mid-vacuum test; all results were found by using interface surface temperatures estimated with IHT code. The three tests presented in Fig. 24 were chosen randomly for this comparison. Focusing on the results for the second, fourth, and sixth test steps, the extra test results can be compared to the mid-vacuum results. At each of these compressive force levels there really is no change in the TCR results between the three tests.

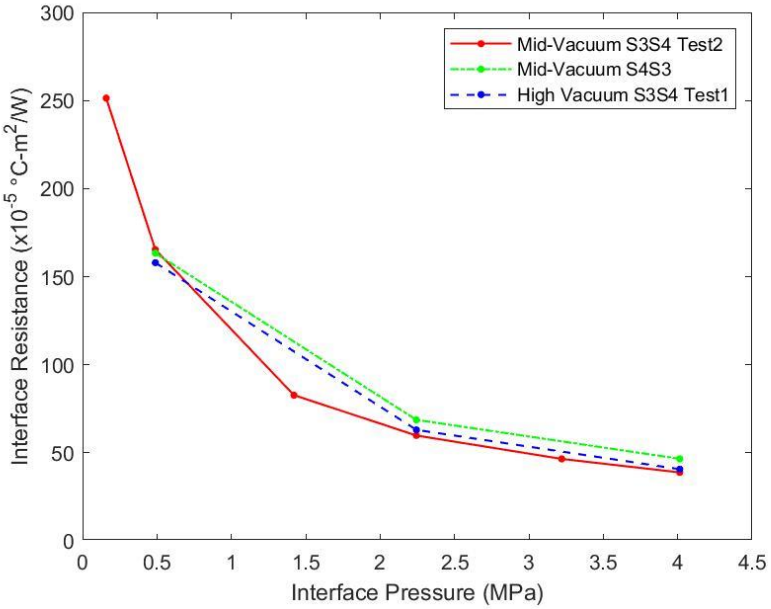

Fig. 24 TCR Results for one mid-vacuum test, test article location change test, and one high-vacuum test for IHT estimated surface temperatures.

The original goal for the tests was to attempt to duplicate the test setup used by McWaid [2] and then compare the results; the results from this study were first graphed along with McWaid's results and can be seen in Fig. 25. The McWaid test results found using ground interface surfaces falls within the error bars for the IHT TCR values for all applied pressures. At the higher pressures, the fine bead blasted sample set is just within the error bars. The interface surfaces for this test were prepared using bead blast that was comparable to the fine bead blast used by McWaid; unfortunately, the last point of data reported by McWaid was excluded since the pressure was out of the range that could be provided by that air cylinder. The trend in both McWaid's study and this study suggested that that final data point could have fallen with the error bars for this study, indicating that the results from this study are comparable to that of McWaid's at higher interface pressures.

Interestingly, the average surface roughness for McWaid's data (found in Table 22) does not seem to trend with his TCR values when looking at all data sets; it is expected that a higher RMS value yields a higher TCR result. The bead blasted samples follow this expected outcome

only in the upper interface pressure range. McWaid explains the measurement of the RMS value for the ground samples in detail since it involved multi-directional passes concluded by calculating an overall average [2]. His outcome is that the sample set with the lower RMS yields TCR values that are lower than that of the set with the higher RMS value. This is expected intuitively and empirically. But when the ground samples are compared to the bead blasted samples the ground samples are found to have lower resistance values for each interface pressure; a result that is not expected based on the method of surface finish.

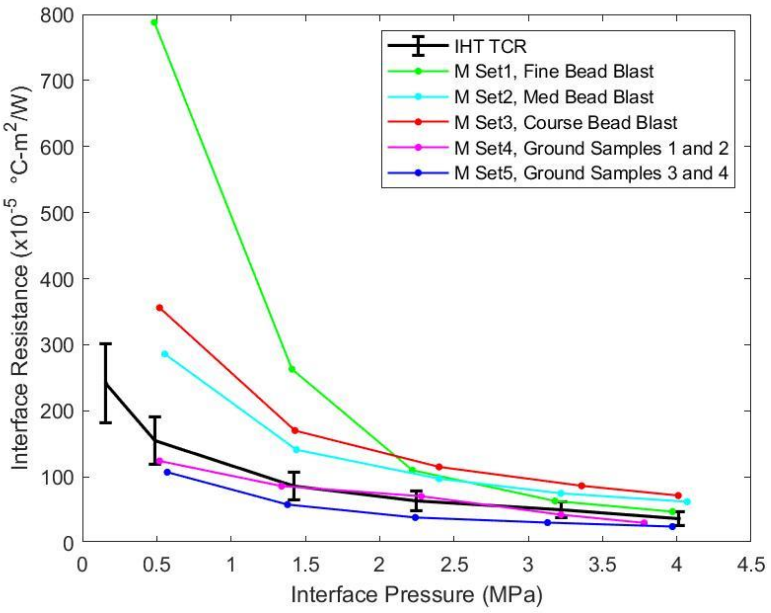

Fig. 25 IHT Resistance Results along with McWaid's Results.

Related to that last comment, an interesting observation of McWaid's data is that the method of preparation in relation to the RMS value can produce different results. M Set5 and M Set1 have RMS values of 0.83 and 0.84 μm (Table 22), respectively, but have TCR results that are notably different. The RMS values for these samples are comparable to the test samples used for this study, 0.80 μm (full results for surface roughness are in the Appendix, Section E). Even though all resulting TCR data sets fall in the shape of an inverse exponential curve, the M Set1

curve encompasses a much greater range of TCR values. At the lower interface pressures, the M Set1 resulted in high TCR values when compared to the results from this study. The M Set5 had lower TCR values compared to the results of this study and exhibited a flatter curve over a narrower range of TCR values. McWaid's outcome can be resolved by assuming that the microscopic asperities that existed in the M Set5 samples could be interlocking when placed under pressure, increasing contact surface area and decreasing contact resistance.

Table 22 Surface finish method and RMS values for each of McWaid's test sample sets[2].

Study Label	McWaid Label	Finishing Method	RMS (μm)
M Set1	SF1/SF2	Small (Fine) Bead Blast	0.84
M Set2	SM1/SM2	Medium Bead Blast	1.38
M Set3	SC1/SC2	Course Bead Blast	1.47
M Set4	SG1/SG2	Ground, Mounted with Lays Parallel	1.001
M Set5	SG3/SG4	Ground, Mounted with Lays Perpendicular	0.83

Finally, the average TCR values calculated using the extrapolated surface temperatures were compared to other results presented in literature. The literature results are in studies conducted by Hegazy [9], Milanez et al. [12], McWaid [2], Fried [11], and Clausing and Chao [13]. Each of the published data sets were found by extrapolating the interface surface temperatures. Table 23 contains details about the literature results, including surface roughness and finish methods for each. The average TCR results using the extrapolated surface temperatures trend in the middle of the results found in published literature with the published results for the higher compressive forces falling within the error bars associated to this study (Fig. 26). When the test articles that were used for this study were measured for surface roughness, the pre-test average was 0.80 μm RMS. The results from Milanez et al. [12] were reported to have a RMS value of 0.72 μm; this RMS value was the closest to the 0.80 μm measured from the test articles used in this study. The Milanez et al. test article set consisted of one test article that was bead blasted and one that was reported as lapped but were only tested with interface pressures values lower than 3 MPa.

The results obtained from Fried [11], trend well with the current results and fall within the error bars. Fried's results were collected from test articles that were ground and had RMS values ranging from 0.38 to 0.25 μm. Interestingly, the TCR average for this study falls in-between the results by Hegazy [9], where his RMS measured 0.478 μm for one set and 2.71 μm for the second, where both test article sets were bead blasted and lapped. It should be noted that Hegazy's second set (H Set2) and Clausing and Chao's second set (CC Set2) have similar results in the higher compressive force range and yet have RMS values of 2.71 μm and 0.08 μm, respectively. This only shows the unpredictability of TCR results.

When the interface pressure is greater than 2 MPa, the published results fall within the error bars that are associated to the results for this study. At interface pressures less than 2 MPa, the published results fall outside of the error bars. The spread for the published data is greater at the lower interface pressures so the expectation of finding the published results within the error for this study is low; this would only result from excessively high uncertainty, which is undesirable. Even though the published data does not fall entirely within the error over all interface pressures, it appears that the results from this study are comparable to results produced by other researchers. This is because the results found here follow a trend that is comparable to published literature when the interface pressure is low, then if the interface pressure is high, the literature results fall within the error for this study.

In Fig. 27 the extrapolated TCR values have been replaced with the TCR values found using surface temperatures calculated with the IHT method. The only outcome of this is that the error bars are reduced and the IHT TCR values, along with the error, fall within the main group of the published literature.

Table 23 Details for Literature Collected TCR Results.

Author	Author's Label	Current Label	Surface finish method	RMS (μm)
Hegazy	PSS0102	H Set1	Bead Blasted/Lapped	0.478
	PSS0304	H Set2	Bead Blasted/Lapped	2.71
McWaid	SM1/SM2	M Set2	Medium Bead Blast	1.38
	SG1/SG2	M Set4	Ground Mounted with Lays Parallel	1.001
Fried	Samples 1&2	F Set1	Ground, Clean	0.38-0.25
Milanez, Yovanovich, and Mantelli	S1	MYM Set1	Bead Blasted/Lapped	0.72
Clausing and Chao	1_S	CC Set1	Lapped	0.08
	2_S	CC Set2	Lapped	0.08

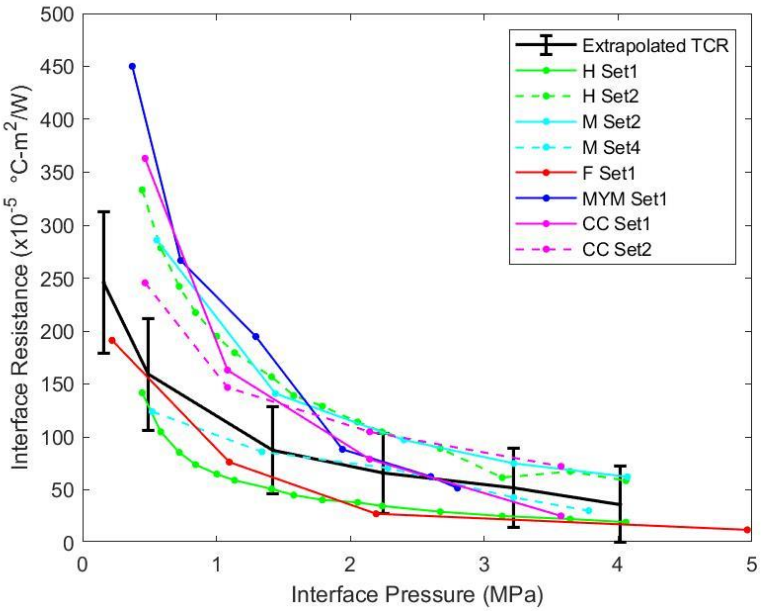

Fig. 26 Literature results with Averages for the TCR values when the surface temperatures are estimated with the extrapolated method for interface surface estimations.

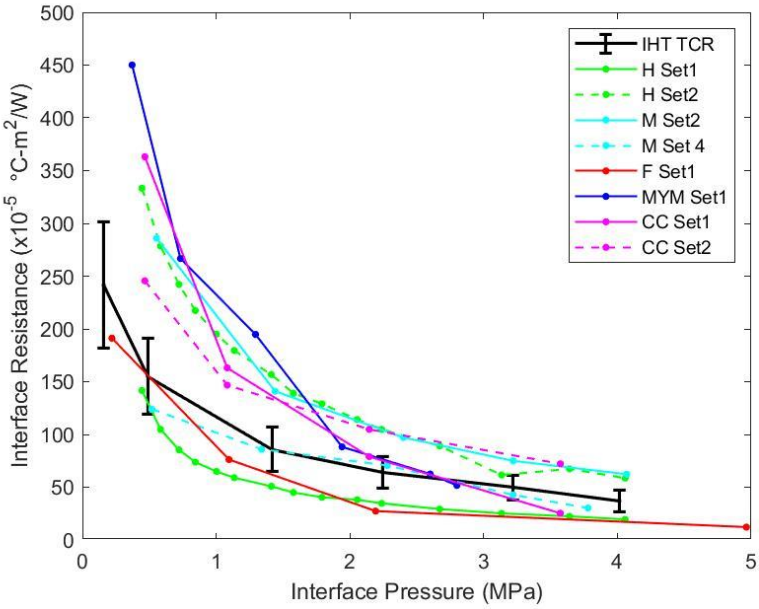

Fig. 27 Literature results with Averages for the TCR values when the surface temperatures are estimated with the IHT method for interface surface estimations.

8 CONCLUSIONS

The primary goal for this work was to obtain thermal contact resistance values with well-defined uncertainty. Two methods of estimating the interface surface temperatures were used and the resulting uncertainties were compared to determine which method is the most reliable. The common practice method involves extrapolating the surface temperature using temperature data from TCs that have been embedded within the test articles. The second method utilizes the same TC data along with Inverse Heat Transfer methodology to estimate the surface temperatures.

The uncertainty calculations were divided into both systematic and random uncertainty. The majority of the data used in calculation of TCR had 95% confidence intervals for the random uncertainty associated with the measured value. The extrapolated interface surface temperatures used standard deviation equations associated with the least-square line along with the 95% confidence interval. The standard deviation equations were more applicable than applying a confidence interval to a standard deviation associated with finding the average value over the last 5 minutes of collected data. The uncertainty for the extrapolated surface temperatures were higher than those that were estimated using IHT.

When identifying the systematic uncertainty for the estimated temperatures, the analysis began with the code verification tests. First, the estimated surface temperatures found using both methods were compared to measured values while producing uncertainty values that could be used for calculating TCR uncertainty. The difference between the measured and estimated value was used as the systematic uncertainty estimate for the interface surface temperatures when propagating the uncertainty through the TCR calculations. Since three tests were conducted, the percent error for the verification test when the heater voltage was controlled at 6V was chosen because the resulting temperatures were comparable to the values observed in the TCR test results. Since the interface surface temperatures cannot be directly measured, there was no way to determine the bias between the IHT-estimated temperatures or the extrapolated values; therefore, using the difference found during the validation test is a reasonable assertion. Future work should refine this process by establishing a mathematical expression derived with a variety

of test points so that the uncertainty for the estimated surface temperature can be based on the estimated temperature value.

Since the initial goal for this study was to replicate the experimental tests performed by McWaid, the IHT TCR values were compared to all of McWaid's results. It was discovered that the results from this study trended well with McWaid's data for the higher interface pressures. The results from this study produced TCR values that were less than the McWaid TCR values, whose sample interface surface finishes were bead blasted.

Finally, the TCR was calculated using the interface temperature averages from the extrapolated mid-vacuum test results and were compared to other published data. The extrapolated results were used for the comparison since the published data was also found through extrapolation. The extrapolated results trended through the middle of the published results, with the published results falling within the error bars for the test points where the compressive force was the highest. Published results with lower test article compressive loads experienced a greater scatter compared with higher compressive force measurements. This greater spread in values causes the published data to fall outside of the error bars and indicates that the uncertainty values should be higher at lower compression forces, which was confirmed when the uncertainty analysis was concluded for both IHT and extrapolation. The conclusion is that the results for TCR found by extrapolating the surface temperatures are comparable to results that have been reported by other research. Since the IHT TCR values are so close to the extrapolated TCR values but have smaller error bars they were also graphed along with the published results so that the error bars could be compared to the published values. If the results for the validation tests are considered, then the uncertainties associated with TCR found through IHT result in quantities much lower than when the interface surface temperatures are extrapolated. With more refinement the IHT uncertainties could be reduced resulting in more reliable TCR values. The focus should be on reducing the systematic error for the interface surfaces along with considering a temperature measure that has a better systematic uncertainty.

The inclusion of an extensive uncertainty analysis not only provided a means to compare the two methods of surface temperature estimations but can help identify where improvements can be made to reduce the uncertainty. Additional test runs will provide more statistically sound

results, but the systematic uncertainty of the TCs that lead to high uncertainty values for the heat flux conditions require improvements. If the original TC data was used instead of the smoothed data, then the noise present in the system would have also caused the random uncertainty to be higher, as well. Reduction of the noise in the TC measurements will need improvement in future testing.

The introduction of IHT to estimate the surface temperature at the interface generates a more accurate value for TCR. Additionally, the IHT TCR results take material properties into account when estimating the interface surface temperature. Since the TCR code includes both methods of estimating the surface temperature at the interface, both methods can be compared after each future test. Once the TCR values are calculated, only a small amount of further work is required to establish the uncertainties. Future tests will require that the estimated surface temperature systematic uncertainty be identified prior to a full propagation. Even so, this will give thermal engineers two values for TCR to more accurately complete their thermal analysis work.

REFERENCES

[1] Madhusudana, C. V., and Fletcher, L. S. "Contact Heat Transfer - The Last Decade." *AIAA Journal*, Vol. 24, No. 3, 1986, pp. 510–523. doi:10.2514/3.9298.

[2] McWaid, T. H. *Thermal Contact Resistance Across Pressed Metal Contacts in a Vacuum Environment*. University of California, Santa Barbara, 1990.

[3] Yovanovich, M. M. Recent Developments in Thermal Contact, Gap and Joint Conductance Theories and Experiment. *Heat Transfer, Proceedings of the International Heat Transfer Conference*. Volume 1, 35–45.

[4] Merrill, C. T., and Garimella, S. V. "Measurement and Prediction of Thermal Contact Resistance across Coated Joints." *Experimental Heat Transfer*, Vol. 24, No. 2, 2011, pp. 179–200. doi:10.1080/08916152.2010.503311.

[5] Tomimura, T., Takahashi, Y., Do, T. W., Shigyo, K., and Koito, Y. "Simple Evaluation Method for Temperature Drop at Contact Interface between Rough Surfaces under Low Contact Pressure Conditions." *IOP Conference Series: Materials Science and Engineering*, Vol. 61, 2014. doi:10.1088/1757-899X/61/1/012040.

[6] Bahrami, M., Culham, J. R., and Yovanovich, M. M. "Modeling Thermal Contact Resistance: A Scale Analysis Approach." *Journal of Heat Transfer*, Vol. 126, No. 6, 2005, p. 896. doi:10.1115/1.1795238.

[7] Fuller, J. J., and Marotta, E. E. "Thermal Contact Conductance of Metal/Polymer Joints: An Analytical and Experimental Investigation." *Journal of Thermophysics and Heat Transfer*, Vol. 15, No. 2, 2001, pp. 228–238. doi:10.2514/2.6598.

[8] Snaith, B., O'Callaghan, P., and Probert, S. "Can Standards Be Set for Reliable Measurements of Thermal Contact Conductance." *21st Aerospace Sciences Meeting*, 1983. doi:10.2514/6.1983-533.

[9] Hegazy, A. A.-H. "Thermal Joint Conductance of Conforming Rough Surfaces: Effect of Surface Micro-Hardness Variation." *PhD Thesis, Uni. of Waterloo*, 1985.

[10] McWaid, T., and Marschall, E. "Thermal Contact Resistance Across Pressed Metal Contacts in a Vacuum Environment." *International Journal of Heat and Mass Transfer*, Vol. 35, No. 11, 1992, pp. 2911–2920. doi:10.1016/0017-9310(92)90311-F.

[11] Fried, E. *Study of Interface Thermal Contact Conductance*. Philadelphia, 1964.

[12] Milanez, F. H., Yovanovich, M. M., and Mantelli, M. B. H. "Thermal Contact Conductance at Low Contact Pressures." *Journal of Thermophysics and Heat Transfer*, Vol. 18, No. 1, 2008, pp. 37–44. doi:10.2514/1.2259.

[13] Clausing, A. M., and Chao, B. T. *Thermal Contact Resistance in a Vacuum Environment*. Urbana, 1963.

[14] Pizzo, M. E., Glass, D. E., and Bey, K. "Analysis of Internal Thermocouple Data in Carbon/Carbon Using Inverse Heat Conduction Methods." *54th AIAA Aerospace Sciences Meeting*, No. January, 2016, pp. 1–17. doi:10.2514/6.2016-0508.

[15] Carasso, A. S. "Space Marching Difference Schemes in the Nonlinear Inverse Heat Conduction Problem." *Inverse Problems*, Vol. 8, No. 25, 1992, pp. 25–43.

[16] Workman, D. L. *Setup, Calibration, and Verification of a Thermal Contact Conductance Measurement Apparatus*. George Washington University, 2004.

[17] Snaith, B., Probert, S. D., and O'Callaghan, P. W. "Thermal Resistances of Pressed Contacts." *Applied Energy*, Vol. 22, No. 1, 1986, pp. 31–84. doi:10.1016/0306-2619(86)90073-5.

[18] Madhusudana, C. V. *Thermal Contact Conductance*. Springer, New York, 2014.

[19] "E1225-13: Standard Test Method for Thermal Conductivity of Solids Using the Guarded-Comparative-Longitudinal Heat Flow Technique." *ASTM*, 2015, pp. 1–10. doi:10.1520/E1225-13.2.

[20] Touloukian, Y. S., and Ho, C. Y. *Thermophysical Properties of Selected Aerospace Materials; Part II: Thermophysical Properties of Seven Materials*. Purdue Research Foundation, West Lafayette, 1977.

[21] Rao, V. V., Bapurao, K., Nagaraju, J., and Murthy, M. V. K. "Instrumentation to Measure Thermal Contact Resistance." *Measurement Science and Technology*, Vol. 15, No. 1, 2004, pp. 275–278. doi:10.1088/0957-0233/15/1/040.

[22] Hills, R. G., and Hensel, Jr., E. C. "One-Dimensional Nonlinear Inverse Heat Conduction Techinque." *Numerical Heat Transfer*, Vol. 10, 1986, pp. 369–393.

[23] Taylor, J. R. *An Introduction To Error Analysis*. University Science Books, Sausalito, 1997.

[24] Murio, D. A., and Guo, L. "A Stable Space Marching Finite Differences Algorithm for the Inverse Heat Conduction Problem with No Initial Filtering Procedure." *Computers Math. Applic.*, Vol. 19, No. 10, 1990, pp. 35–50.

[25] Keirth, F., and Black, W. Z. *Basic Heat Transfer*. Harper & Row, Publishers, Inc., New York, 1980.

[26] "Temperature Measurements with Thermocouples : How-To Guide." *National Instrument*, 2011, pp. 1–6.

[27] Mathworks Smooth Noisy Data. https://www.mathworks.com/help/curvefit/smoothing-data.html.

[28] Minco. Minco Polyimide Thermofoil Heater. http://catalog.minco.com/catalog3/d/minco/?c=fsearch&cid=3_1-polyimide-thermofoil-heaters.

[29] Maddren, J., and Marschall, E. "Predicting Thermal Contact Resistance at Cryogenic Temperatures for Spacecraft Applications." *Journal of Spacecraft and Rockets*, Vol. 32, No. 3, 1995, pp. 469–474. doi:10.2514/3.26639.

[30] Purdue University. *Thermophysical Properties of Selcted Aerospace Materials*. West Lafayette, Ind., 1977.

[31] Killough, B. D. "NASA LaRC Thermal Testing Philosophy." *Thermal Test Panel Discussion presented at 14th Thermal/Fluids Analysis Workshop*, 2003.

[32] Coleman, H. W., and Steele, W. G. *Experimentation and Uncertainty Analysis for Engineers*. John Wiley & Sons, Inc., New York, 1999.

[33] Omega. Wire Color Codes and Limits of Error. https://www.omega.com/techref/colorcodes.html. Accessed Mar. 6, 2019.

APPENDICES

A. CHAMBER THROUGH PORT CONFIGURATION AND SYSTEM IMAGES

The following images are of the test chamber and the location of the through ports that were used for this study. In Fig. 28, the coolant bath is located in the lower left-hand corner; the blue line connected to the back can be followed up to the through port. The heater power supply is seen off to the left in the background. The monitor that is found in the image is connected to the chamber control computer and its setup to display TC and load cell data as it is being collected.

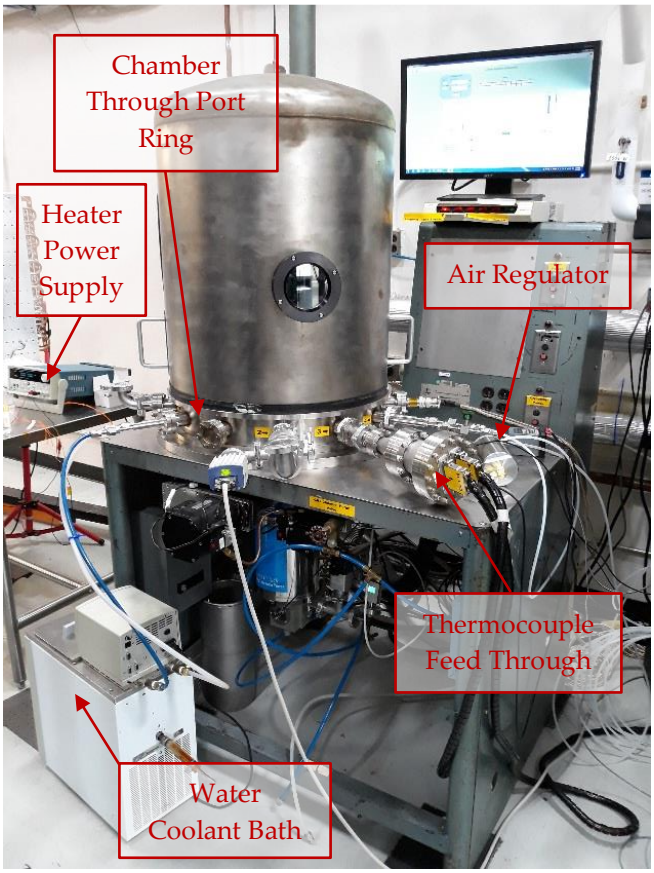

Fig. 28 Stainless Steel Bell Jar during testing.

Fig. 29 shows that through port number 4 was setup to allow penetration for the air line to the air cylinder. As seen in the image only the extract line is connected to the air regulator after

it passes through the external volume. The retract line was closed off with a valve and during testing the weight of the moveable platen and the test column was used to retract the air cylinder.

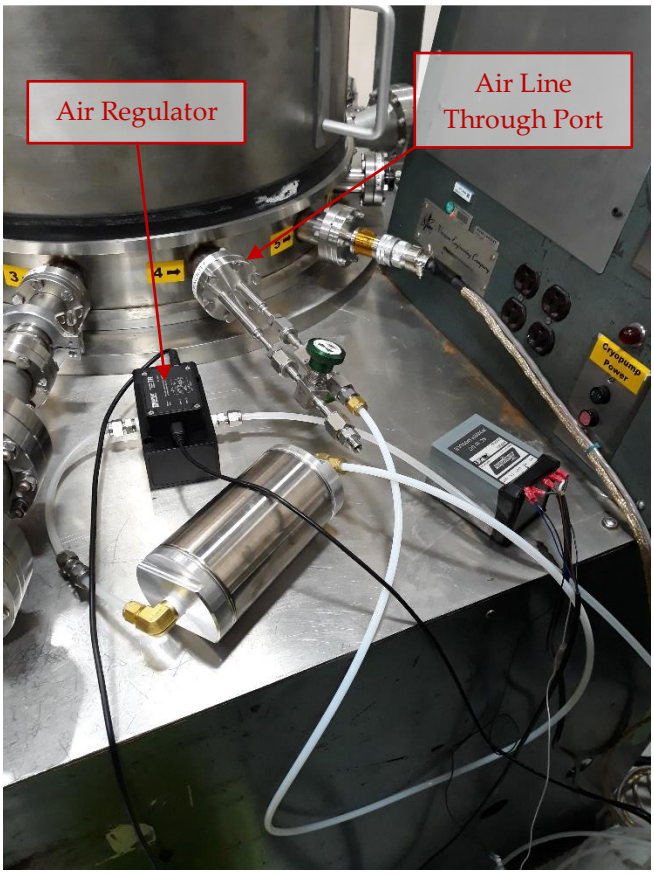

Fig. 29 Location of through port for the air line coming from the air regulator.

In Fig. 30 the coolant line is connected to port 12 while the heater power supply is connected to port 10. Barely seen off to the left is the port of the communication line to the load cylinder; this is port 7. The TC harness located inside of the chamber can be seen in Fig. 31. This allows for an easy connection between the TCs and the computer and utilized port number 3. The placement of the load cell and air cylinder can be seen in Fig. 32.

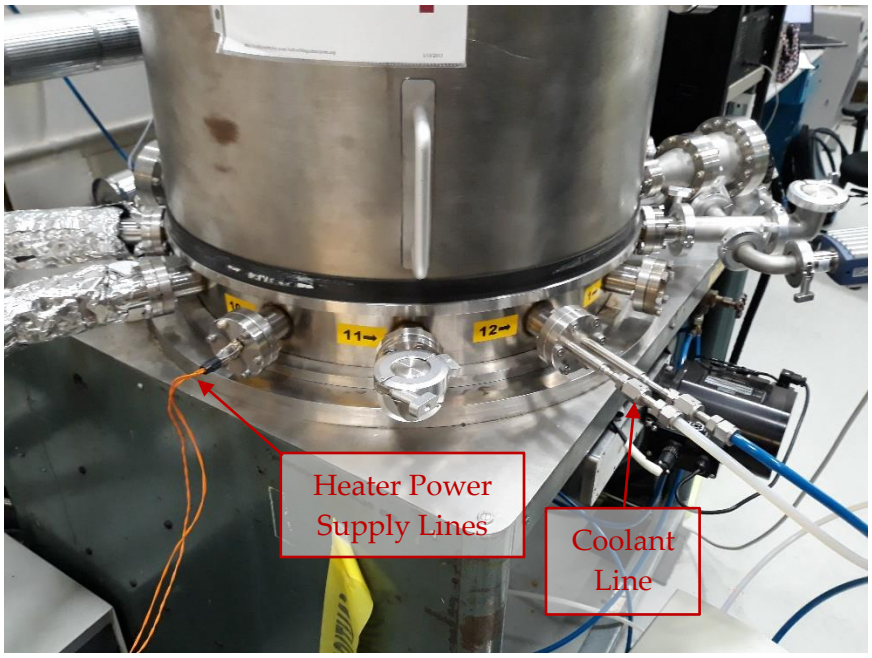

Fig. 30 Through port location for heater power supply and coolant lines.

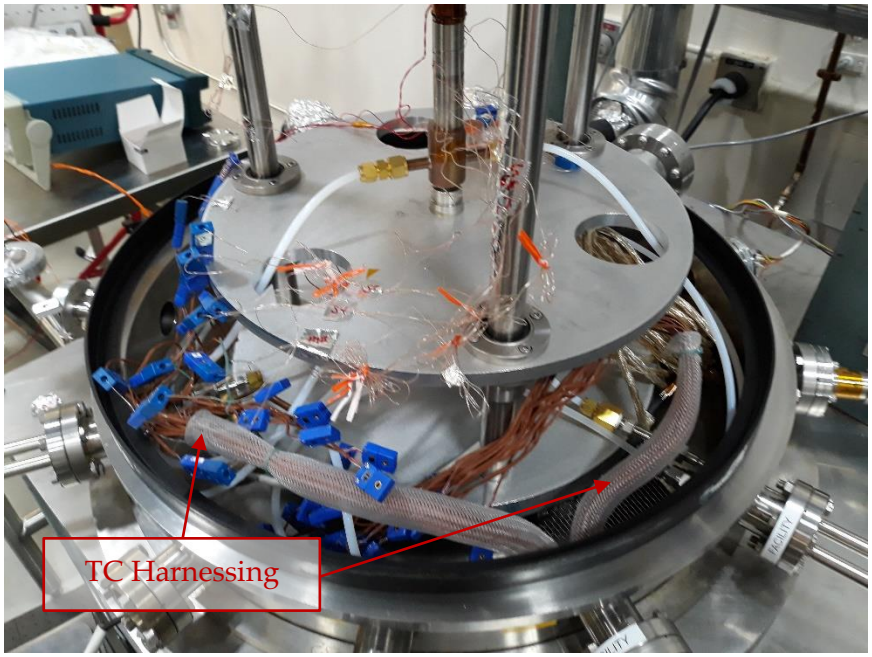

Fig. 31 Internal location of the TC harness.

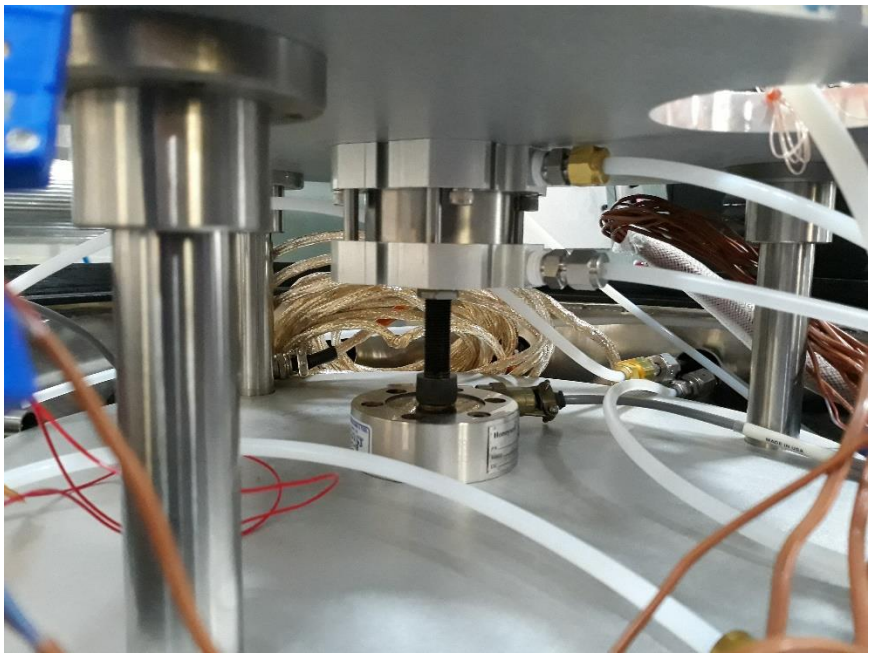

Fig. 32 Placement of air cylinder and load cell.

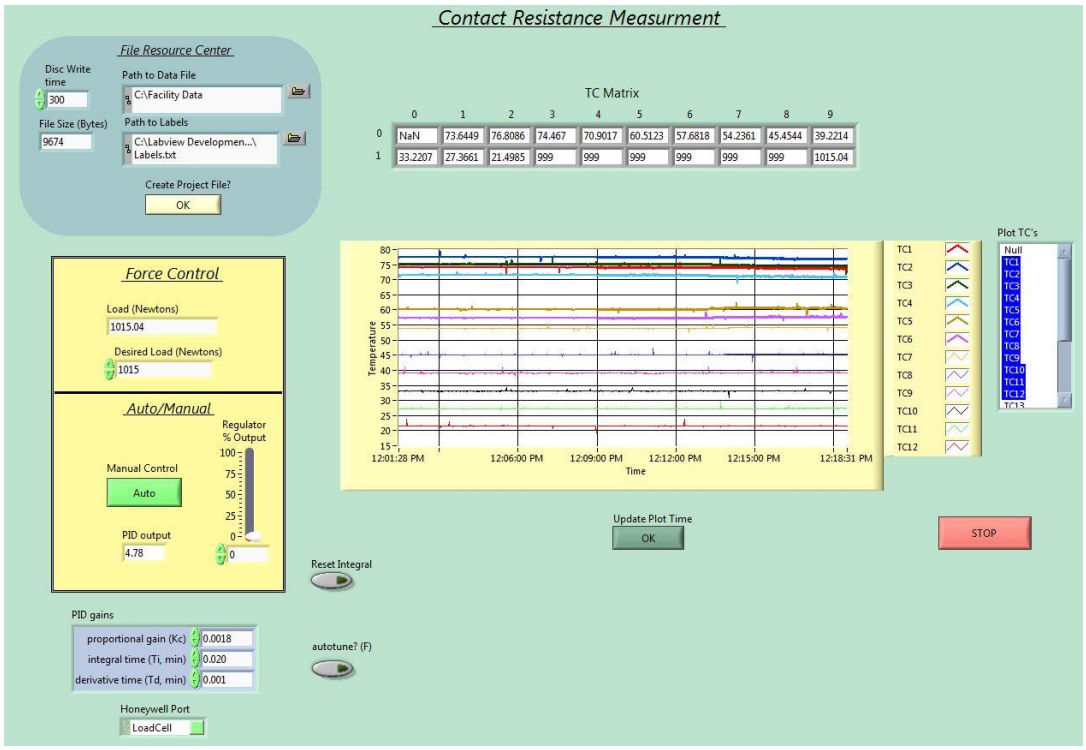

Fig. 33 Screen capture of LabView GUI during TCR data collection.

B. MATERIAL PROPERTIES

STAINLESS STEEL 304

The specific heat (c_p, Fig. 34) and thermal conductivity (k, Fig. 35) were collected from Touloukian data published in 1977 [20]. The raw data was graphed and then used to determine a best-fit curve that could be used to find the material properties at the desired temperatures. The temperature range that was used was truncated down to a range that included the temperatures within this study; the full range extended well outside of the temperatures of interest. In the Touloukian documentation it was stated that the specific heat has a 5% error, while the error for thermal conductivity 10%.

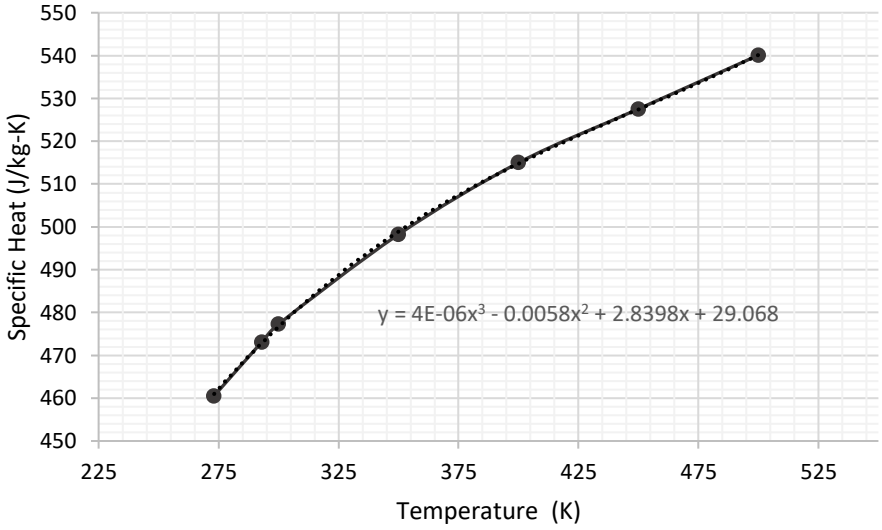

Fig. 34 Specific heat for SS304 with best-fit-line.

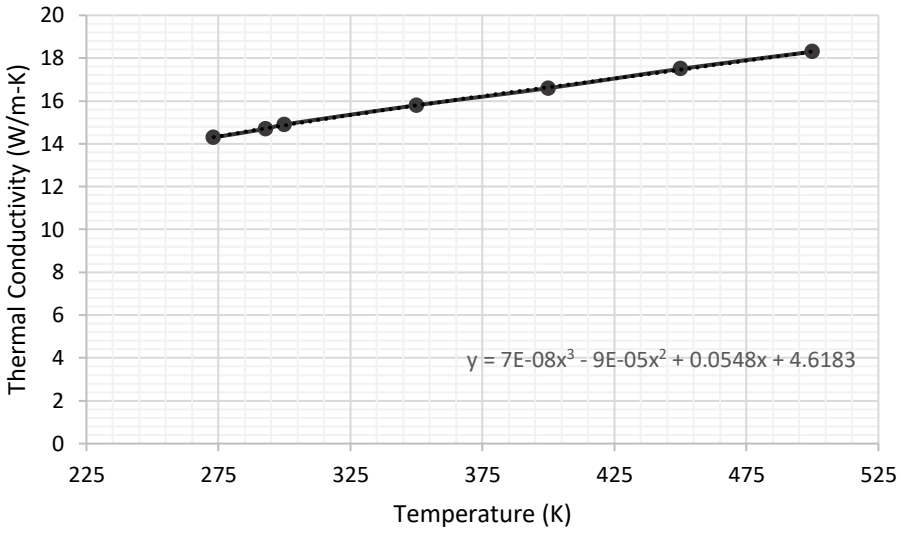

Fig. 35 Thermal conductivity of SS304 with best-fit-line.

Table 24 Touloukian raw data for SS304 specific heat.

Temperature (K)	Specific Heat (J/kg-K)
273.15	460.55
293	473.11
300	477.30
350	498.23
400	514.98
450	527.54
500	540.10

Table 25 Touloukian raw data for SS304 thermal conductivity.

Temperature (K)	Thermal Conductivity (W/m-K)
273.15	14.3
293	14.7
300	14.9
350	15.8
400	16.6
450	17.5
500	18.3

INVAR 36

Only the thermal conductivity (Fig. 36) is needed for the Invar Meter Bars since it is used to calculate the heat flux within the system.

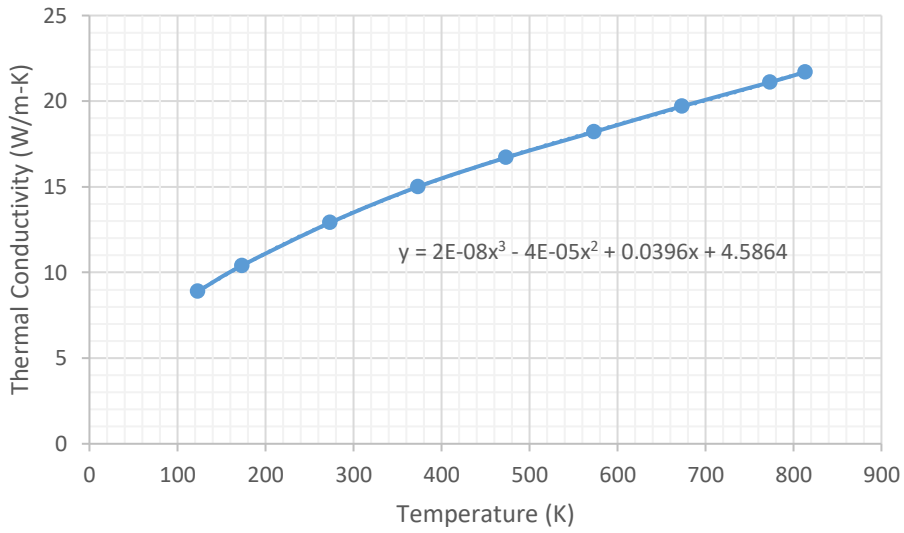

Fig. 36 Touloukian data, Curve 44 [30], for thermal conductivity of Invar with average curve and best-fit line equation.

Table 26 Touloukian data from Curve 44.

Temperature (K)	Thermal Conductivity (W/m-K)
123.2	8.9
173.2	10.4
273.2	12.9
373.2	15
473.2	16.7
573.2	18.2
673.2	19.7
773.2	21.1
813.2	21.7

C. CODE VERIFICATION TEST RESULTS

The results for the 6V and 8V test are presented here. The graphs are the same as the 4V test graphs presented in Section 4.4.

HEATER VOLTAGE – 6V

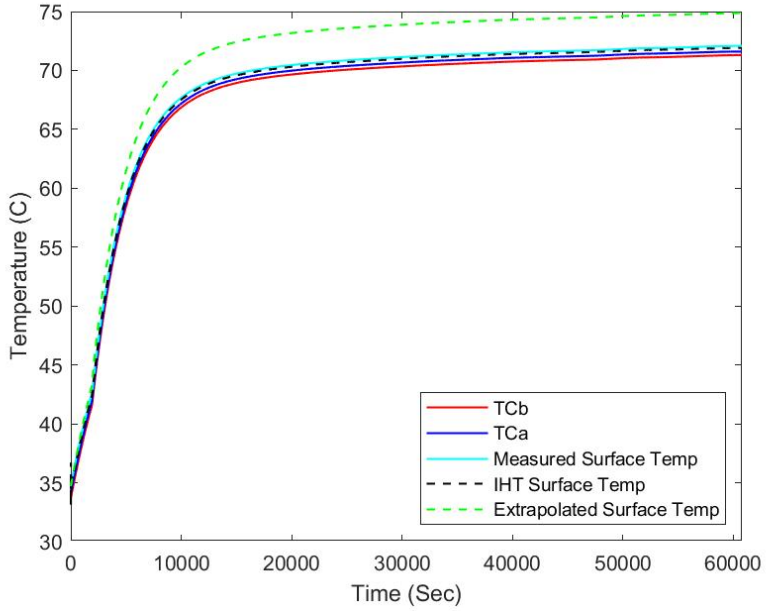

Fig. 37 Smoothed temperature over time for 6V validation test.

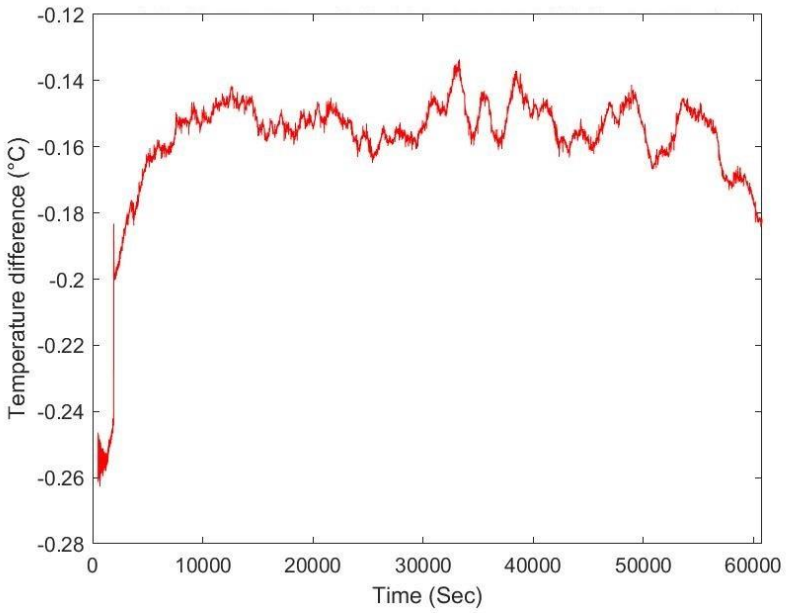

Fig. 38 Difference between IHT estimated surface temperature and measured surface temperature for 6V test.

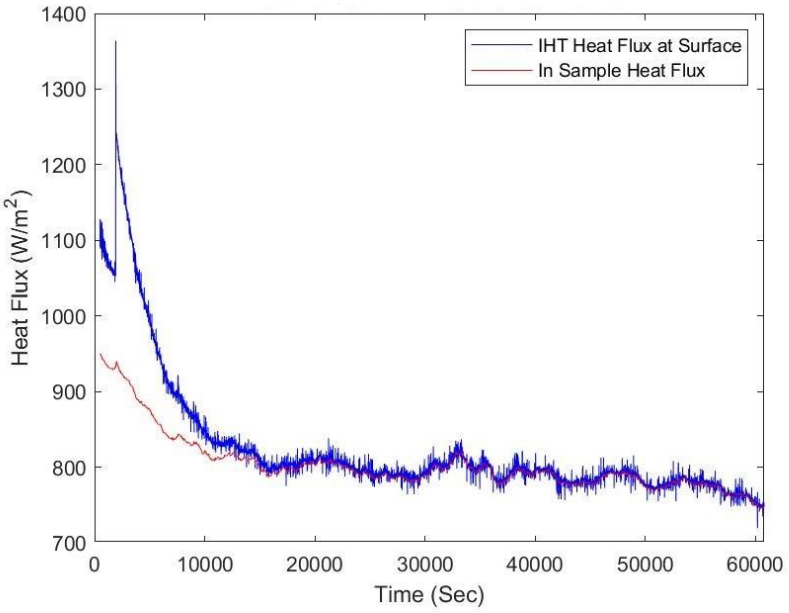

Fig. 39 Heat flux over time for both IHT surface heat flux and heat flux found using embedded TC data (In Sample) for 6V test.

HEATER VOLTAGE – 8V

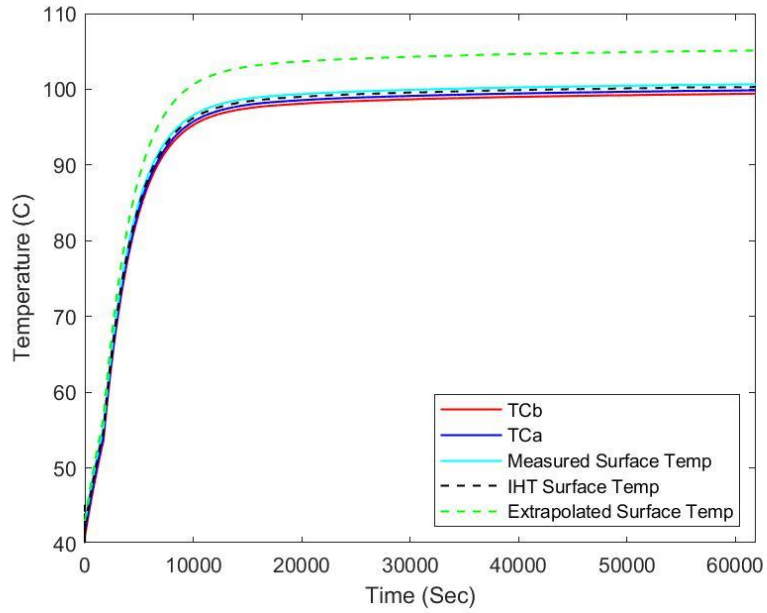

Fig. 40 Smoothed temperature over time for 8V validation test.

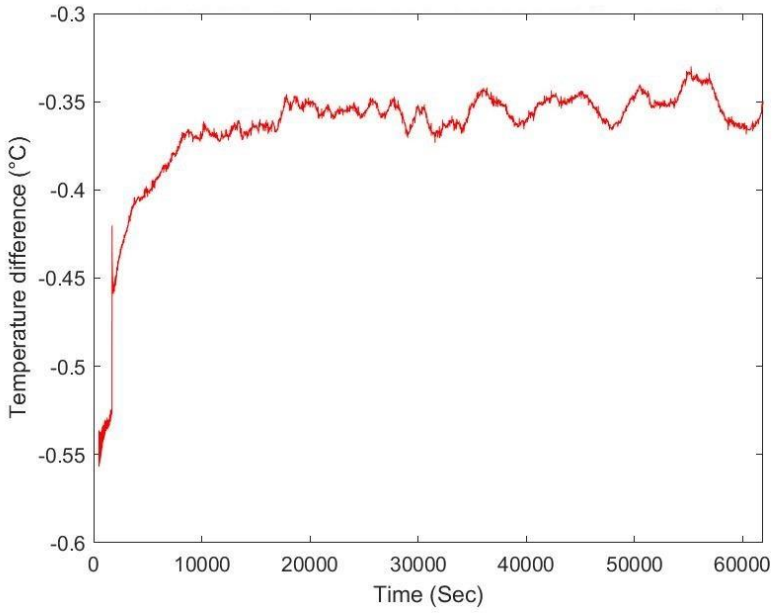

Fig. 41 Difference between IHT estimated surface temperature and measured surface temperature for 8V test.

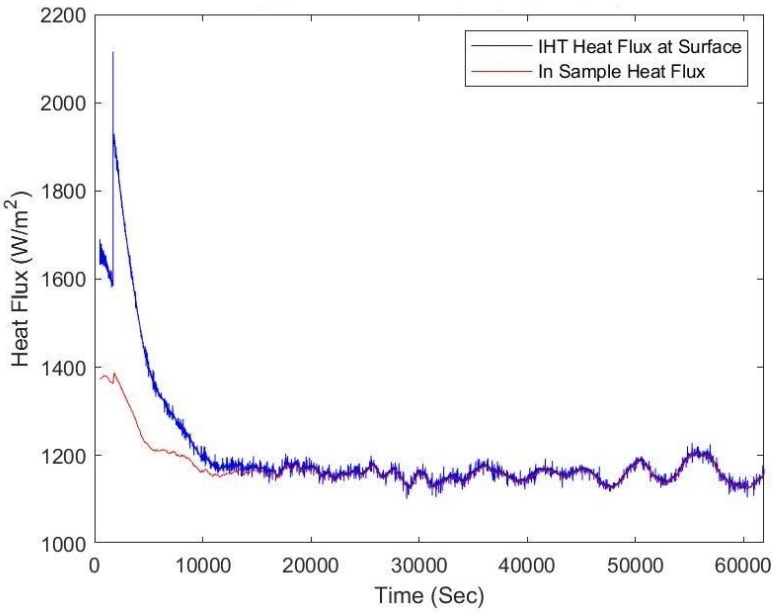

Fig. 42 Heat flux over time for both IHT surface heat flux and heat flux found using embedded TC data (In Sample) for 8V test.

D. INVAR METER BAR AND STAINLESS STEEL 304 SAMPLE SPECIFICATIONS

The precise location, angle, and depth of holes in the legacy Meter Bars were not previously recorded; therefore, this information was collected so the precise location of the hole interior where the TC bead is measuring the component temperature. Each Meter Bar from the legacy test setup was engraved with a "1" or "2" (for Meter Bars 1 and 2, respectively) near one of its flat surfaces to indicate the reference surface from which dimensional measurements were taken. Only information for Meter Bar 2 will be presented here since it was used for this study. The location of the hole entrance relative to the reference surface was used in combination with the angle and depth of the holes in order to determine the location of the bottom of the holes where the TC beads are positioned. A Gage Master Optical Comparator GM4 was used to determine the drill angle, while a Mitutoyo Absolute Digimatic Height Gage was used to find the location of the hole along the height of the cylinder.

A pin with a 0.91 mm diameter and length of 50.87 mm was found to fit in every hole and was used to determine the depth. The required geometry allowed the angle (θ), depth at angle

(*D*), and the location (height of hole, *x*) to be determined; these measurements are found in Fig. 43. The direction of the angle, off of 90°, was found based on the values of the measured angles. The difference measurement was then found by using the angle and depth at angle. This value was then added or subtracted from the exterior location to generate the adjusted height. The angle measurement was found by measuring the angle between the pin and the surface of the cylinder. Six measurements, three from each side of the pin, were taken and the difference from 90° was averaged. All values, along with the adjusted height location for each TC, can be found in Table 27, and the overall height of the Meter Bar was measured at 44.76 mm. This same process was repeated for each of the four test articles with the results reported in Table 28, and the figures with the drill angle of each hole can be found in Fig. 44– to Fig. 47.

Table 27 Hole measurements in Meter Bar.

	Hole Number			
Meter Bar 2	1	2	3	4
Angle (θ, deg)	1.24	-0.61	0.6	0.27
Depth at Angle (Da, mm)	10.58	10.8	11.31	90.1
Difference (x', mm)	0.23	-0.11	0.12	0.04
Height (hx, mm)	35.99	26.71	17.64	8.47
Adjusted Height (X, mm)	36.21	26.59	17.76	8.51

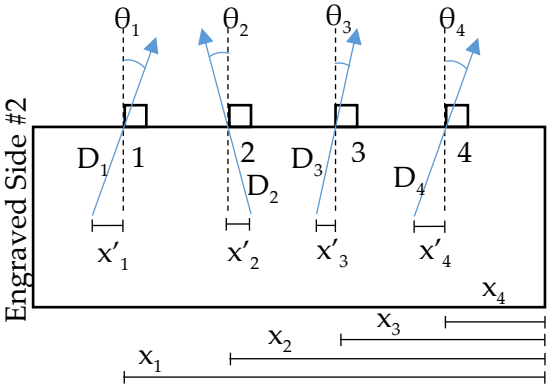

*Not to scale

Meter Bar 2:

Angle of Hole	Height of Hole
$\theta_1 = 1.24^\circ$	$hx_1 = 35.99$ mm
$\theta_2 = -0.61^\circ$	$hx_2 = 26.71$ mm
$\theta_3 = 0.60^\circ$	$hx_3 = 17.64$mm
$\theta_4 = 0.27^\circ$	$hx_4 = 8.47$mm

Depth at Angle

$D_1 = 10.58$ mm

$D_2 = 10.80$ mm

$D_3 = 11.31$ mm

$D_4 = 9.01$ mm

Fig. 43 Measurements of holes for Meter Bar.

Table 28 In-test article hole locations with uncertainties.

	Hole Number					
	1		2		3	
Sample 1	**Value**	**Uncertainty**	**Value**	**Uncertainty**	**Value**	**Uncertainty**
Angle (θ, deg)	0.62	0.39	0.26	0.78	-0.34	0.81
Depth at Angle (Da, mm)	11.55	0.02	11.65	0.02	11.57	0.07
Difference (x', mm)	0.12	0.03	0.05	0.03	-0.07	0.07
Height (hx, mm)	4.95	0.44	9.06	0.56	13.98	0.50
Adjusted Height (X, mm)	4.82	0.44	9.11	0.56	13.91	0.50
Sample 2						
Angle (θ, deg)	0.10	0.83	-1.64	0.65	0.43	0.34
Depth at Angle (Da, mm)	11.54	0.02	11.79	0.05	11.99	0.07
Difference (x', mm)	0.02	0.03	-0.34	0.05	0.09	0.07
Height (hx, mm)	5.08	0.23	9.2425	0.55	13.96	0.25
Adjusted Height (X, mm)	5.10	0.23	8.91	0.56	14.05	0.26
Sample 3						
Angle (θ, deg)	-0.62	0.32	0.65	0.65	0.47	0.81
Depth at Angle (Da, mm)	11.24	0.09	11.12	0.07	11.60	0.00
Difference (x', mm)	-0.12	0.09	0.13	0.07	0.09	0.02
Height (hx, mm)	4.44	0.13	9.4275	0.02	15.88	0.11
Adjusted Height (X, mm)	4.32	0.16	9.55	0.07	15.97	0.11
Sample 4						
Angle (θ, deg)	-0.63	0.57	0.45	0.99	0.80	0.79
Depth at Angle (Da, mm)	11.24	0.05	11.74	0.02	11.64	0.07
Difference (x', mm)	-0.12	0.05	0.09	0.03	0.16	0.07
Height (hx, mm)	4.42	0.03	9.5775	0.19	14.08	0.03
Adjusted Height (X, mm)	4.29	0.06	9.67	0.19	14.25	0.07

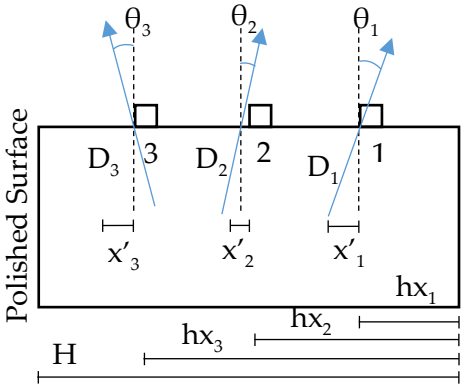

Test Article 1:

Angle of Hole	Height of Hole
$\theta_1 = 0.87^\circ$	$hx_1 = 4.95$ mm
$\theta_2 = 0.26^\circ$	$hx_2 = 9.06$ mm
$\theta_3 = -0.34^\circ$	$hx_3 = 13.98$ mm
Depth at Angle	H = 18.83 mm
$D_1 = 11.57$ mm	Dia = 24.12 mm
$D_2 = 11.67$ mm	
$D_3 = 11.59$ mm	

*Not to scale

Fig. 44 Measurements of holes for test article 1.

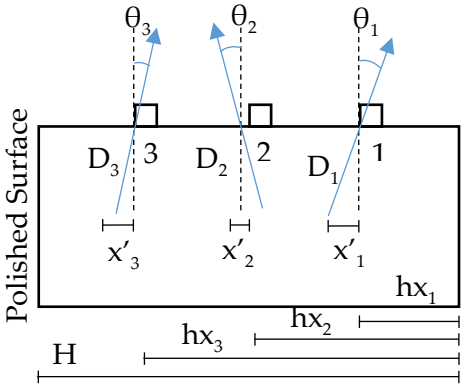

Test Article 2:

Angle of Hole	Height of Hole
$\theta_1 = 0.187^\circ$	$hx_1 = 5.08$ mm
$\theta_2 = -1.64^\circ$	$hx_2 = 9.24$ mm
$\theta_3 = 1.72^\circ$	$hx_3 = 13.96$ mm
Depth at Angle	H = 19.07 mm
$D_1 = 11.56$ mm	Dia = 24.12 mm
$D_2 = 11.82$ mm	
$D_3 = 12.01$ mm	

*Not to scale

Fig. 45 Measurements of holes for test article 2.

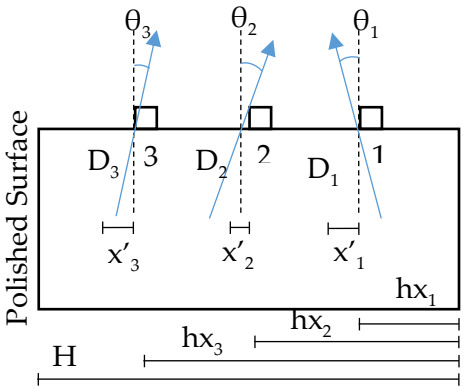

Test Article 3:

Angle of Hole	Height of Hole
θ_1 = -0.615°	hx_1 = 4.44 mm
θ_2 = 0.65°	hx_2 = 9.43 mm
θ_3 = 0.47°	hx_3 = 15.88 mm
Depth at Angle	H = 19.01 mm
D_1 = 11.26 mm	Dia = 24.13 mm
D_2 = 11.14 mm	
D_3 = 11.62 mm	

*Not to scale

Fig. 46 Measurements of holes for test article 3.

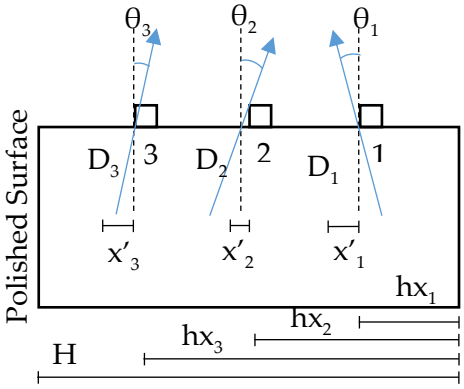

Test Article 4:

Angle of Hole	Height of Hole
θ_1 = -0.63°	hx_1 = 4.42 mm
θ_2 = 0.45°	hx_2 = 9.58 mm
θ_3 = 0.80°	hx_3 = 14.08 mm
Depth at Angle	H = 18.51 mm
D_1 = 11.24 mm	Dia = 24.11 mm
D_2 = 11.74 mm	
D_3 = 11.64 mm	

*Not to scale

Fig. 47 Measurements of holes for test article 4.

E. SURFACE ROUGHNESS OF STAINLESS STEEL 304 TEST ARTICLES

A Zygo NewVIew 6K was used to measure the surface roughness of each test article before the tests were conducted (after bead blasting) and then after the test was conducted. The results only demonstrate the difficulty in understanding the characteristic of surfaces. The results can be found in Table 29 and Table 30.

Table 29 Surface characteristics for test articles 1 and 2.

	Sample 1			Sample 2		
When Measured	RMS (μm)	PV (μm)	RA (μm)	RMS	PV	RA
Before test 5	0.857	6.163	0.700	0.741	5.858	0.597
After test 5	0.775	5.950	0.621	0.836	5.243	0.673
Before test 6	0.791	6.089	0.638	0.843	5.802	0.681
After test 6	0.885	5.528	0.723	0.817	6.067	0.657

Table 30 Surface characteristics for test articles 3 and 4.

	Sample 3			Sample 4		
When Measured	RMS (μm)	PV (μm)	RA (μm)	RMS	PV	RA
Before test 5	0.816	5.858	0.660	0.777	6.564	0.625
After test 5	0.855	5.523	0.696	0.795	5.877	0.648
Before test 6	0.792	5.781	0.642	0.818	6.408	0.662
After test 6	0.766	6.201	0.614	0.841	5.709	0.678

F. COLLECTED THERMOCOUPLE DATA FOR EACH TEST

The average of the last 5 minutes for each TC embedded in the test articles is presented in Table 31 and Table 32. The results for the extra tests can be found in Table 33.

Table 31 Thermocouple data for all mid-vacuum tests using test articles 1 and 2.

Test Run	Pressure (MPa)	TC Number					
		TC2	TC3	TC4	TC5	TC6	TC7
Test1	0.159	88.8	86.7	83.2	59.9	56.9	53.5
	0.489	82.4	80.1	76.5	60.0	56.9	53.6
	1.421	77.5	75.1	71.5	60.2	57.2	53.8
	2.244	76.5	74.1	70.5	60.7	57.8	54.3
	3.221	75.6	73.2	69.7	60.6	57.8	54.3
	4.014	75.1	72.7	69.3	60.6	57.8	54.4
Test2	0.159	89.4	86.6	83.4	55.8	53.1	50.3
	0.489	84.7	81.7	78.4	57.5	54.7	51.8
	1.421	79.8	76.6	73.4	58.8	56.0	53.0
	2.244	78.5	75.3	72.0	59.5	56.6	53.6
	3.221	77.4	74.2	70.9	59.6	56.8	53.8
	4.014	76.7	73.5	70.3	59.7	56.9	53.9
Test3	0.159	88.5	85.8	82.8	57.7	54.8	51.1
	0.489	84.5	81.6	78.4	58.8	55.8	52.1
	1.421	79.9	76.8	73.6	60.0	57.0	53.2
	2.244	78.7	75.6	72.3	60.7	57.6	53.8
	3.221	77.8	74.6	71.3	60.8	57.8	54.0
	4.014	77.1	74.0	70.7	60.9	57.8	54.1
Test5	1.421	81.3	78.0	75.9	58.9	55.6	52.3
	2.244	79.7	76.3	74.2	59.5	56.2	52.8
	3.221	78.6	75.1	73.0	60.2	57.0	53.6
	4.014	78.0	74.4	72.3	60.4	57.1	53.7
Test6	0.159	89.9	87.6	84.6	57.7	55.0	52.2
	0.489	85.5	83.1	80.0	58.2	55.7	52.7
	1.421	80.9	78.4	75.2	59.1	56.6	53.6
	2.244	79.3	76.8	73.6	59.3	56.9	53.8
	3.221	78.2	75.7	72.5	59.6	57.2	54.1
	4.014	77.6	75.1	71.9	59.7	57.4	54.2

Table 32 Thermocouple data for all mid-vacuum tests using test articles 3 and 4.

Test Run	Pressure (MPa)	TC Number					
		TC 2	TC3	TC4	TC5	TC6	TC7
Test1	0.159	94.5	91.2	87.5	57.5	53.8	51.0
	0.489	88.1	84.6	80.8	58.9	55.1	52.2
	1.421	82.2	78.5	74.7	60.2	56.4	53.4
	2.244	80.4	76.7	72.9	60.5	56.7	53.7
	3.221	79.1	75.4	71.6	60.7	56.9	53.9
	4.014	78.4	74.6	70.9	60.7	57.0	54.0
Test2	0.159	95.4	92.3	88.1	57.0	52.9	50.4
	0.489	89.5	86.2	81.9	58.8	54.6	52.0
	1.421	83.2	79.6	75.2	60.4	56.2	53.5
	2.244	81.0	77.3	73.0	60.7	56.6	53.9
	3.221	79.5	75.8	71.6	60.9	56.8	54.2
	4.014	78.7	75.0	70.8	60.9	57.0	54.3
Test3	0.489	86.1	83.1	79.6	57.2	53.6	50.8
	1.421	81.7	78.6	75.0	58.8	55.1	52.2
	2.244	80.2	77.1	73.5	59.5	55.8	52.8
	3.221	79.2	75.9	72.3	59.8	56.2	53.2
	4.014	78.5	75.3	71.7	60.0	56.4	53.4
Test5	0.221	100.5	97.4	93.4	56.1	52.2	49.9
	0.489	93.3	89.9	85.6	58.4	54.3	51.8
	1.421	85.4	81.7	77.3	59.9	55.7	53.0
	2.244	82.9	79.1	74.8	60.3	56.1	53.4
	3.221	81.1	77.4	73.0	60.5	56.4	53.7
	4.014	80.3	76.5	72.2	60.6	56.6	53.9
Test6	0.159	99.0	95.5	92.0	54.7	51.2	49.2
	0.489	91.5	87.7	84.1	56.7	53.0	50.8
	1.421	84.5	80.3	76.8	59.2	55.2	52.9
	2.244	82.2	78.0	74.5	59.7	55.7	53.4
	3.221	80.2	75.9	72.4	60.1	56.1	53.8

Table 33 Thermocouple data for all extra tests.

Test Run	Pressure (MPa)	TC Number TC2	TC3	TC4	TC5	TC6	TC7
High Vac	0.489	89.6	86.4	81.9	59.6	55.7	52.8
S3S4	1.421	82.3	78.9	74.3	61.5	57.7	54.6
	3.221	80.2	76.7	72.2	61.9	58.1	55.0
High Vac	0.489	94.3	90.5	87.3	59.8	55.7	52.3
S3S4	1.421	85.0	80.8	77.5	62.2	58.1	54.5
Retest	3.221	82.4	78.1	74.8	62.5	58.6	54.9
S2S1	0.489	86.3	83.6	80.8	56.7	54.5	51.5
	1.421	79.2	76.2	73.3	58.9	56.7	53.5
	3.221	78.0	74.9	72.1	59.8	57.6	54.4
S2S1	0.489	88.9	85.8	83.3	58.1	54.9	52.3
Retest	1.421	80.8	77.5	74.8	60.2	57.1	54.2
	3.221	78.4	75.1	72.5	60.5	57.5	54.6
S4S3	0.489	87.2	85.2	81.1	58.8	54.1	50.7
	1.421	80.0	77.9	73.7	60.8	56.2	52.6
	3.221	78.0	75.9	71.7	61.2	56.7	53.1

G. RESULTS COLLECTED FOR EACH TEST

Table 34 Average TCR results, with uncertainty, for test articles 1 and 2 for both methods of estimating the interface surface temperature for each step of all mid-vacuum tests.

S1S2	Interface Pressure (MPa)	IHT Estimated Surface Temperatures TCR Average ($x10^{-5}$ °C-m²/W)	Uncertainty Average	Extrapolated Surface Temperatures TCR Average ($x10^{-5}$ °C-m²/W)	Uncertainty Average
Step 1	0.159	184.9	±49	188.9	±62
Step 2	0.489	120.7	±27	124.7	±46
Step 3	1.421	70.3	±18	73.2	±39
Step 4	2.244	51.5	±13	54.3	±36
Step 5	3.221	39.6	±11	42.2	±36
Step 6	4.014	33.6	±9	36.2	±35

Table 35 Average TCR results, with uncertainty, for test articles 3 and 4 for both methods of estimating the interface surface temperature for each step of all mid-vacuum tests.

		IHT Estimated Surface Temperatures		Extrapolated Surface Temperatures	
S3S4	Interface Pressure (MPa)	TCR Average ($x10^{-5}$ °C-m²/W)	Uncertainty Average	TCR Average ($x10^{-5}$ °C-m²/W)	Uncertainty Average
Step 1	0.1592	298.1	±71	302.7	±72
Step 2	0.4885	189.4	±44	193.5	±60
Step 3	1.4213	101.3	±23	102.2	±44
Step 4	2.2436	76.4	±17	76.8	±40
Step 5	3.2207	59.5	±13	61.4	±38
Step 6	4.0142	50.3	±11	48.8	±37

Table 36 TCR results for all tests using test articles 1 and 2 for IHT estimated surface temperatures.

		IHT Estimated Surface Temperature (°C)			
Test Run	Pressure (MPa)	TCR Results ($x10^{-5}$ °C-m²/W)	Random Uncertainty	Systematic Uncertainty	Total Uncertainty
Test1	0.159	152.6	±7.3	±38.4	±39
	0.489	85.3	±4.2	±21.1	±21
	1.421	39.1	±2.6	±9.8	±10
	2.244	25.2	±2.9	±6.5	±7
	3.221	19.6	±2.6	±5.2	±6
	4.014	15.8	±1.9	±4.4	±5
Test2	0.159	205.6	±9.5	±53.7	±55
	0.489	132.0	±3.5	±17.2	±18
	1.421	68.9	±4.1	±17.2	±18
	2.244	49.3	±2.8	±12.3	±13
	3.221	37.9	±2.4	±9.5	±10
	4.014	32.5	±2.0	±8.1	±8
Test3	0.159	167.0	±6.6	±41.5	±42
	0.489	108.7	±4.4	±26.1	±27
	1.421	51.2	±2.3	±12.1	±12
	2.244	32.9	±1.6	±7.8	±8
	3.221	23.3	±1.7	±5.7	±6
	4.014	18.5	±1.3	±4.6	±5
Test5	1.421	94.6	±3.9	±23.9	±24
	2.244	71.4	±2.9	±17.9	±18
	3.221	52.7	±2.7	±13.2	±14
	4.014	43.5	±2.3	±10.9	±11
Test 6	0.159	214.4	±9.1	±59.0	±60
	0.489	157.3	±6.5	±42.7	±43
	1.421	97.5	±4.0	±26.2	±26
	2.244	78.8	±3.3	±21.2	±21
	3.221	64.4	±2.7	±17.3	±18
	4.014	57.5	±2.6	±15.5	±16

Table 37 TCR results for all tests using test articles 3 and 4 for IHT estimated surface temperatures.

		IHT Estimated Surface Temperature (°C)			
Test Run	Pressure (MPa)	TCR Results ($x10^{-5}$ °C-m²/W)	Random Uncertainty	Systematic Uncertainty	Total Uncertainty
Test1	0.159	251.2	±4.0	±58.9	±59
	0.489	160.3	±2.8	±36.5	±37
	1.421	85.9	±1.8	±19.4	±19
	2.244	64.8	±1.5	±14.7	±15
	3.221	50.6	±1.6	±11.5	±12
	4.014	44.2	±1.4	±10.1	±10
Test2	0.159	251.4	±3.8	±57.3	±57
	0.489	165.3	±3.0	±36.8	±37
	1.421	82.7	±3.4	±18.1	±18
	2.244	59.8	±1.6	±13.2	±13
	3.221	46.5	±1.6	±10.4	±11
	4.014	38.9	±1.5	±8.8	±9
Test3	0.489	183.1	±3.2	±44.3	±44
	1.421	112.6	±2.4	±26.7	±27
	2.244	88.9	±2.2	±21.0	±21
	3.221	73.7	±1.0	±17.5	±17
	4.014	65.0	±1.9	±15.4	±16
Test5	0.221	333.2	±1.4	±78.3	±78
	0.489	207.1	±3.3	±46.3	±46
	1.421	105.9	±2.3	±23.0	±23
	2.244	78.0	±1.5	±16.9	±17
	3.221	61.4	±1.6	±12.5	±13
	4.014	53.1	±1.1	±10.9	±11
Test6	0.159	356.5	±4.9	±89.2	±89
	0.489	231.3	±4.5	±55.2	±55
	1.421	119.4	±1.4	±27.4	±27
	2.244	90.6	±2.2	±20.7	±21
	3.221	65.4	±1.2	±15.0	±15

Table 38 TCR results for all tests using test articles 1 and 2 for extrapolated estimated surface temperatures.

		Extrapolated Estimated Surface Temperature			
Test Run	Pressure (MPa)	TCR Results ($x10^{-5}$ °C-m²/W)	Random Uncertainty	Systematic Uncertainty	Total Uncertainty
Test1	0.159	157.7	±16.1	±53.1	±55
	0.489	90.6	±14.9	±39.6	±42
	1.421	43.8	±13.4	±33.6	±36
	2.244	29.6	±13.2	±32.5	±35
	3.221	23.6	±12.2	±32.4	±35
	4.014	20.0	±12.2	±32.3	±35
Test2	0.159	209.6	±12.9	±64.7	±66
	0.489	135.6	±10.8	±38.2	±40
	1.421	72.0	±7.9	±36.5	±37
	2.244	52.5	±7.7	±33.9	±35
	3.221	41.0	±7.2	±32.8	±34
	4.014	35.5	±6.8	±32.5	±33
Test3	0.159	169.3	±9.1	±54.2	±55
	0.489	111.3	±7.9	±41.6	±42
	1.421	53.5	±6.0	±32.7	±33
	2.244	35.3	±6.0	±30.7	±31
	3.221	25.6	±12.0	±33.4	±36
	4.014	21.0	±5.9	±29.9	±31
Test5	1.421	95.7	±7.0	±42.1	±43
	2.244	72.3	±9.5	±37.3	±38
	3.221	53.2	±9.3	±34.9	±36
	4.014	44.1	±9.8	±33.6	±35
Test 6	0.159	218.9	±14.7	±71.7	±73
	0.489	161.3	±12.6	±57.3	±59
	1.421	101.1	±10.9	±44.7	±46
	2.244	82.1	±10.6	±41.4	±43
	3.221	67.5	±10.4	±39.2	±41
	4.014	60.4	±10.0	±38.3	±40

Table 39 TCR results for all tests using test articles 3 and 4 for extrapolated estimated surface temperatures.

		Extrapolated Estimated Surface Temperature (°C)			
Test Run	Pressure (MPa)	TCR Results ($x10^{-5}$ °C-m²/W)	Random Uncertainty	Systematic Uncertainty	Total Uncertainty
Test1	0.159	254.5	±10.4	±71.4	±72
	0.489	163.3	±9.0	±51.9	±53
	1.421	88.5	±7.5	±39.7	±40
	2.244	67.4	±7.2	±37.1	±38
	3.221	53.0	±6.4	±35.6	±36
	4.014	46.3	±5.5	±35.2	±36
Test2	0.159	257.0	±17.3	±69.8	±72
	0.489	170.8	±16.3	±51.9	±54
	1.421	87.6	±14.3	±38.9	±41
	2.244	64.2	±12.7	±35.6	±38
	3.221	50.8	±12.1	±35.1	±37
	4.014	42.8	±11.1	±34.2	±36
Test3	0.489	186.5	±10.6	±59.2	±60
	1.421	115.8	±10.0	±45.6	±47
	2.244	92.0	±9.5	±41.9	±43
	3.221	76.4	±8.4	±40.0	±41
	4.014	67.9	±9.1	±38.9	±40
Test5	0.221	338.8	±16.5	±41.8	±45
	0.489	212.3	±15.5	±59.9	±62
	1.421	110.6	±13.6	±40.9	±43
	2.244	82.4	±12.5	±37.1	±39
	3.221	65.7	±12.2	±35.1	±37
	4.014	57.3	±11.7	±34.5	±36
Test6	0.159	360.4	±12.8	±99.9	±101
	0.489	234.5	±10.5	±68.0	±69
	1.421	122.0	±9.7	±45.0	±46
	2.244	93.1	±9.8	±40.6	±42
	3.221	67.8	±9.6	±37.3	±39

Table 40 Average in test article heat flux for test articles 1 and 2 with uncertainties.

		In Sample Heat Flux (W/m²)			
Test Run	Pressure (MPa)	Empirical	Random Uncertainty	Systematic Uncertainty	Total Uncertainty
Test1	0.159	10656.2	±471.6	±2679.3	±2720
	0.489	10905.4	±477.0	±2680.6	±2723
	1.421	10814.4	±447.6	±2671.1	±2708
	2.244	10805.8	±467.4	±2670.1	±2711
	3.221	10662.7	±474.1	±2663.4	±2705
	4.014	10583.6	±439.7	±2659.8	±2696
Test2	0.159	10166.5	±452.1	±2655.3	±2694
	0.489	10574.0	±450.7	±2666.9	±2705
	1.421	10777.1	±483.6	±2670.3	±2714
	2.244	10868.4	±472.1	±2673.2	±2715
	3.221	10833.3	±469.1	±2670.7	±2712
	4.014	10730.8	±441.7	±2641.2	±2678
Test3	0.159	10800.1	±420.8	±2681.7	±2715
	0.489	11236.3	±443.4	±2694.8	±2731
	1.421	11556.5	±454.8	±2703.7	±2742
	2.244	11710.1	±463.4	±2709.3	±2749
	3.221	11688.0	±471.5	±2707.2	±2748
	4.014	11595.5	±467.3	±2702.7	±2743
Test5	1.421	10580.9	±409.9	±2667.0	±2698
	2.244	10691.4	±433.6	±2670.0	±2705
	3.221	10740.9	±425.5	±2671.1	±2705
	4.014	10858.6	±424.0	±2675.0	±2708
Test 6	0.159	9599.5	±403.3	±2638.4	±2669
	0.489	9744.2	±392.1	±2638.5	±2667
	1.421	9854.2	±392.8	±2637.7	±2667
	2.244	9862.4	±389.0	±2636.3	±2665
	3.221	9867.3	±389.4	±2635.5	±2664
	4.014	9863.5	±393.6	±2634.7	±2664

Table 41 Average in test article heat flux for test articles 3 and 4 with uncertainties.

		In Sample Heat Flux (W/m²)			
Test Run	Pressure (MPa)	Empirical	Random Uncertainty	Systematic Uncertainty	Total Uncertainty
Test1	0.159	9785.1	±141.2	±2292.1	±2296
	0.489	10130.4	±142.1	±2302.8	±2307
	1.421	10259.7	±159.3	±2304.5	±2310
	2.244	10277.6	±138.1	±2303.8	±2308
	3.221	10270.5	±142.9	±2302.7	±2307
	4.014	10203.5	±128.5	±2299.2	±2303
Test2	0.159	10121.4	±143.7	±2307.2	±2312
	0.489	10435.0	±154.7	±2317.9	±2323
	1.421	10694.3	±226.7	±2326.1	±2337
	2.244	10654.0	±147.3	±2322.8	±2327
	3.221	10481.4	±162.6	±2313.7	±2319
	4.014	10420.7	±134.1	±2310.4	±2314
Test3	0.489	9373.4	±150.0	±2266.4	±2271
	1.421	9619.6	±158.3	±2274.3	±2280
	2.244	9681.3	±135.2	±2276.3	±2280
	3.221	9676.6	±119.9	±2275.5	±2279
	4.014	9684.1	±117.5	±2275.4	±2278
Test5	0.221	9605.1	±114.2	±2256.7	±2260
	0.489	10361.2	±149.1	±2315.8	±2321
	1.421	10784.5	±149.4	±2331.9	±2337
	2.244	10813.3	±121.1	±2331.4	±2335
	3.221	10702.6	±150.0	±2147.2	±2152
	4.014	10631.3	±126.6	±2143.9	±2148
Test6	0.159	9055.2	±123.1	±2264.8	±2268
	0.489	9561.8	±160.7	±2280.7	±2286
	1.421	10046.4	±110.9	±2297.5	±2300
	2.244	10085.8	±134.9	±2297.7	±2302
	3.221	10125.1	±113.5	±2298.2	±2301

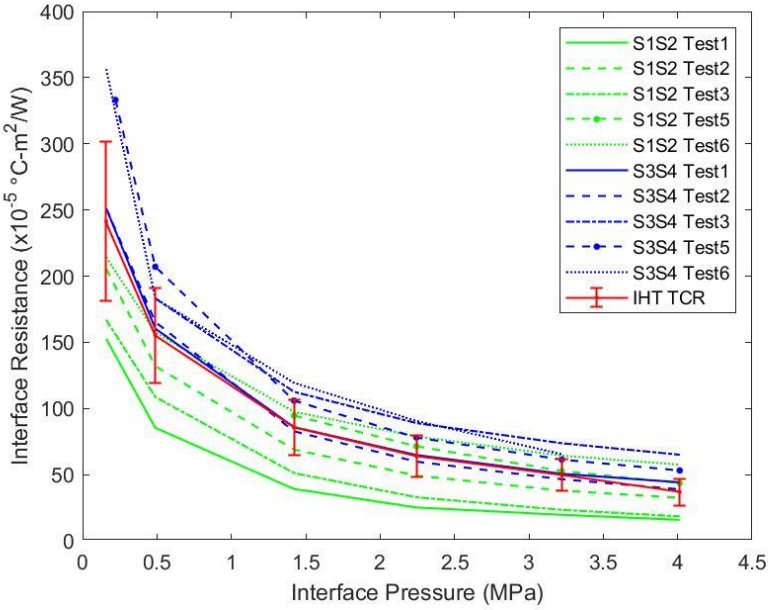

Fig. 48 All TCR results found with IHT surface estimates including total average with error bars.

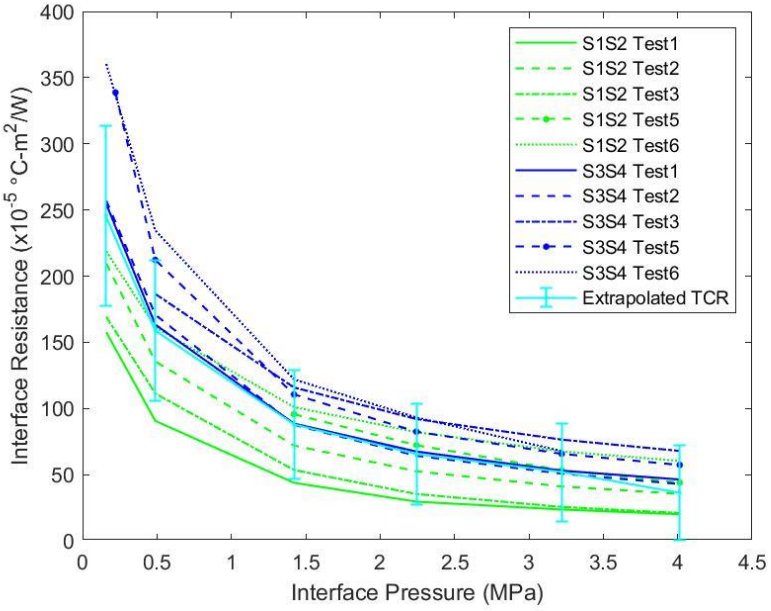

Fig. 49 All TCR results found with extrapolated surface estimates including total average with error bars.

H. DATA COLLECTION PROCEDURE

Introduction

This procedure was followed during the TCR data collection tests. The time to thermal equilibrium was determined by using an Excel document that was setup and used during CERES TVAC testing since 0.5°C/hr was also used for thermal equilibrium.

Test Fixture Components

- Steel and Aluminum frame
- Load cell with signal conditioner
- Air cylinder
- Copper heat sink
- Copper heater
- Invar Meter Bar
- Stainless Steel Bell Jar
- 36-gauge T-type Thermocouples
- Vacuum Grease
- Kapton and Aluminum Tape

Procedure

1. Verify the presence of all components needed for the test article stack
    a. Stack sequence from bottom:
        i. heat sink – in chamber
        ii. cold Meter Bar – in chamber
        iii. test article 2
        iv. test article 1
        v. heater – in chamber
2. Verify that all TCs are securely placed in the holes of Meter Bar and each test article using vacuum grease and aluminum tape
3. Attach TCs to heater and heat sink with Kapton tape
4. Verify that all cables and tubing are connected to the correct external and internal components and that power is available to all equipment
5. Start the LabView software and follow any instructions pertaining to data collection

6. While working inside the vacuum chamber, place the heat sink at the bottom and build the column according to the stack sequence found above ending with the heater at the top of the sample column
    a. This should be done within the frame so that the weight of the horizontal plates will assist with assembling the stack
    b. One side of the heat sink and heater has a dimple. There is a peg that the dimple will engage with on the corresponding side of the frame
    c. Allow a small amount of compressive force to be applied by the horizontal platen to hold stack in place
    d. Apply a small amount of vacuum grease to each polished surface
7. Hand tighten each bolt located on the top and bottom of the top place of the test fixture just until contact is made to the top plate
8. Tare out the load cell by removing any compressive load that is applied and follow the procedure presented by Honeywell
9. Close the chamber and follow the lab procedure to bring the Bell Jar to rough vacuum
10. Once at the desired vacuum, set the desired compressive force in Newtons within the appropriate field in the LabView software GUI
11. Start collecting data by generating the data file with the desired name
12. Set the power for the heater to the correct voltage/amperage for the desired temperature
13. Set the chiller temperature to the desired coolant temperature and allow the coolant to run through the heat sink
14. Wait until thermal stability is reached.
15. Continue recording data for a set amount of time
16. Can repeat steps 10, 12, or 13 if a different compressive force or temperature gradient is desired
17. After data collection is completed stop coolant flow and power off heater, remove compressive force and bring the chamber to ambient
18. Remove sample column from frame being careful to not damage the surfaces or the thermocouples in the Meter Bar

I. INVERSE HEAT TRANSFER FUNCTION USED WITH MATLAB CODE

```
function [T, q, Ti, qi] = Implicit_Direct_Solve(dx, dxi, dt, TCb, TCa,...
    test article_num, N, N_i)

%TC layout, TC1 is the heater TC
%TC2     TC3    TC4    | TC5    TC6    TC7    TC8    TC9    TC10    TC11
%SA_TC2  SA_TC3 SA_TC4 | SB_TC5 SB_TC6 SB_TC7 MB_TC8 MB_TC9 MB_TC10 MB_TC11

%    TC locations along test articles
```

```
%
% L_Surface    ____________  surface
% |            |           |    for inverse indirect: L_i = TC to surface
% | L_TCa      |      *----|--- TCa
% | |          |           |   for Inverse direct: L = distance btw TC
% | | L_TCb    |      *----|--- TCb
% | | |        |           |
% | | |  L_TCc |      *----|--- TCc
% | | | |      |           |
% | | | | x = 0--------------
%

M = numel(TCb); %time total in sec
rho= 8000;
%used to fill first time step %on 9/18 this was changed from TCb to TCa
Tzero = TCa(1);

%fill matricies with zeros
q = zeros(1,M);
T = zeros(N, M);
RHS = zeros(1,N-2);
Ti = zeros(N_i, M);
qi = zeros(N_i, M);

%variable for displaying final surface temp and heat flux
avg = 300; %used to take average of the last 5min of data
Temp_Sum = zeros(1, avg);
HF_Sum = zeros(1, avg);

%fill initial condition for all nodes and fill LD matrix with zero,
for i=1:N
    T(i,1) = Tzero;
    LD(i) = 0;
    D(i) = 0;
    UD(i) = 0;
end

for m = 1:M %pull measured TC data as boundary nodes
    T(1,m) = TCb(m);
    T(N,m) = TCa(m);
end

%direct solve
for m=1:M-1 %advances to next time step
    k = zeros(N);

    for i=1:N %advances nodal location
        %calculates conductivity after the node number advances
        k(i) = Thermal_Conductivity(T(i,m));
        %calculates specific heat for each new node
        c(i) = Specific_Heat(T(i,m));

        %conditions for all nodes 2 through N-1, This excludes the
        %boundary nodes where the temperature is being measured
```

```
        if (i >= 2) && (i <= N-1)
            D(i) = (rho*c(i)*dx/dt)+(k(i-1)/(2*dx))+(k(i)/(2*dx));
            UD(i) = -k(i)/(2*dx);

            if (i >= 3) %lower diagonal condition for nodes greater than 3
                LD(i) = -k(i-1)/(2*dx);
            end
            % the RHS condition applies to all nodes with an addition to
            % the 2nd and N-1 nodes. Adds that after calculating basic RHS.
            % The i-1 in the LHS of this equations in this secion allows
            % the values to be placed at the correct location in the RHS
            % matrix for linear algebra calculation later on.
            RHS(i-1) = (((rho*c(i)*dx)/dt)*T(i, m))...
                    +((k(i-1)/(2*dx))*(T(i-1,m)-T(i,m)))...
                    +((k(i)/(2*dx))*(T(i+1,m)-T(i,m)));
            if (i == 2)
                RHS(i-1) = RHS(1)+(k(1)/(2*dx))*T(1,m+1);
            end
            if (i == (N-1))
                RHS(i-1) = RHS(i-2)+(k(i)/(2*dx))*T(N,m+1);
            end
        end
    end
    %Moves all values to a matrix so the temperature at each node will be
    %solved simutaniously

    %used to move values to correct location within matrix
     row = 2;
     col = 1;
     LHS = zeros(N-2, N-2);

    %start of loop to move values
    for i=2:N-1

        %only the maind Diagonal and Upper diagonal are here
        if i == 2
            LHS(1,1) = D(2);
            LHS(1,2) = UD(2);

        %3 to N-1 has main diagonal, upper diagonal, and lower diagonal
        else,if i == 3
                for a=3: N-2
                    LHS(row, col) = LD(a);
                    LHS(row, col+1) = D(a);
                    LHS(row, col+2) = UD(a);
                    row = row+1;
                    col = col+1;
                end
            %this node is only Lower diagonal and main diagonal
            else,if i == N-1
                    LHS(row, col) = LD(i);
                    LHS(row, col+1) = D(i);
                 end
            end
```

```
        end
    end
    %linear algebra to solve matrix
    Temp = linsolve(LHS,RHS');

    for l=2:N-1
        T(l,m+1) = Temp(l-1);
    end

    %find heat flux at each node in the direct solve section
    for i=2:N-1
        q(i,m) =abs( k(i)*(T(i+1,m)-T(i,m))/dx);
    end
end

%%%%% Indirect Solve Section%%%%%%

%Set up t=1 with initial conditions
for i=1:N_i
    Ti(i,1) = Tzero;
    qi(i, 1) = q(N-1,1); %changed from N-1 to N-2 since this was being
    %populated with zeros
end

%sets first step to the measured temperature for all times and pull heat
%flux values
for ni=1:M
    Ti(1,ni)=TCa(ni);
    qi(1, ni) = q(N-1,ni); %this was changed from N-1 to N-2
    if ni == M
       qi(1,ni) = q(N-1,ni-1);
    end
end

for i=1:N_i-1 %this is the location loop
    for ni=2:M %this is the time loop
        %time from 2 to M-1
       if ni<= M-1
            k = Thermal_Conductivity(Ti(i, ni));
            c = Specific_Heat(Ti(i,ni));

            if test article_num == 0
                %This is for the top test article, the heat flux in moving
                %in adifferent direction than the bottom test article so
                %there need to be a change in the sign for the Heat
                %Flux
                Ti(i+1,ni)= Ti(i,ni)+ dxi*(-qi(i,ni)/k);
                qi(i+1,ni) = qi(i,ni)-dxi*rho*c*((Ti(i,ni+1)...
                    -Ti(i,ni-1))/(2*dt));

            elseif test article_num == 1
                Ti(i+1,ni)= Ti(i,ni)+ dxi*(qi(i,ni)/k);

                qi(i+1,ni) = qi(i,ni)+dxi*rho*c*((Ti(i,ni+1)...
```

```
                        -Ti(i,ni-1))/(2*dt));
             end
        else
            %last time step is different
            if ni == M
                 Ti(i+1,ni) = 2*Ti(i+1,ni-1)-Ti(i+1,ni-2);
                 if test article_num == 0
                     %again the sign for the heat flux has been changed,
                     %this might not matter since the last points may not be
                     %included in the average calcualtion
                     qi(i+1,ni) = -2*qi(i+1,ni-1)+qi(i+1,ni-2);
                 elseif test article_num == 1
                         qi(i+1,ni) = 2*qi(i+1,ni-1)-qi(i+1,ni-2);
                 end
            end
        end
    end
end
end
```

VITA

OLD DOMINION UNIVERSITY — Norfolk, VA
Master of Science in Mechanical Engineering, May 2020

Pathways Engineering Student Trainee — Hampton, VA
NASA Langley Research Center
Structural & Thermal Systems Branch, February 2017 - present

GRAND VALLEY STATE UNIVERSITY — Allendale, MI
Bachelors of Science in Engineering, August 2016

BOWLING GREEN STATE UNIVERISTY — Bowling Green, OH
Masters of Fine Art, May 2006

GRAND VALLEY STATE UNIVERSITY — Allendale, MI
Bachelors of Fine Art, December 2003